國立台灣大學物理系,
博士論文
Department of Physics, College of Science
National Taiwan University
Ph.D. Thesis

可用來研究電漿子及幫助蝕刻矽晶體的銀奈米粒子有序陣列

Ordered Arrays of Silver Nanoparticles for Plasmonics and Silver-Assisted Silicon Etching

Pradeep Sharma (夏普迪)

Taiwan International Graduate Program (TIGP),
Academia Sinica, Taiwan
&
Institute of Atomic and Molecular Sciences (IAMS)
Academia Sinica, Taiwan

Advisor: Prof. Yuh-Lin Wang (王玉麟教授)

中華民國 100 年 4 月

April, 2011

Acknowledgements

"*There is nothing which is mine in me, whatever is there belongs to you; I offer yours to you my God, nothing belongs to me*". Source of truth-love-peace-joy-knowledge is one, but resources are multiple. The best of human achievements are results of inspirations and strength from God. We must help ourselves and others, and work hard to achieve the best, God is always here to help and guide us. Though I am a common person, God has given me the best Guru, parents, relatives, teachers, friends, coworkers and employers. They all have contributed towards my physical and intellectual growth. Thanks to God for all his blessings.

I am grateful to my PhD thesis advisor Prof. Yuh-Lin Wang for being a constant resource of guidance, suggestions, criticism and inspirations for me. I acknowledge the necessary financial and logistics support by Institute of Atomic and Molecular Sciences, Academia Sinica, Taiwan; and Taiwan International Graduate Program, Academia Sinica, Taiwan.

Pradeep Sharma

Abstract

Silver nanoparticles have been grown by four different methods viz: (1) constrained self organization of Ag films onto silicon substrates, (2) electrochemical growth of Ag into custom-designed porous anodic alumina templates, (3) electron-beam lithography, and (4) galvanic displacement of Si by Ag. Methods '1-3' yield ordered arrays of Ag nanoparticles whereas method '4' results in growth of self organized Ag nanoparticles. Only method '2' produces arrays of dimers and trimers of silver nanoparticles with sub-5 nm interparticle gap. Mechanisms for growth of Ag nanoparticles by methods '1, 2', and '4' have been discussed.

Surface plasmons of Ag nanoparticles formed by method '1' have been mapped by scanning electron transmission microscope (STEM)–electron energy loss spectroscopy (EELS). Experimental results are found to be consistent with STEM-EELS calculations.

Directional etching of Si(100) substrates by different types of Ag nanostructure is achieved. Key parameters which promote the directional etching have been identified.

Mechanisms of "galvanic displacement mediated Ag plating on Si" and "Ag-assisted etching of Si" are elucidated by high resolution electron microscopy and *in-situ* Raman and FTIR spectroscopy.

Key words

Ordered arrays of Ag nanoparticles, Surface plasmon mapping, Electroless Ag plating, Ag-assisted Si etching, ion and electron microscopy, *in-situ* Raman and FTIR spectroscopy.

摘　要

我們用四種方法來成長銀奈米粒子: (1) 蒸鍍銀薄膜在矽基板表面, 經由限制性自組織來形成奈米粒子, (2)在氧化鋁孔洞基板, 經由電化學過程來形成奈米粒子, (3)用電子束顯影蝕刻術, 來製造奈米粒子, (4)直流置換矽為銀奈米粒子. 其中方法 ‘1-3’可形成有序銀奈米粒子, 而方法 ‘4’可長出自組的銀奈米粒子, 特別地, 方法 ‘2’可形成間隙小於 5 奈米之銀粒子雙連體或三連體陣列. 方法 ‘1,2,4’ 的機制將會討論.

我們使用掃描電子穿透顯微術—也就是電子能量損失能譜術, 對方法 ‘1’長出的銀奈米粒子, 進行表面電漿子掃描分析. 實驗的結果與理論的計算相符合.

藉著不同型態的銀奈米結構, 我們可以對矽(100)基板做方向性蝕刻, 也找到這種蝕刻的關鍵參數.

經由高解析電子顯微鏡, 就地觀測的拉曼光譜術, 以及傅利葉轉換紅外線光譜術等觀測, 我們釐清在矽基板進行置換銀電鍍, 以及藉銀粒子輔助的矽晶蝕刻等現象的機制.

關鍵字

奈米銀粒子的有序陣列, 表面電漿子掃描分析, 無電極的銀電鍍, 銀輔助的矽晶蝕刻, 離子和電子顯微觀測術, 就地觀測的拉曼和傅利葉轉換紅外線光譜術

Contents

List of figures

Chapter 1 Introduction

Following is the brief discussion of different phenomena and underlying concepts relevant to understanding of this thesis.

1.1 Constrained self organization

Self organization generates structural hierarchy on all scales from atoms to galaxies through multiple interactions of different entities and surroundings. Driving forces for the self organization are lowest energy configuration of the formed structure, temperature, strain, electro-magnetic field, gravitational force, capillary force, physical-chemical bonds and interactions etc. An atom is a self-organized structure of electrons, protons and neutrons driven by minimization of energy and reactivity of the formed structure. Material to material, energy to energy and matter to energy transformations and vice-versa transformations are well known in science. Form emerges from formless entities upon interaction between entities under the action of driving forces.

Vapor-liquid-solid (VLS) growth of ZnO micro-nanostructures [1,2] is a typical example of emergence of form from the formless dust of Zn, and ZnO & graphite. For VLS growth, first a noble metal (Au, Ag) catalyst thin film or nanoparticles is deposited on to a substrate and then the substrate is loaded into a chemical vapor deposition (CVD) chamber. Then the temperature of the CVD chamber is raised to form the metal catalyst droplets followed by introduction of the substance to be grown as vapor. These vapors absorb onto the liquid surface and diffuse into the droplet. Supersaturation and nucleation at the liquid/solid interface leads to directional growth of crystalline materials. VLS

growth allows the site selective and spatially constrained growth of semiconducting (Si, Ge) and insulating (ZnO) nanostructures. Fig. 1.1 shows scanning electron microscope (SEM) images of different ZnO nanostructures viz. nanowires, nanosprings, nanospirals, nanorods, and nanotetrapods formed by VLS growth. Formed ZnO nanostructures find a wide variety of applications in photocatalysis, photoluminescence, photovoltaics, field emission and gas sensing etc. [1,2]. VLS growth also reveals the effect of temperature on formation and self organization of these micro-nanostructures.

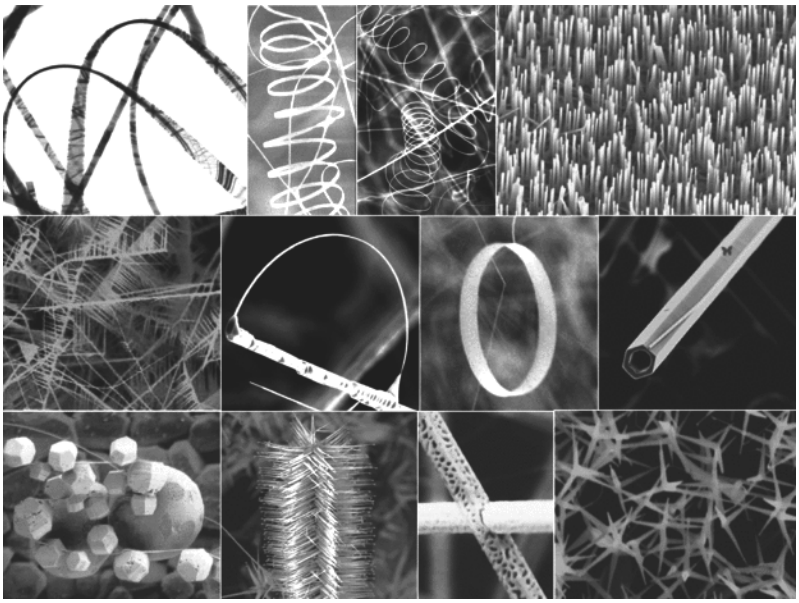

Figure1.1: SEM images of ZnO nanospirals, nanowires, nanorods and nanotetrapods formed by VLS growth [1,2].

In addition to temperature, if there exist a pinning or constraining center (either physical or chemical) then it will lead to formation of ordered arrays of nanostructures as demonstrated by growth of ordered arrays of Ag nanoparticles by constrained self organization [3]. Growth and surface plasmon properties of these Ag nanoparticles will be discussed in detail in Chapter 2 and 3 of this thesis. In brief, the post deposition

annealing of the Ag deposited on a focused ion beam (FIB) patterned Si substrate results in constraining of the migration of Ag on the patterned region which results in formation of ordered arrays of Ag nanoparticles.

Magnetic field [4] and strain [5] have been used to elucidate the self organization of Fe_3O_4 nanoparticles and metal-insulator domains in VO_2 nanobeams respectively. Fig. 1.2 shows the SEM and transmission electron microscope (TEM) images of the aligned Fe_3O_4 nanoparticles chains under the action of magnetic field. A uniaxial magnetic anisotropy in the saturation field, hysteresis loop and ferromagnetic resonance is observed to increase with increasing field [4].

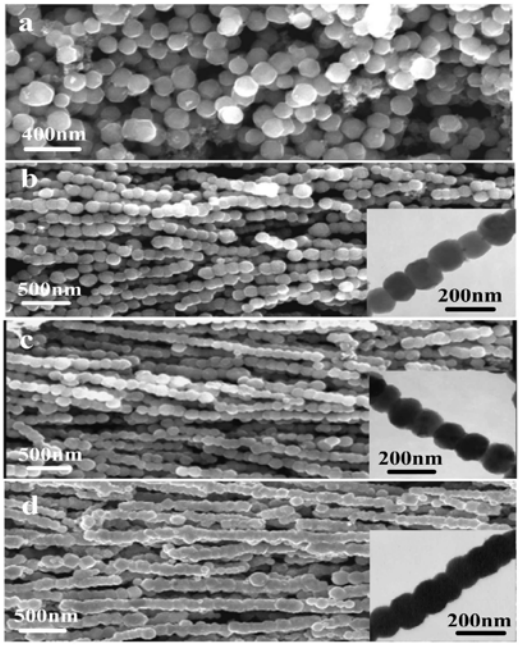

Figure 1.2: SEM and TEM images of the samples prepared with magnetic field of (a) 0, (b) 1000, (c) 2500, (d) 3500 Oe [4].

Though gravitational force is negligible in promoting self organization of the nanostructures but for microstructures it can play a vital role as illustrated by gravity

dependent self-organization of microtubules [6]. Capillary force has been widely used for topologically constrained self organization of colloids [7] and nanopillars [8]. Fig. 1.3 shows the SEM images of the ordered arrays of colloidal microparticles. When an aqueous solution of colloidal microparticles is allowed to dewet from a patterned solid surface then the particles are trapped in patterned regions forming a dimer, trimer, quadramer, and pentamer etc. depending on the geometric constrain provided by the patterned surface. Depending on the geometry of the patterned surface and liquid flow direction during the dewetting process, formation of linear chains of particles is also observed.

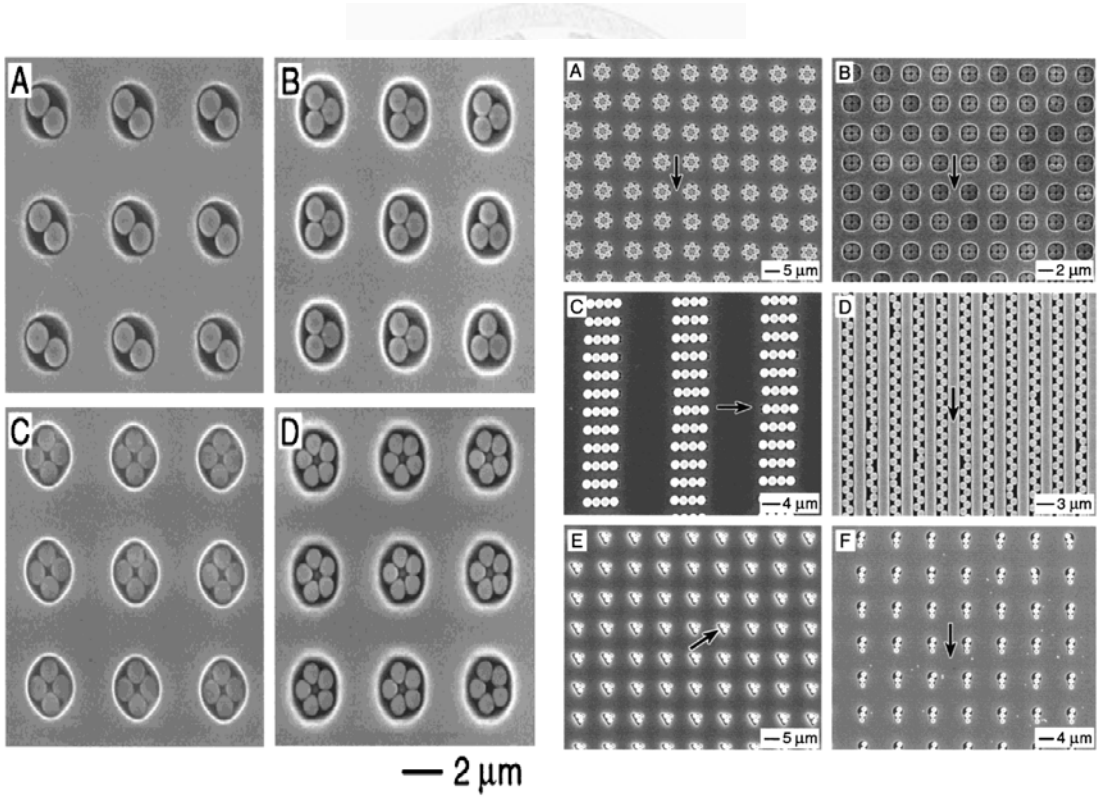

Figure 1.3: SEM images of the ordered arrays of polystyrene (PS) microparticles formed on different templates. In the left hand side image, the size of PS beads is gradually reduced from 1 µm to 0.7 µm to form dimer to pentamer arrays of microparticles. In right hand size image, the arrows indicate the direction of flow of liquid slug [7].

Fabrication of ordered two dimensional arrays of micro- and nanoparticles arrays by using patterned self-assembled monolayers (SAMs) have also been reported [9]. Microcontact printing is used to pattern the Au surfaces into grids of hydrophobic and hydrophilic SAMs of alkanethiolates. When this patterned substrate is immersed in an aqueous solution of an organic or inorganic salt and then withdrawn, the solution wets and is retained exclusively on the hydrophilic regions of the surface. Eventually water evaporates leaving behind an ordered array of micro- and nanoparticles. Fig. 1.4 shows the atomic force microscope (AFM) of the $CuSO_4$ particles of different sizes from 50 to 500 nm.

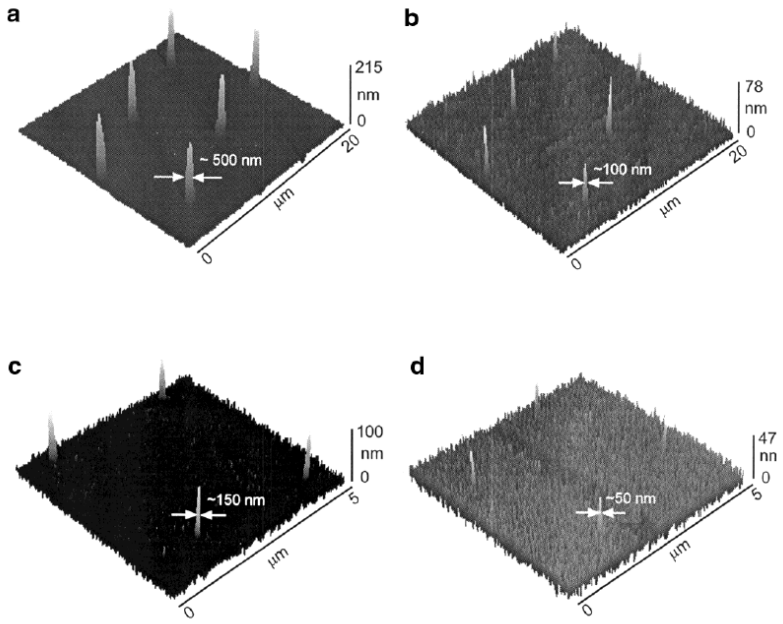

Figure 1.4: (a), (b) AFM images of ordered arrays of $CuSO_4$ particles formed on the surfaces patterned with 5x5 µm square grids of COOH terminated SAMs from a 0.5 M and 0.05 M $CuSO_4$ solution respectively. (c), (d) AFM images of $CuSO_4$ particles on the surfaces patterned with surfaces 2x2 µm square grids of COOH terminated SAMs from a 0.5 M and 0.05 M $CuSO_4$ solution respectively [9].

1.2 Surface plasmon

Surface plasmons, are defined as fluctuations in the electron density at the boundary of two materials. Plasmons, as shown in Fig.1.5, are collective vibrations of an electron gas (or plasma) surrounding the atomic lattice sites of a metal. When a plasmons couples with a photon, then resulting particle is called a polariton. This polariton propagates along the surface of the metal until it decays, either by absorption, whereupon the energy is converted into phonons, or by a radiative transition into a photon.

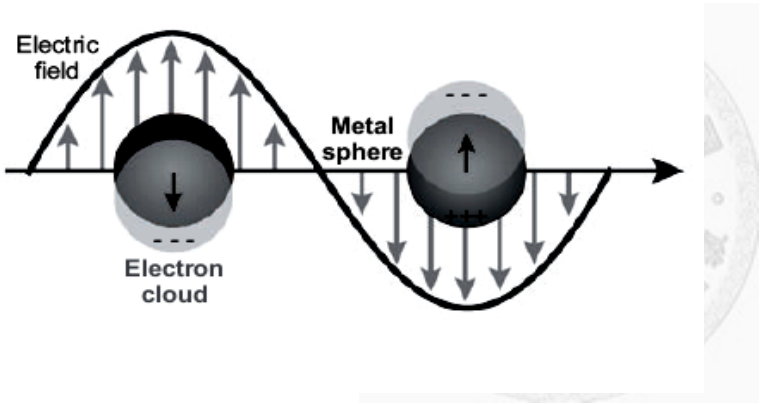

Figure 1.5: Illustration of localized surface plasmon resonance effect [10].

Investigation of optically excited coherent conduction electron oscillations in metallic NP, is known as localized surface plasmon resonance (LSPR) study. NPs of Ag, Au, Pd, Pt, Al and Cu nanostructures support surface plasmon resonances in ultra violet (UV)-visible (VIS)-near infrared (NIR) regime [10-17]. In addition, optical properties of metal NPs depend on size, shape and dielectric environment of the NP [18] which in turn helps to tune surface plasmon resonance position [19-24]. Peak position as well as width of surface plasmon resonance is also found to be dependent on interparticle distance [24].

Characteristic decay length of surface plasmons of metal NPs is estimated to be about 20% of size of NP [25]. Accordingly, when metal NPs are close enough and surface plasmons are interacting then optical properties of ensemble of co-related NPs are quite different from that of ensemble of isolated NPs [24, 26]. Fig. 1.6 shows the effect of interparticle gap on the scattering spectra. Decreasing gap results in red shift of the transverse surface plasmon mode of Ag nanorods embedded in AAO. Reduction of gap also results in strong surface plasmon coupling of these Ag nanorods which has been exploited for fabrication of a highly Raman enhancing substrates [36]. Fig. 1.7 shows another example of effect of paprticle-particle interaction upon the extinction spectra of Ag nanoparticles.

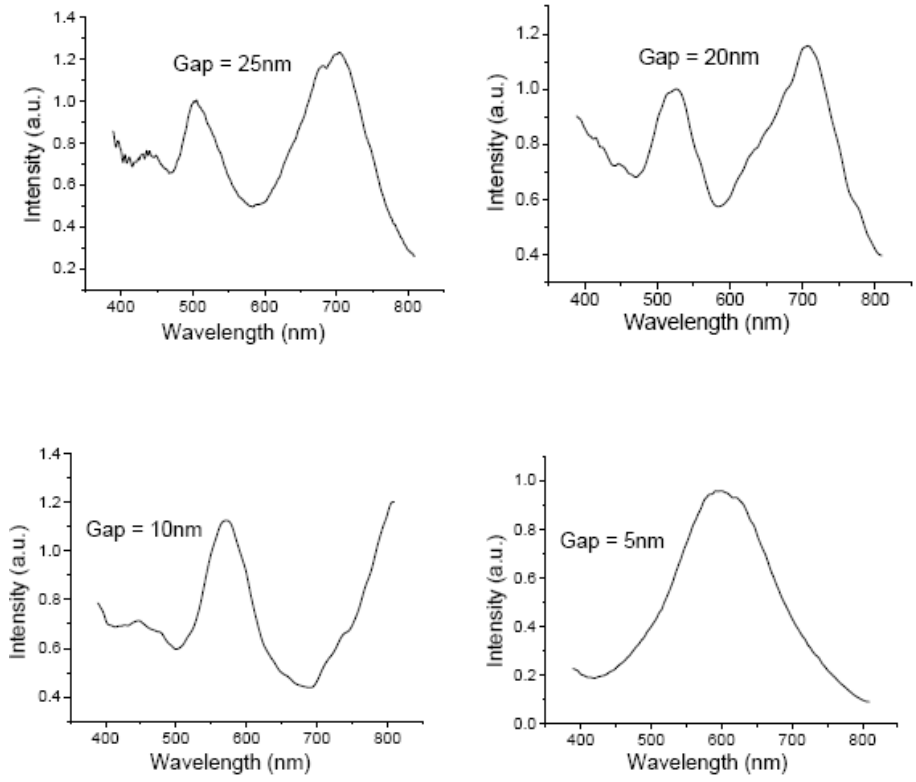

Figure 1.6: Dark-field scattering spectra from Ag nanorods in AAO samples for different gaps between the Ag nanorods [24].

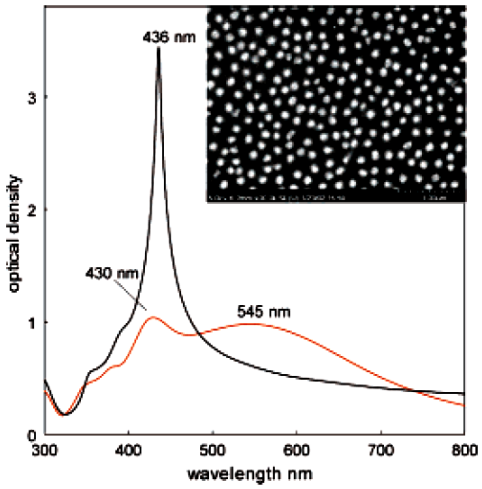

Figure 1.7. Extinction spectra of 100-nm Ag particles in water (red curve) and the same particles assembled into a closely spaced 2D array imbedded in poly-(dimethylsiloxane) (PDMS) (black curve). Inset: electron microscopy image of this 2D array. The spectrum (black curve) corresponds to the image in the inset [26].

Properties of nanoparticle ensembles are governed by electromagnetic interactions between the localized modes. For small particles (size ~ 30 nm) these interactions are essentially of a dipolar nature, and the particle ensemble can in a first approximation be treated as an ensemble of interacting dipoles. For bigger particles quadruple and higher order interactions are to be considered to describe the ensemble [27]. Consider a specific example of linear chain of NPs. Using the simple approximation of an array of interacting point dipoles, the direction of the resonance shifts for in-phase illumination can be determined by considering the Coulomb forces associated with the polarization of the particles. As sketched in Fig. 1.8, the restoring force acting on the oscillating electrons of each particle in the chain is either increased or decreased by the charge distribution of neighboring particles. Depending on the polarization direction of the exciting light, this

leads to a blue-shift of the plasmon resonance for the excitation of transverse modes, and a red-shift for longitudinal modes [27].

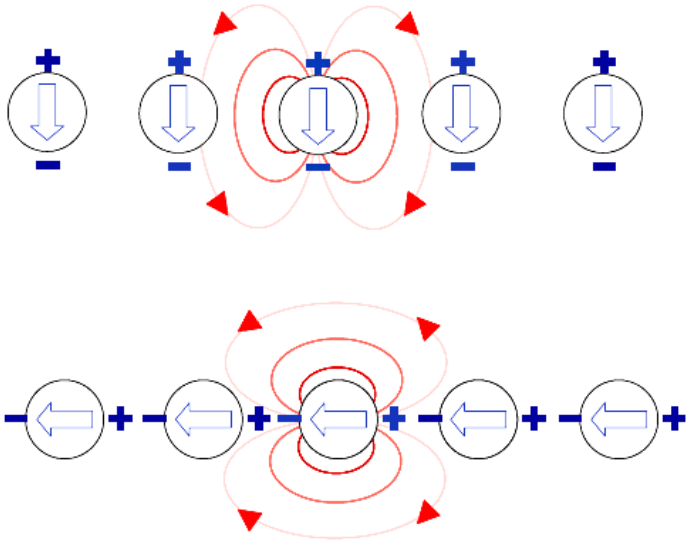

Figure 1.8: Schematic of near-field coupling between metallic nanoparticles for the two different polarizations [27].

Surface plasmons of nanoparticles can be excited by longitudinal electric field of highly accelerated charged particles as well as transverse electric field of photons. Electrons entering a crystal transfer energy $\Delta E = \hbar\omega$ and momentum $\hbar q$ to the excitation according to following equations:

$$(\hbar q)^2 = (\hbar k_{el}\theta)^2 - (\hbar\omega/v)^2 = (\hbar q_{\_})^2 - (\hbar q_{\|})^2$$

where k_{el} : wave vector of the incoming electron. θ : scattering angle of the electron. $\hbar\omega$: transferred energy. In case of normal incidence of the electron beam the component of k_{el} parallel to the surface is given by

$k_x = q_{\_} = k_{el}.\theta$:

Dispersion relation can be scanned over by varying θ. Radiative as well as nonradiative plasmons can thus be excited. The excitation is detected by measuring the energy losses of the electrons in an energy analyzer [28]. As a typical example, excitation of surface plasmon of Ag nanoparticle by electron beam and corresponding EELS spectra and nanoscale map of plasmon intensity are shown in Fig. 1.9.

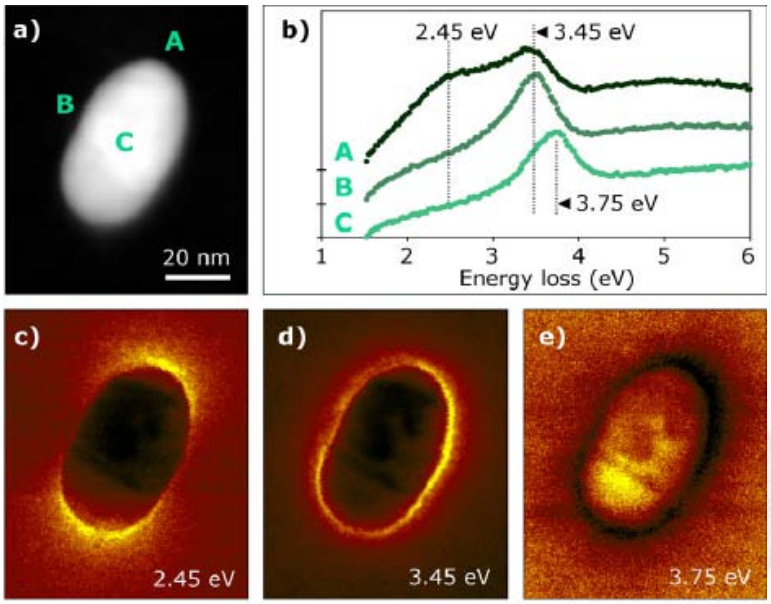

Figure 1.9: (a) Annular dark field STEM image of an ellipsoidal silver particle. (b) Spectra from the three regions indicated in (a). (c) Map of the plasmon intensity at 2.45 eV (λ = 506 nm), showing the longitudinal resonance mode. (d) Map of the plasmon intensity at 3.45 eV (λ = 360 nm), showing the transverse resonance mode. (e) Intensity map of the bulk plasmon resonance at 3.75 eV (λ = 330 nm). The intensity in the last map further than about 10 nm off the ellipsoid is caused by spectral noise [29].

Light directed onto a surface can excite radiative SP's directly. Direct excitation is not possible with nonradiative SP's since frequency and wave vector of the surface

plasmon can not be matched simultaneously. Following two methods allow overcoming this difficulty [28].

a) The grating coupling method:

Here a corrugated surface, e.g., a grating with periodicity a, is irradiated with light of frequency ω and wave vector $k_l = \omega / c$ .The wave vector in the boundary k_x can be changed into $k_x^{'} = k_x \pm n\frac{2\pi}{a}$, n integer. Thus the dispersion relation ($k_x^{'}$) can be

b) The prism method:

Light falls from the dielectric material ε_1, e.g., quartz, on the boundary of a plasma slab $\varepsilon_1/\varepsilon_2$; the wave vector component parallel to the surface is given by $k_x^{'} = \sqrt{\varepsilon_1}(\omega / c)\sin\theta_0$. If $\sqrt{\varepsilon_1}\sin\theta_1 \geq 1$, the vector $k_x^{'}$ lies right from the light line and total reflection at the boundary 1/2 takes place so that an inhomogeneous wave (evanescent wave) with the phase velocity $c/(\sqrt{\varepsilon_1}\sin\theta_1) < c$ runs along the boundary $\varepsilon_1/\varepsilon_2$. This inhomogeneous wave can excite nonradiative SP's at the boundary $\varepsilon_2/\varepsilon_3$ if the thickness of medium ε_2 is not too large. ε_2 can be the plasma and ε_3 a dielectric, e.g., air, or vice versa. In the experiment, medium (ε_1) is given by form of a prism or a half cylinder. Entering the medium (ε_1), the light gains the additional momentum $\Delta k_x = (\sqrt{\varepsilon_1 - 1})\frac{\omega}{c}\sin\theta_1$ so that it can excite the nonradiative plasmons. The resonance case is detected by a deep minimum in the totally reflected beam since the plasmon absorbs energy,as in the case of grating coupling. Therefore the prism method is often called the ATR method (attenuated total reflection).

1.3 Porous anodic alumina (or Anodic Aluminum Oxide or AAO)

When Al is anodized in neutral or basic solutions (pH > 5), a flat, non-porous, featureless insulating oxide film is formed. This type of anodized alumina is in use for the protection and decoration of surfaces since 1923. In last two decades, PAA or anodic alumina, a nanostructured material with arrays of self organized and self aligned nanochannels, has gained attention due to ultrahigh pore density, optical transparency, and mechanical robustness. When Al is anodized in an acidic electrolyte [e.g. sulfuric acid (H_2SO_4), oxalic acid ($H_2C_2O_4$), and phosphoric acid (H_3PO_4)], deep pores (size ≈ 0.3 x lattice constant of anodic alumna (L, where I≈ 2.5 x anodization voltage by assuming 10% porosity in formed structure) can form, with diameters varying between 5 and 100 nm and lengths up to several microns. The bottom of each pore consists of a thin "barrier layer" (thickness≈ 0.7 L) over the metallic Al surface. The pore diameter depends on pH, anodization voltage, and choice of acid [30].

The chemical reaction describing the growth of anodic alumina nanochannels is given as: 2 Al (s) + 3 H_2O → Al_2O_3 (oxide) + 3 H_2. AAO nanochannels can be filled with dyes and micro/nanoparticles and sealed by boiling in water. And corresponding chemical reactions is given as: Al_2O_3 + H_2O → 2 AlOOH.H_2O. This sealing of pores enhances corrosion resistance and limits the photobleaching of the encapsulated dyes. They find applications in decorative hard coating of cellular phones etc.

Naturally self-organized AAO have two drawbacks. First, the ordered range can only reach up to several microns. Second, the nanochannels can have ordered structure at backside but they have disordered structures at topside. This is because the nanochannels grow from random initiated pores at the initial stage and later repulsive forces between

the channels, caused by mechanical stress at Al/alumina interface, pushes the system to form an ordered structure. Highly ordered AAO can be formed by two-step anodization [31], mechanical molding of Al surface [32], focused ion beam pre-patterning of Al surface [33], holographic patterning of Al films [34] and interference lithography [35] etc. Fig. 1.10 shows cross section and plan view of ordered arrays of anodic alumina nanochannels formed in oxalic acid at 40 V. Interpore spacing of the AAO formed in oxalic acid is 100 nm as is observable in the SEM images.

AAO can be filled with different materials like noble metals [36], semiconductors [37], thermoelectric materials [38], magnetic materials [39] oxides and polymers [40, 41], which make AAO a versatile template for wide range of nanoscale application. AAO has been used for growth of Ag nanoparticles based surface enhanced Raman scattering (SERS) substrate [36]. Fig. 1.11 shows the scanning transmission electron microscope (STEM) half angle annular dark field images of this SERS substrate. It shows self organized Ag nanoparticles embedded in anodic alumina. To demonstrate the SERS activity of this substrate, SERS spectrum of Rhodamine 6G on Ag NPs filled anodic alumina is shown in Fig. 1.12. Electromagnetic enhancement is believed to arise from the highly enhanced fields in metal nanoparticle junctions due to localized surface plasmon resonances. Highly confined fields are better known as '*hot spots*'.

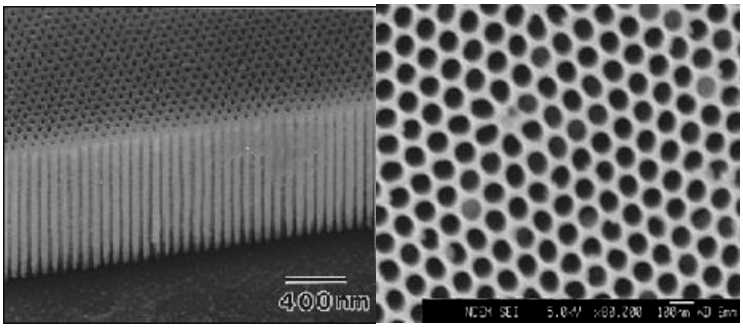

Figure 1.10: SEM images of AAO formed in Oxalic acid [33].

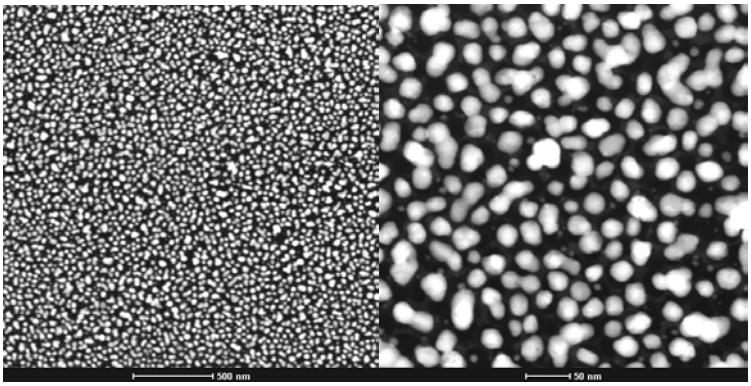

Figure 1.11: STEM HAADF images of SERS substrate. Silver nanoparticles are separated by anodic alumina walls (thickness of wall < 10 nm).

A proper understanding and control over the generation of these hot spots is one of the major driving forces behind the design of noble metal nanoparticle ensembles with tunable optical properties. AAO offers precise control over interparticle gaps. Interparticle gap dependent light scattering from 2D arrays of monodispersed Ag-nanoparticles in anodic alumina was studied was Biring et.al. [42]. Therefore, AAO is a good template for fabricating plasmonic substrates.

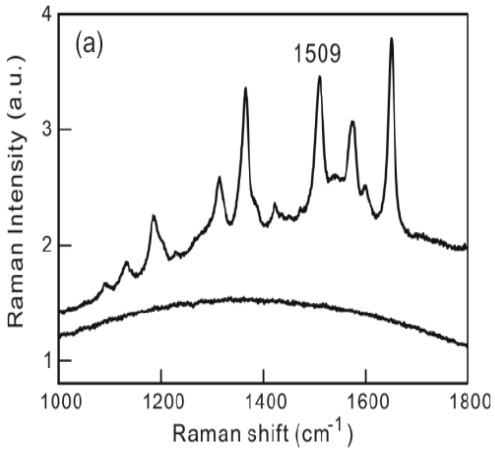

Figure 1.12: SERS spectrum of 10^{-6} M R6G solution on a Ag/AAO substrate, and on a typical SERS substrate prepared by depositing < 30 nm Ag on Si (bottom plot) [36].

1.4 Electroless metal deposition

Electroless metal plating is defined as deposition of metal films onto conducting (metal, alloys, and semiconductors) or insulating (polymer, glass, and ceramics etc.) substrates without using any external bias. It can be further classified as galvanic displacement plating and auto-catalytic plating [43]. Former involves replacement of substrate's material by a metal with lower redox potential as compared to the substrate and later involves reduction of metal ions on the substrates by a reducing agent. Following reactions describe the galvanic displacement plating of noble metals on Si substrate:

$M^{n+} + ne^- \rightarrow M$, where M = metal like Ag, Au, Pt

$Si + 2H_2O \rightarrow SiO_2 + 4H^+ + 4e^-$

$SiH_x + 2\ H_2O \rightarrow SiO_2 + (4+x)H^+ + (4+x)e^-$

$SiO_2 + 6HF \rightarrow H_2SiF_6 + 2H_2O$

$2H^+ + 2e^- \rightarrow H_2$

Here, metal ions get reduced on Si surface by taking electrons from Si which results in injection of holes into valence band of Si. Si with injected holes reacts with water form silicon oxide which is eventually dissolved by HF providing a clean Ag/Si interface where further reduction and deposition of metal continues. Deposition of metals can also be performed on conducting surface and it is well illustrated by deposition of Cu onto steel ($Fe + Cu^{2+} \rightarrow Cu + Fe^{2+}$). This type of displacement reaction requires that reactivity of the metal to be deposited should be less than that of the substrate. On the other hand, in case of auto-catalytic plating, deposition of metal on the conducting/semi-conducting

substrates occurs with the help of a reducing agent. Reducing agent like $NaBH_4$ itself gets oxidized and causes the reduction of metal ions on the surface of the substrates.

$R \rightarrow R^{n+} + ne^{+}$, where R= reducing agent

$M^{n+} + ne^{-} \rightarrow M$, where M = metal

In order to coat insulating substrates with metals, an activation layer or seed layer of metal ions (e.g.: Sn^{2+} from $SnCl_2$ or Pd^{2+} from $PdCl_2$) is deposited prior to plating [44]. Electroless plating results in uniform and conformal coating of the substrates because of absence of spatial variations of current or electric field on the substrates [45]. Applications of electroless metal plating includes deposition of protective [46], and decorative films [47]; interconnects and contact pads etc. in integrated circuit (IC) industry [48], metal nanostructures for surface enhanced Raman spectroscopy (SERS) substrates [49,50], plasmonics [51], catalysis [52], electromagnetic shielding [53], and bio-medical technologies [54], growth of Si nanowires [55], and energy storage and production [56]. Fig. 1.13 illustrates examples of nanostructures formed by electroless plating.

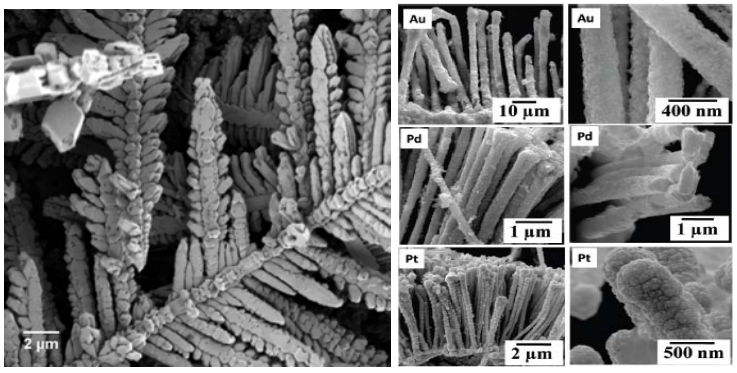

Figure 1.13: (left) SEM images of Ag dendrites (a SERS substrate) from galvanic displacement on commercial Al foils [49]. (right) SEM images of Au, Pd and Pt nanorods formed by galvanic exchange reaction for catalysis [52].

1.5 Metal assisted silicon etching

Metal assisted or electroless etching of Si refers to etching of Si in a solution containing HF and metal salts (e.g.: $AgNO_3$) [57]. Here, Ag is deposited onto the Si substrate by galvanic displacement reaction discussed in section 1.3. Deposited Ag assists in etching of Si underneath giving rise to formation of Si nanowires as shown in Fig. 1.14.

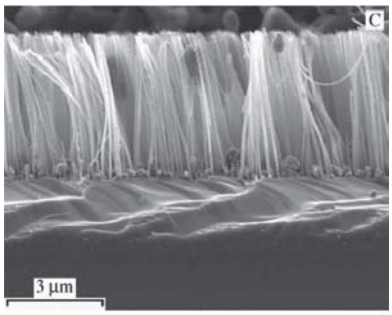

Figure 1.14: SEM image of Si nanowires formed by electroless etching of Si in aqueous solution of HF and $AgNO_3$ [57].

Alternatively, metal assisted Si etching can be conducted in aqueous solution of HF and an oxidizing agent like H_2O_2 after deposition of metal (Ag, Au, Pt, Cu or Pd) thin films or nanoparticles (NPs) or lithographic patterns onto the Si. Fig. 1.15 shows formation of different Si nanostructures depending on the morphology of Ag catalyst.

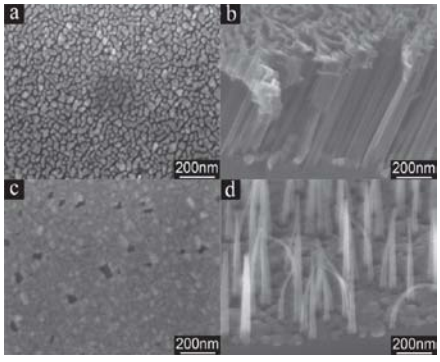

Figure 1.15: SEM images showing the effect of deposited Ag film morphology (a and c) on the morphology of the etched Si (b: nanoholes and d: nanowires) [61].

Different mechanisms have been proposed to explain the metal assisted etching of Si. It is agreed that at cathode i.e. at metal catalyst surface the oxidizing agent like H_2O_2 is reduced and hydrogen is evolved at anode.

$H_2O_2 + 2H^+ + 2e^- \rightarrow 2H_2O$

$2\ H^+ + 2e^- \rightarrow H_2$

But dissolution of Si into solution is described in different ways. Peng et. al. [57] proposed that Si etching proceeds by formation of silicon oxide and its dissolution into solution by HF.

$Si + 2H_2O \rightarrow SiO_2 + 4H^+ + 4e^-$

$SiO_2 + 6HF \rightarrow H_2SiF_6 + H_2O$

Li et. al. [58] proposed the direct dissolution of Si in tetravalent state.

$Si + 4h^+ + 4HF \rightarrow SiF_4 + 4H^+$

$SiF_4 + 2HF \rightarrow H_2SiF_6$

Chartier et.al. [64] proposed a mixed reaction composed of divalent and tetravalent dissolution of Si.

$Si + HF_2^- \rightarrow H_2SiF_6 + 2\ HF + H_2 + 2e^-$, and the overall reaction is:

$$Si + \frac{n}{2}\ H_2O_2 + 6\ HF \rightarrow n\ H_2O + H_2SiF_6 + \frac{4-n}{2}\ H_2$$

Nonetheless, electroless etching of Si has been applied successfully for improving photoluminescence of Si [58], enhancing photovoltaic efficiency of solar cells [59], site selective etching of Si [60], growth of Si nanostructures [61-64], creation of super-hydrophobic surfaces [65], and etching of three dimensional nanostructures into Si by lithographically defined Au patterns [66].

1.6 Fabrication and characterization tools

Electroless plating onto Si substrates [48-50, 55], electrodeposition into AAO templates [36], electron beam (e-beam) lithography [67], and focused ion beam (FIB) lithography [68] are used to fabricate different types of Ag and Si nanostructures. Characterization of the formed nanostructures has been performed using atomic force microscopy (AFM) [69], scanning electron microscopy (SEM) and transmission electron microscopy (TEM) [70], scanning transmission electron microscope (STEM) [71] equipped with electron energy loss spectroscopy (EELS) [72], Raman spectroscopy [73], and FTIR spectroscopy [74].

In order to select right tool for characterization it is necessary to know the analysis depth (Fig. 1.16) and detection limit (Fig. 1.17) of different tools.

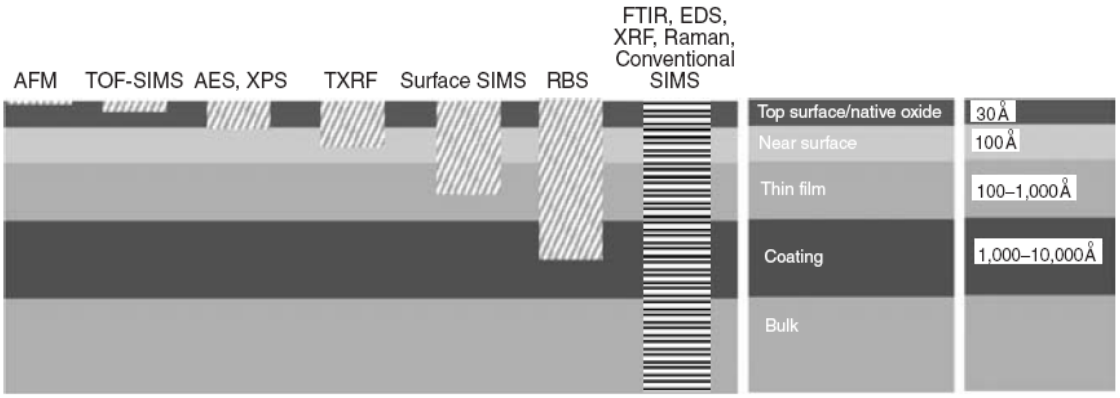

Figure 1.16: Analysis Depth of various characterization techniques [75].

Acronyms of Fig. 1.16 and Fig. 1.17 are described as the following: AES = auger electron spectrometry, AFM = atomic force microscope, EDS = energy dispersive X-ray spectrometry, ESCA = electron spectroscopy for chemical analysis, FE-SEM = field emission scanning electron microscopy, FIB = focused ion beam, FTIR = Fourier

transform infrared spectrometry, GC/MS = gas chromatography/mass spectrometry, HFS = hydrogen forward scattering spectrometry, MFM = magnetic force microscopy, MSMS = Enhanced sensitivity for quantization with tandem mass spectrometry, PIXE = particle-induced X-ray emission, RBS = Rutherford backscattering spectrometry, SAM = scanning auger microscopy, SEM = scanning electron microscopy, SIMS = secondary ion mass spectrometry, TEM = tunneling electron microscope, STM = scanning tunneling microscope, TOF-SIMS = time-of-flight secondary ion mass spectrometry, TXRF = total reflection X-ray fluorescence, XPS = X-ray photoelectron spectroscopy, and XRF = X-ray fluorescence.

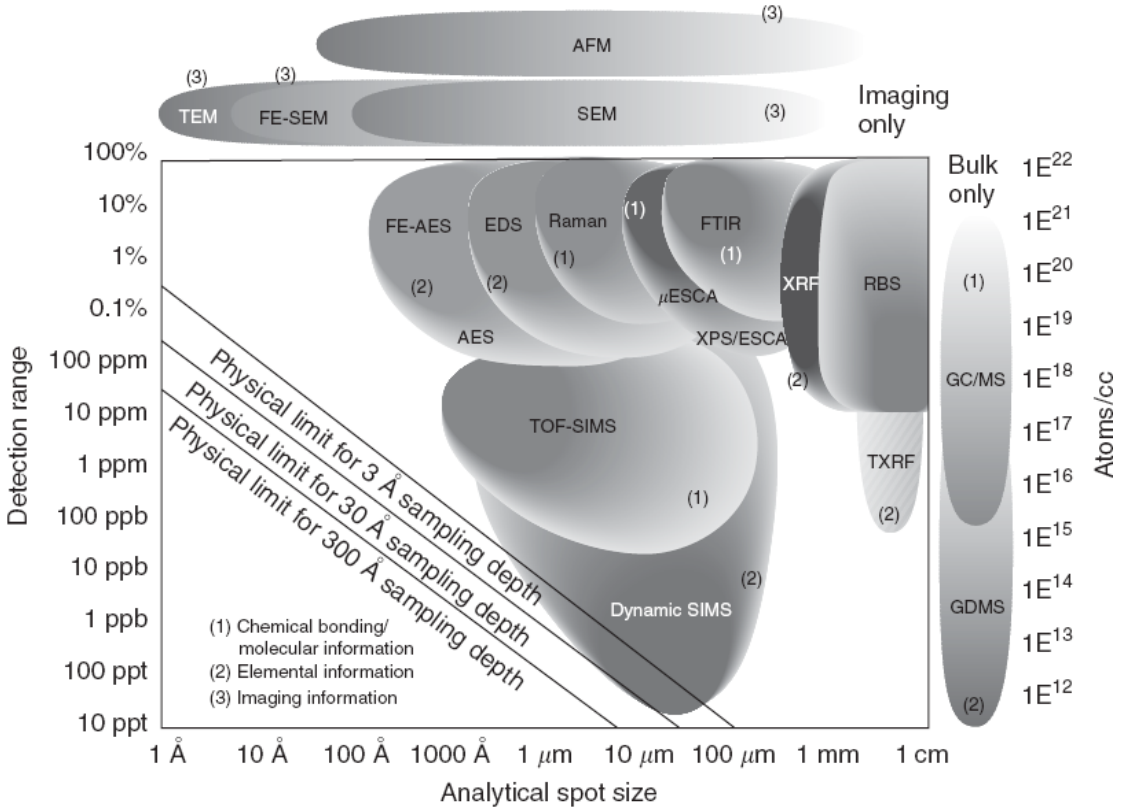

Figure 1.17: Analytical resolution versus detection limit of various techniques [75].

Chapter 2 Ordered arrays of Ag nanoparticles by constrained self organization

2.1 Aim

In recent years considerable efforts have been made to fabricate ordered arrays of nanoparticles and examples include: application of ordered anodic alumina nanochannels for the fabrication of ordered Ag nanoparticles arrays [76,36], integration of colloidal nanocrystals into lithographically patterned substrate [77] by using interfacial capillary force as driving agent, self assembly of size and position controlled ultralong nanodot (≈ 100 nm) chains by using near field optical desorption [78] and fabrication of ordered two dimensional arrays of micro- and nanoparticles by using patterned self assembled monolayers as templates [9]. In this letter, we report the use of focused ion beam (FIB) [79] to create a lattice of aggregation centers on a Si(100) substrate, for constraining the surface migration of Ag in a post-deposition annealing process and growing ordered arrays of Ag nanoparticles. In addition, the mechanism for constrained self-organization of Ag nanoparticles on the ion-irradiated Si substrate is discussed.

2.2 Experiments

2.2.1 Patterning of Si substrates

p-type Si(100) substrates (10 Ω·cm resistivity) are cleaned by sonication in acetone, methanol and deionized water (18.2 MΩ·cm resistivity) for 5 minutes separately. Immersing such substrates in 1% HF solution for 5 minutes followed by rinsing in

deionized water for another 5 minutes results in formation of hydrogen (H) terminated Si surface. After drying with N_2 gas, a commercial 50 KeV Ga^+ FIB with diameter ~10 nm and beam current of 1.1 pA is used to irradiate these cleaned Si substrates for creating arrays of aggregation centers. The working pressure of the FIB system is maintained below 1 x 10^{-7} Torr during the ion irradiation. The ion beam dose is varied from 2 x 10^{14} ions/cm^2 to 1 x 10^{16} ions/cm^2, which corresponds to ramping the dwell time (Δt) of the FIB on a single pixel from 0.2 ms to 10 ms, to create different aggregation regions on the substrate surface. Square as well as hexagonal closed packed arrays of aggregation centers with 100 nm lattices constant are patterned onto the Si substrates. Morphologies of the formed aggregation centers are characterized using AFM.

2.2.2 Low temperature Ag deposition

Low temperature (~200 K) deposition of Ag on the FIB-irradiated substrate is conducted by radio-frequency (RF) magnetron sputtering of a Ag target (99.99 %) under a Ar gas pressure of 2 mTorr. Before deposition the base pressure of deposition chamber is 2 x 10^{-6} Torr. The substrate is cooled down using flowing liquid nitrogen connected to the substrate through a vacuum feed through. During deposition the temperature of the substrate is monitored by type-K thermocouple. This thermocouple is made of Chromel (90 % Nickel + 10 % Chrome) and Alumel (95% Nickel + 2 % Manganese + 2 % Aluminum + 1 % Silicon) and offers a sensitivity of about 40 μV/ºC. It is a general purpose thermocouple useful for temperature ranging from -200 ºC (73 K) to 1350 ºC (1623 K). While maintaining temperature about 200 K, Ag thin film is deposited onto the patterned substrates. We tuned Ag film thickness from 1 to 5 nm for achieving the

optimum thickness of Ag film yielding maximization of ordering of the formed Ag nanoparticles arrays.

2.2.3 Post deposition annealing of patterned substrates

After Ag thin film deposition, the substrates are annealed at different temperatures ranging from 570 K to 970 K for one hour in a chamber that has been pumped down to a base pressure of 10^{-6} Torr before back filling with N_2 (99.999 %) to a pressure of 0.5 atm. Morphologies of the annealed Ag films are recorded using SEM. TEM and TEM-EDX spectra are used to reveal the cross-sectional morphologies of formed Ag nanoparticles and to examine the Ag nanoparticles/Si interfaces respectively.

2.3 Results and discussion

2.3.1 Ordered arrays of aggregation centers on Si substrate

Depending on isolated single pixel FIB irradiation dose (or FIB dwell time) formation of nanoscale protrusions and craters occur onto Si surface. As shown by the contact-mode atomic force microscope (AFM) image of the surface morphology (Fig. 2.1), the regions exposed to FIB with dwell time (Δt) = 1 ms appears as protrusions on the substrate. These protrusions are the result of ion beam induced swelling-distortion (amorphization of the crystal and deposition of the residual gases) of Si lattice [80]. Irradiation of a crystal by energetic ion beams leads to sputtering of atoms from the crystal surface as well as defect formation in the near surface region. The amount of sputtered material and the density of the defects increase with increasing ion dose. Beyond a certain threshold dose, the damage becomes so severe that the crystalline

structure collapses and an amorphous layer is formed. From a surface morphologic point of view, sputtering results in the formation of a crater, while defects in the lattice usually lead to protrusions on the irradiated surface. These two effects are opposite and the final height of the irradiated surface depends on the competition between sputtering and defect formation.

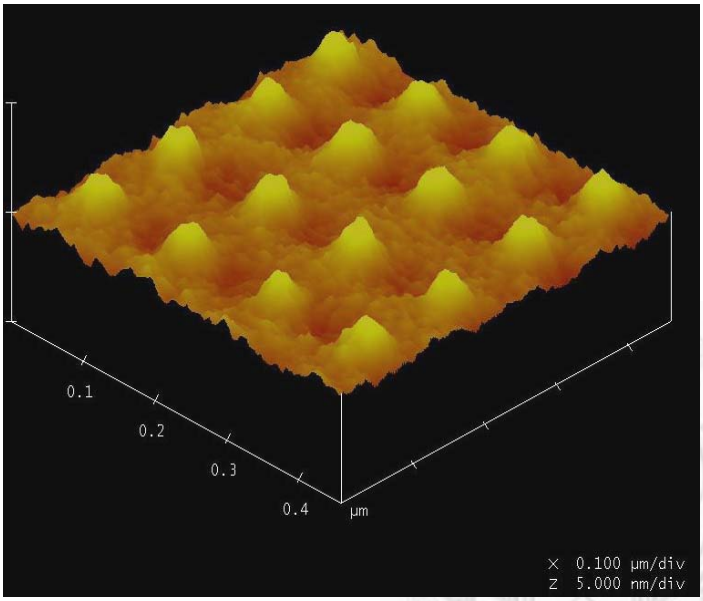

Figure 2.1: 3D AFM image of square lattice (lattice constant = 100 nm) of ordered arrays of protrusions Si (100) substrate created by FIB dose of 2 x 10^{15} ions/cm^2 (dwell time, Δt = 1 ms). Yellow-white bumps mark locations of these FIB created protrusions and partial dark brown areas mark the regions of overlap of tail of FIB.

Average height of these FIB created protrusions starts from 0.5 nm (Δt = 0.2 ms) and reaches a maxima of 1.7 nm (Δt = 2 ms). Further increase of dwell time (Δt) leads to the formation of craters due to ion sputtering of the Si substrate. At dwell time of 12 ms the average depth of craters reaches about 1 nm. Fig. 2.2 shows the variation of protrusion height (crater depth) with dwell time.

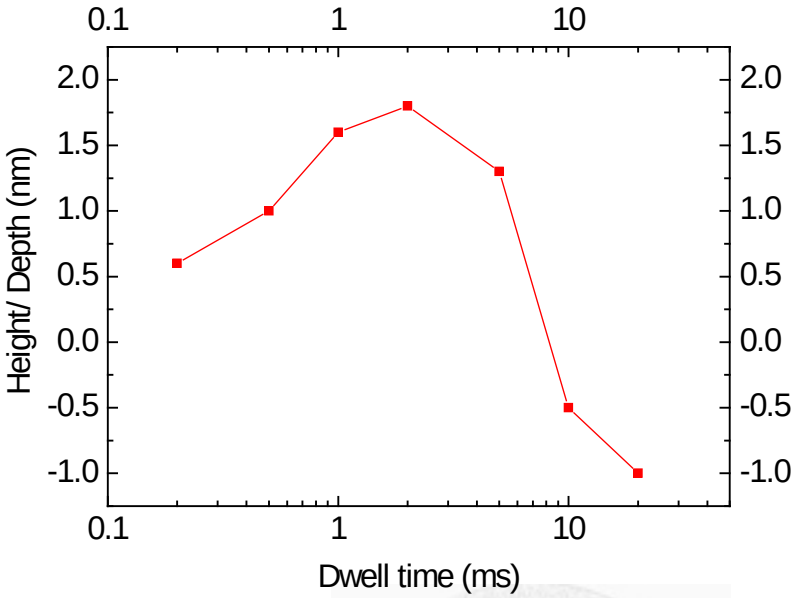

Figure 2.2: Variation of protrusion height (crater depth) with dwell time (Δt).

2.3.2 Self-organized and ordered arrays of Ag nanoparticles

Low temperature deposition of Ag on Si substrates results in formation of self-organized Ag nanoparticles on the Si surface. Fig. 2.3 shows the representative plan view SEM image of the Ag nanoparticles on Si. Size of the nanoparticles varies from 10 to 50 nm with log normal distribution of particle size. For the substrates annealed at temperature below 870 K, randomly distributed and aggregated Ag nanoparticles with mean size of few tens of nanometers are observed as shown in Fig. 2.4. Comparing Fig. 2.3 and 2.4, it is evident that size of Ag nanoparticles gets almost doubled and surface density of particles is also reduced. But ordered arrays of Ag nanoparticles are observed. Annealing temperature of 970 K provides sufficient surface mobility to Ag to move towards FIB created aggregation centers to form ordered arrays of Ag nanoparticles.

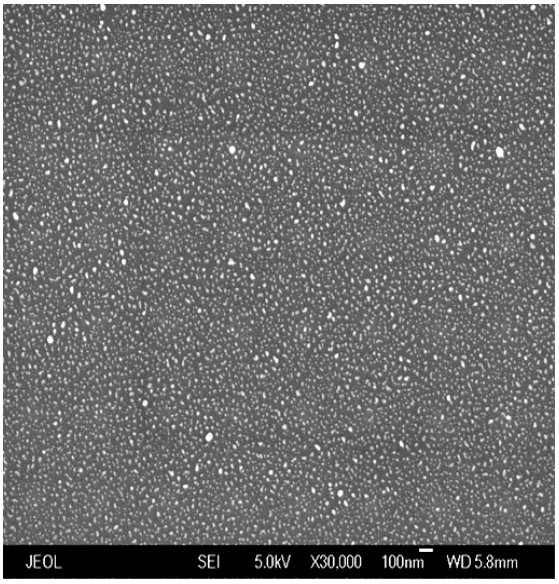

Figure 2.3: SEM image of as deposited Ag on patterned Si substrate.

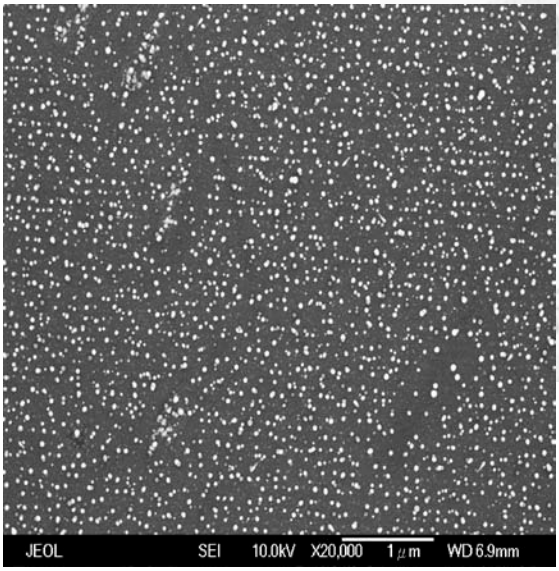

Figure 2.4: SEM image of aggregated Ag nanoparticles when annealing is conducted at temperature below 870 K.

Fig. 2.5(a) and 2.5(b), show SEM image of square and hexagonal-close-packed (HCP) ordered arrays of Ag nanoparticles grown on aggregation centers created by FIB with Δt =1 ms. Typical height of these Ag nanoparticles as measured by AFM is about

20 nm, which is in agreement with cross section TEM image, Fig. 2.14(b). For $\Delta t \leq 0.5$ ms or $\Delta t \geq 5$ ms, Ag nanoparticles of large size variation appear randomly on the surface, as shown in Fig. 2.5(c) and 2.5(d). These observations indicate the existence of an optimum FIB-dose for making a pixel into an effective aggregation center, and the loss of its constraining efficacy when it is under or over exposed to the ions.

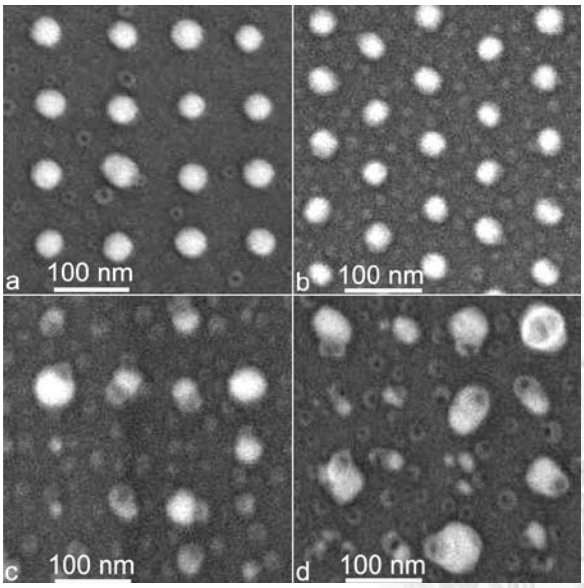

Figure 2.5: SEM images of ordered arrays of Ag nanoparticles formed on Si(100) surface irradiated by FIB (1 ms/pixel) to create a lattice of (a) square and (b) HCP aggregation centers. The ion-induced aggregation centers are not effective for FIB dwell time (c) below 0.5 ms or (d) over 5 ms.

Fig. 2.6 and 2.7 shows the large area view of the square and HCP lattice of ordered arrays of Ag nanoparticles formed on Si(100) surface irradiated by FIB (dwell time = 1 ms/pixel). Both images also show some empty points present among the ordered arrays of Ag nanoparticles. These points are those where FIB missed patterning of the Si substrate on account of beam blanking. Besides the ion dose, the symmetry of the lattice

of aggregation centers and its lattice constant as well as the Ag film thickness also affects the ordering and size uniformity of Ag nanoparticles. As shown in Fig. 2.5(b) and Fig. 2.7, HCP lattice of aggregation centers gives better uniformity because it ensures equal sharing of Ag between the aggregation centers. It is to be noted that constrained self organization yields ordered arrays of Ag nanoparticles only in the patterned area. Outside the patterned area only self organized Ag nanoparticles are found as shown in Fig. 2.8.

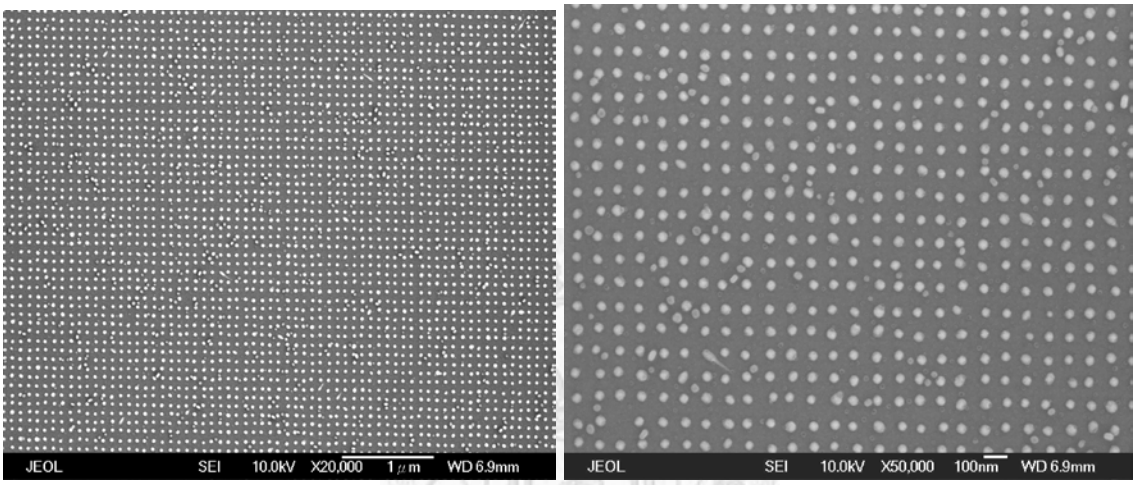

Figure 2.6: SEM images of Square lattice of ordered arrays of Ag nanoparticles.

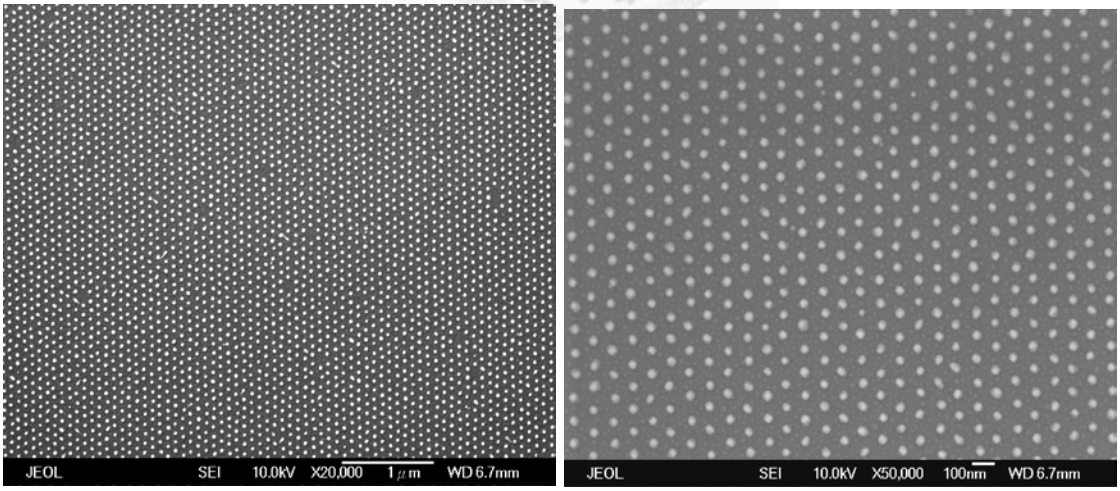

Figure 2.7: SEM images of HCP lattice of ordered arrays of Ag nanoparticles.

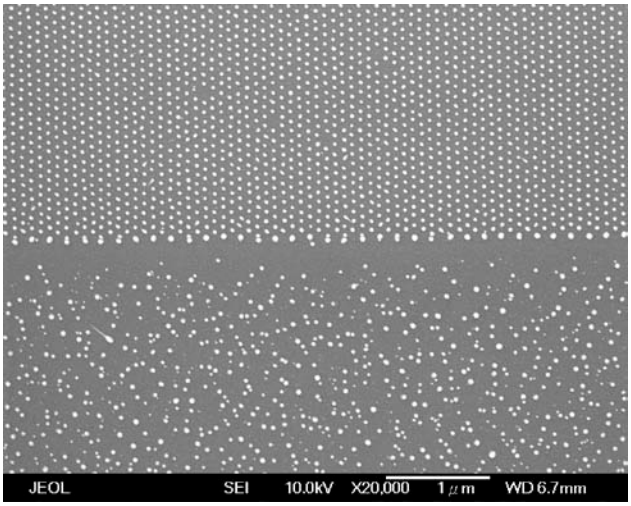

Figure 2.8 SEM image of ordered array of Ag nanoparticles in patterned region (top half) and self organized Ag nanoparticles (bottom half) in non-patterned region.

Fig. 2.9 shows Fourier transform of the SEM images of Ag nanoparticles, shown in Fig. 2.6 and 2.7. Observation of square and HCP lattice points confirms symmetry and long range order of the array of nanoparticles.

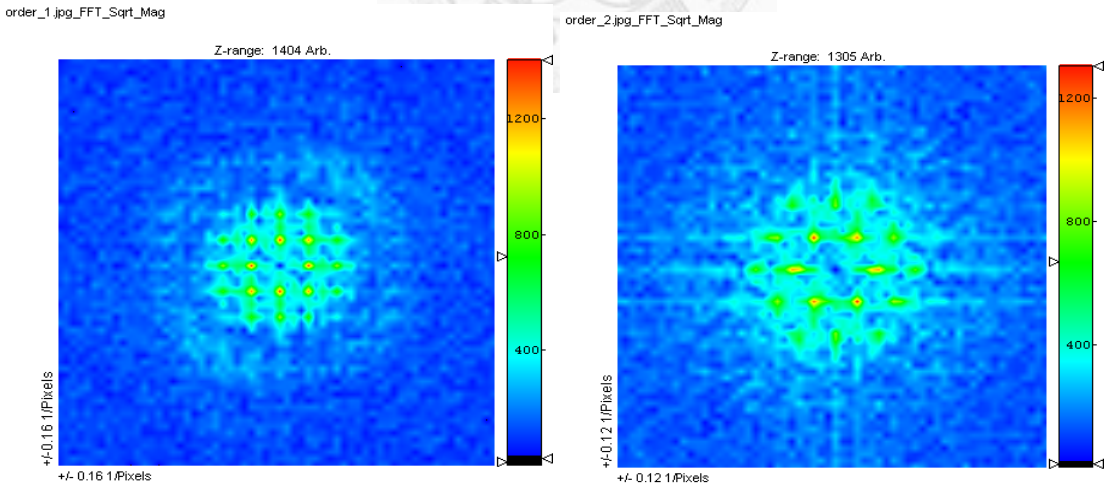

Figure 2.9: Fourier transform of ordered arrays of Ag nanoparticles. LHS image represents square lattice of Ag nanoparticles and RHS image represents HCP lattice of Ag nanoparticles.

Fig. 2.10 shows the effect of increase of lattice constant of the patterned aggregation centers. For an array of aggregation centers with lattice constant of 200 nm and more, many self-organized Ag nanoparticles appear in between the Ag nanoparticles formed by constrained self-organization. On the other hand, aggregation centers with lattice constant much smaller than 100 nm, the tail of the ion beam profile overlaps which results in absence of distinct aggregation sites on Si surface and no ordering of Ag nanoparticles is observed. Fig. 2.11 shows that with decrease of lattice of aggregation centers to 80 nm the loss of order begins.

Deposition of 1 nm of Ag films results in large size distribution in size of ordered arrays of Ag nanoparticles [Fig. 2.12(LHS image)] whereas deposition of 2-3 nm Ag films results in formations of ordered arrays of Ag nanoparticles with about 10% variation in size of nanoparticles (Fig. 2.5 to Fig. 2.8). On the other hand deposition of Ag films with thickness of 5 nm and more leads to the formation of a large number of self-organized Ag nanoparticles with random spatial and size distribution [Fig. 2.12(RHS image)].

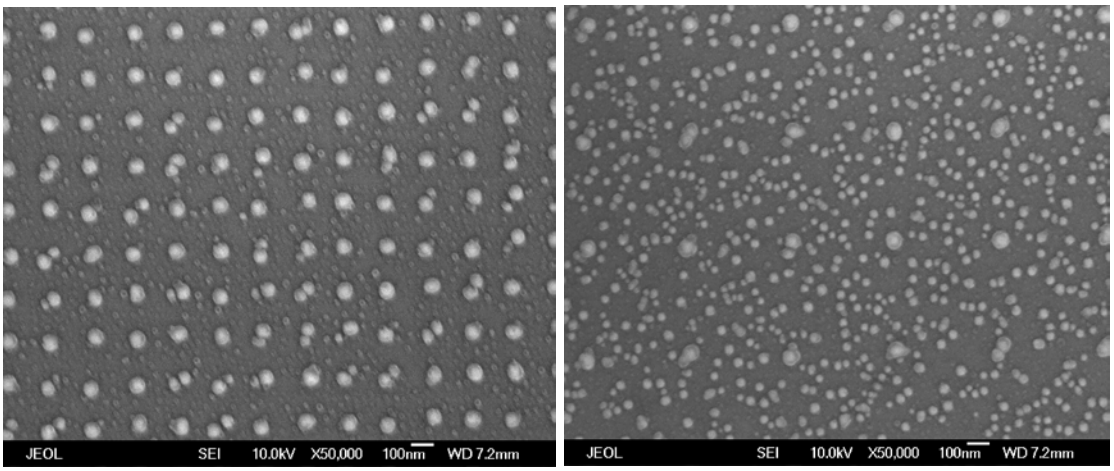

Figure 2.10: SEM images of ordered and self organized Ag nanoparticles. Lattice constant of aggregation centers is 200 nm for LHS image and 500 nm for RHS image.

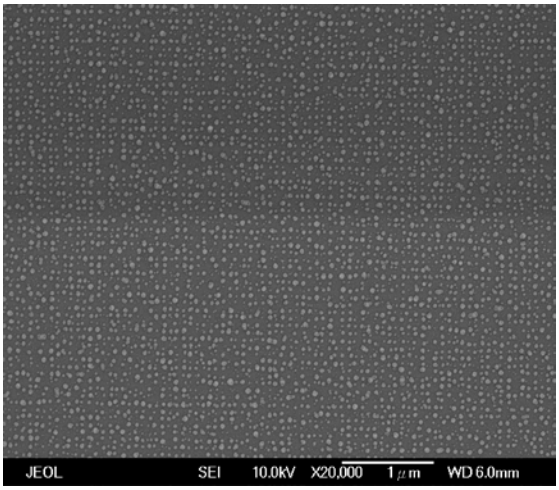

Figure 2.11: SEM image of Ag nanoparticles formed when lattice of aggregation centers is reduced to 80 nm.

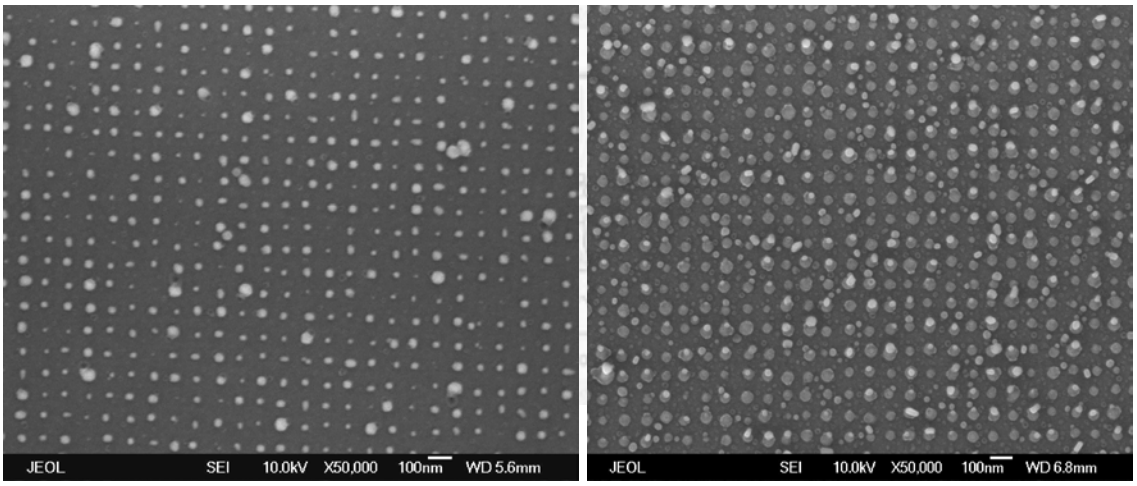

Figure 2.12: SEM images showing effect of deposited Ag thin film thickness on size distribution of ordered arrays of Ag nanopartilcles. LHS morphology is observed when 1 nm of Ag film is deposited and RHS morphology is observed when 5 nm of Ag film is deposited.

Therefore, to create an ordered array of Ag nanoparticles of a given size, the symmetry and lattice constant of the constraining lattice, FBI dwell time of the aggregation centers, and Ag thin film thickness must be carefully matched.

To quantify the efficacy (η) of ion beam irradiation to constrain the surface migration of Ag , η is defined as $N_c/(N_c + N_r)$, where N_c is number of Ag nanoparticles at aggregation centers created by ion beam irradiation and N_r is number of particles at random locations (N_c+N_r equals the total number of particles in a field of view). Fig. 2.13 shows the variation of η with Δt. For Δt below or about 0.2 ms, η remains zero because the number of defects in each FIB-irradiated pixel is not adequate to constrain the surface migration of surrounding Ag. With increase of Δt, η first increases in a linear fashion till it reaches its maximum value of 90% at Δt =1 ms and then starts to decrease drastically. The decrease of η for longer Δt is expected since the tail of the ion beam profile gradually exposes the region between two neighboring pixels and eventually covers the entire surface, leaving no pristine Si surface on which the Ag can migrate more freely.

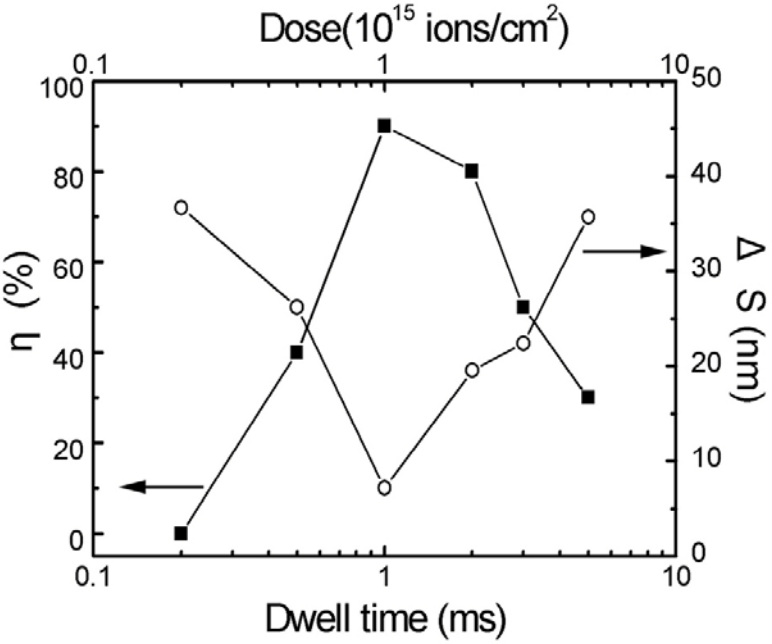

Figure 2.13: Efficacy (η) of aggregation centers (see text) and size variation (ΔS) of Ag nanoparticles as a function of FIB dwell time per pixel.

An important byproduct of constraining the Ag self-organization process by an ordered array of aggregation center is the decrease in the size variation (ΔS) of the nanoparticles. As shown in Fig. 2.13, ΔS and η exhibit a clear anti-correlation and the minimum of ΔS (about 10% of the mean size) occurs at Δt =1ms, which coincides with the maximum of η. For comparison, size variation (ΔS) for Ag nanoparticles formed on the pristine region is more than 50% of their mean size, which indicates significant improvement in the uniformity of Ag nanoparticles in an ordered array.

The structure and composition of Ag nanoparticles is revealed by cross-section TEM (transmission electron microscope) images and EDX (energy dispersive x-rays) spectra of nanoparticles. Ag nanoparticles formed on a pristine Si surface, as shown in Fig. 2.14(a), consist of Ag with well defined interface between Ag nanoparticles and substrate surface. In contrast, Ag nanoparticles formed on the ion-irradiated locations, as shown in Fig. 2.14(b), have inverted pyramids of strained Si underneath, which exhibit clear {111} interfaces with the surrounding Si. The EDX spectrum of the Si under the Ag nanoparticles on a pristine surface shows no detectable amount of Ag. This observation is in agreement with negligible solubility of Ag and Si in solid phase. On the other hand, the strained Si under the Ag nanoparticles on the ion-irradiated aggregation centers contains significant amount of Ag (30% atomic concentration), indicating enhanced diffusion of Ag into the ion-irradiated Si during annealing. The apparent diffusion range of Ag ($\approx$20 nm), estimated from Fig. 2.14(a), is in agreement with longitudinal penetration depth of Ga^+ ions as calculated by TRIM code simulations [81].

Based on the TEM and EDX data, we propose that during the annealing process, significant amount of Ag diffuses into the amorphized aggregation centers created by ion

irradiation. As the Si recrystallizes, the embedded Ag induces strain in a local region of the Si, while the remaining Ag on the surface forms the hemispherical nanoparticle. Our proposal is supported by the TRIM code simulations [81], according to which approximately 700 vacancies are created by impact of a single 50 KeV Ga^+ ion. Since each aggregation centre is exposed to ~10^4 Ga^+ ions for Δt =1 ms, the average number of defects in each ion-irradiated pixel is of the order of 10^6~ 10^7. Such a large number of defects attract the migrating Ag and some amount of the Ag diffuses into the amorphized region to form the strained-Si structure during the annealing process. When the diffusion process is terminated by the Si recrystallization, the remaining Ag can form the nanoparticle on top of the strained Si.

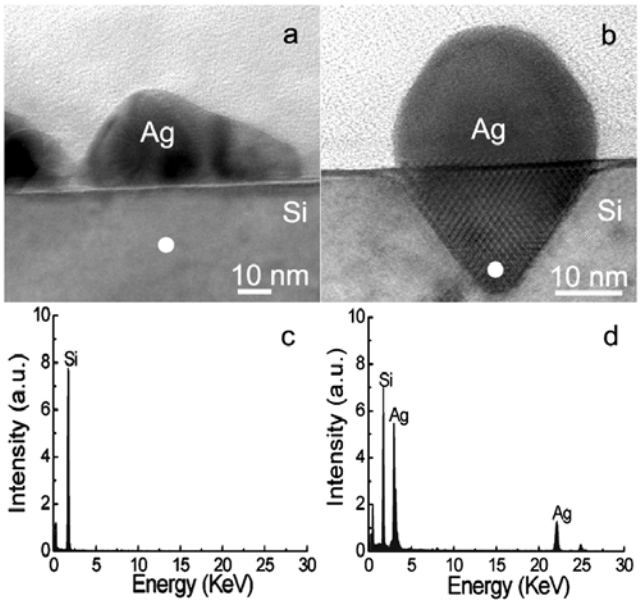

Figure 2.14: Cross section TEM images of Ag nanoparticles formed on (a) pristine region and (b) ion irradiated location. (c) and (d) show the corresponding EDX spectra of the substrate (white spots) under the nanoparticles.

Chapter 3 Probing surface plasmon of individual Ag nanoparticles by STEM

3.1 Aim

Surface plasmons (SPs) are quantized collective plasma oscillations of conduction electrons propagating at the surface of metals [82-84]. The excitations of SPs by the dipolar electric field of light in the visible spectral regime dictate the color of noble metals [85].

In noble metal nanoparticles (NPs) with only a few tens or hundreds of nanometers, SPs tailored by the sizes, shapes, and electric near-field couplings of the NPs determine their optical properties ranging from near-infrared to visible spectral regimes as demonstrated in nanoprisms [89], nanorings [90], nanostars [91], (coupled) nanorods [86, 92], and (coupled/arrayed-) nanospheres [87, 93-97]. In individual and/or coupled NPs with designated geometrical constraints, SPs can then be tuned to the proximity of the laser energies/wavelengths conventionally available [24]. The associated resonant excitations have been shown to open up vast opportunities for many fascinating applications of the NPs such as plasmonics [24,98] and molecular sensing by surface enhanced Raman scattering (SERS) [94,36]. It has been noted that these novel applications are closely correlated with the SPs characteristic and their near-field distributions in each individual nanomaterial [87, 91, 24]. The corresponding spectral characterization requires spectroscopy techniques with a nanometer-scale spatial

resolution that is, however, difficult to achieve even by advanced nanoprobe-based scanning near-field optical microscopy (SNOM) [99].

An electron beam can excite SPs like light by coupling its electromagnetic field to the evanescent electric fields of SPs, and results in electron energy losses [100-102]. The sub-nanometer-scale electron beam in a scanning transmission electron microscope (STEM), therefore, provides us with an unmatched nanometer-scale resolution and energy range in investigating SP characteristics of individual NPs, spectrally and spatially, when used in conjunction with electron energy-loss spectroscopy (EELS), i.e., the combined technique of STEM-EELS [89, 100, 103]. Using STEM-EELS, the spatially resolved probing of SPs in individual Ag nanoprisms [89] and individual and coupled Au NPs [103] in the visible spectral regime has been demonstrated.

Here, we address the experimental and theoretical aspects of surface excitations in individual Ag NPs (~30 nm) grown on Si(100) substrates in the ultra-violet spectral regime that can only be marginally probed by optical approaches and is less understood accordingly [89, 100]. All experimental results show good agreement with the theoretical calculations [102,104]. The spatial distributions of the surface excitations on the NPs have been also mapped out, exhibiting a dipolar-dominant character of the SP at 3.5 eV with prominent near-field enhancements.

3.2 Experiments

3.2.1 Ag nanoparticles on Si by constrained self organization

In a post-deposition annealing process, the Ag deposited at low temperature on a Si(100) substrate aggregates to regions that have been exposed to adequate dose of

energetic ions. By patterning an array of such aggregation centers on the substrate, using a 50 KeV focused Ga^+ ion beam, the migration of Ag on the patterned area during the subsequent annealing is constrained and ordered arrays of Ag nanoparticles with uniform size distribution are formed spontaneously. Related experimental details have been described in chapter 2 and reference [3].

3.2.2 STEM probing of Ag nanoparticles

The STEM-EELS investigations of the Ag NPs grown on Si(100) were performed on a field-emission STEM, FEI Tecnai F20, operated at 200kV and equipped with a Gatan Tridiem 865 EELS spectrometer. The electron energy resolution (defined by the line-width of the zero-loss peak, ZLP) and beam size exploited throughout the work were ~0.66 eV and ~0.2 nm, respectively. The growth of the arrayed Ag NPs (size, ~30 nm; gaps between NPs, ~50 nm) by focused-ion-beam patterning of Si substrates and post-annealing of Ag films on the patterned substrates has been reported in a chapter 2. The Ag-NPs/Si samples for STEM-EELS studies were prepared by the standard mechanical and ion-milling thinning technique and, subsequently, subject to HF and repeated plasma cleanings before the investigations in order to improve the sample surface cleanness.

3.3 Results and discussion

3.3.1 3D tomography of Ag nanoparticle

Fig. 3.1(a) illustrates the typical TEM image of an individual Ag NP among the arrays. The upper part of the NP in vacuum shows a hemisphere-like geometrical

configuration and negligible carbon contamination, while the lower part embedded in Si is characterized by a V-shape grove defined by the {111} faces of Si [3].

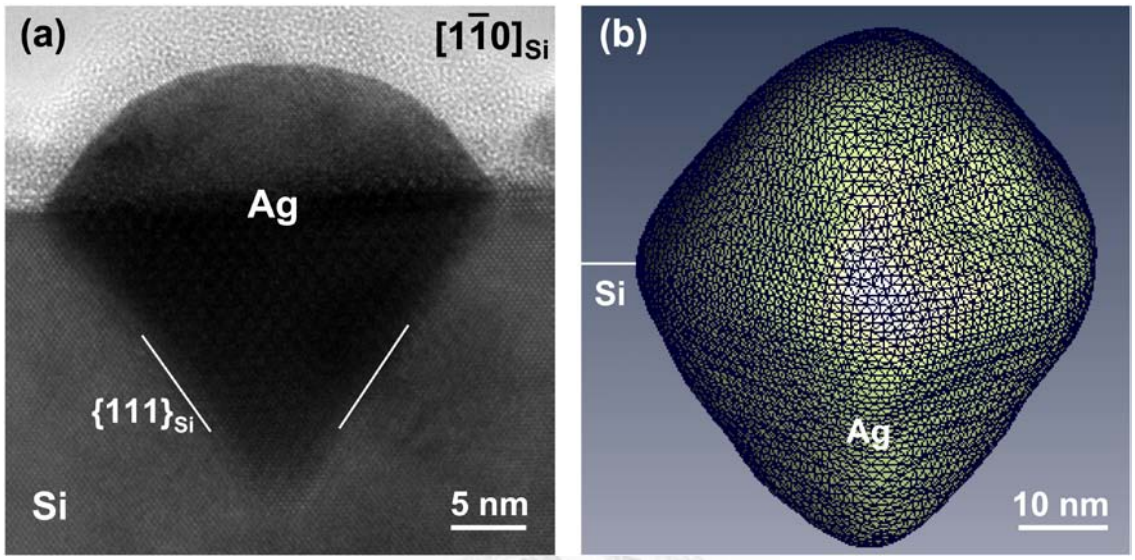

Figure 3.1: (a) TEM image of an individual Ag NP grown on Si(100), acquired along the $[1\text{-}10]_{Si}$ projection. (b) Three-dimensional imaging of such an individual Ag NP using STEM electron tomography.

STEM electron-tomography experiments (sample tilting from -65° to + 65°) were performed on several NPs and Fig. 3.1(b) exhibits the corresponding three-dimensional tomography image of a NP. From Fig. 3.1(b), it is obvious that the conventional TEM thinning technique does not flatten the NPs to two-dimensional thin-slab-like shapes as what thinning usually does, and the $\{111\}_{Si}$-type facets of the NPs (lower part) and the smoother hemisphere-like head (upper part) are now clearly revealed. These geometrical characteristics are essential for the following SP investigations considering the difference between the SP-excitation energies of thin Ag slab, ~3.7 eV (~335 nm) [105], and

spherical and hemispherical Ag NPs, ~3.5 eV (~355 nm) [106], in the ultra-violet spectral regime.

3.3.2 STEM-EELS spectra of Ag nanoparticles

Fig. 3.2(a) shows the STEM-EELS spectra acquired at different locations of the Ag NP (black, red, green, and blue curves), and a spectrum at 1 nm from the Si surface and ~20 nm from the edge of the NP was also taken (purple curve). It should be pointed out that the mean gap spacing, ~50 nm [3], between neighboring NPs is too large to exhibit any noticeable SP coupling between the Ag NPs (gaps of at least ten nanometers are necessary for effective coupling [24]). Positioning the electron beam at the core of the Ag hemisphere-like head (black curve, Fig. 3.2(a)), a broad maximum at ~8.5 eV (~146 nm) and a weaker maximum around ~3.8 eV (~326 nm) characteristic to the bulk plasmon excitations of Ag were observed [107]. Further positioning the electron beam at an impact parameter of 1 nm from the NP surface (similar to optical near-field setup and propitious for the coupling to surface excitations [100]; red curve, Fig. 3.2(a)), we observed the prominent SP resonance of Ag around ~3.5 eV (~355 nm), in good agreement with the reported value for hemispherical Ag NPs [106]. A broad surface excitation was also revealed at ~7 eV (~177 nm; red curve, Fig. 3.2(a)), where the real part of the complex dielectric function of Ag is still negative [105,107], suggesting its SP character [100]. With the further increase in impact parameters for STEM-EELS probing (3 nm, green curve; 6 nm, blue curve; Fig. 3.2(a)), the SP excitation around ~3.5 eV finally approaches 3.5 eV, accompanied with a red-shift of nearly 1 eV for the broad spectral intensity at ~7 eV.

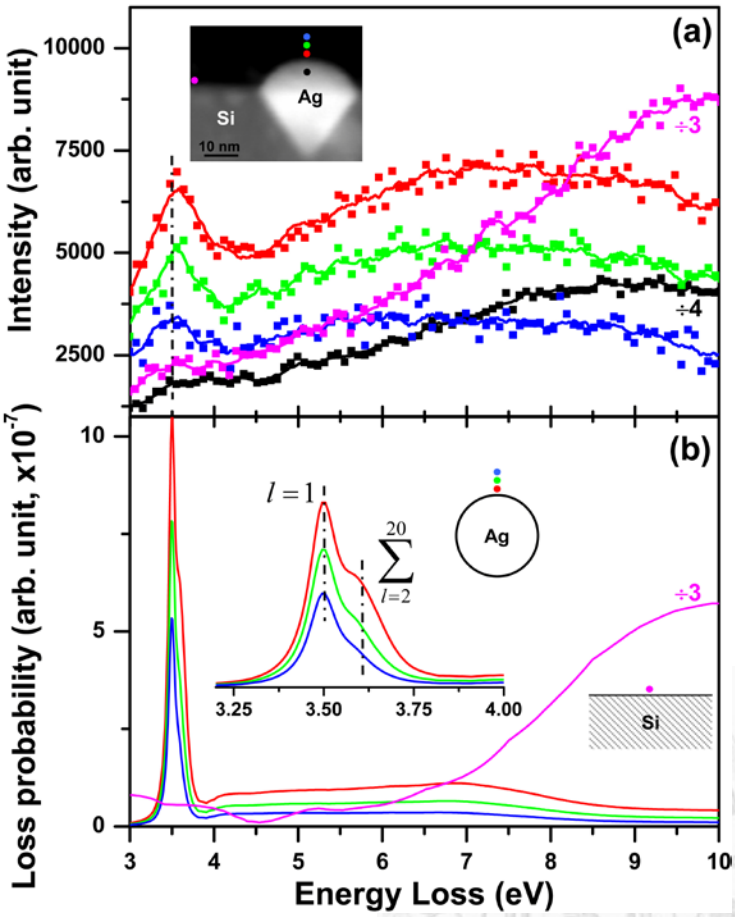

Figure 3.2: (a) The STEM-EELS spectra acquired at different locations of the Ag NP and the Si substrate (inset). All spectra were first aligned and normalized to the ZLP of the red curve (1 nm from the Ag NP surface), and the ZLPs were then deconvoluted from the spectra. The spectrum taken at 1 nm from the surface of Si (~20 nm from the edge of the NP; purple curve) and that taken at the core of the Ag NP (black curve) were divided by 3 and 4, respectively, to fit into the scale of the figure. Green (blue) curve, the spectrum acquired at 3 (6) nm from the Ag NP surface. (b) The calculated impact-parameter dependent STEM-EELS spectra for an individual Ag nanosphere (radius, 15 nm) and a Si film. The insets show the blowup of the region below 4.0 eV and the geometrical constraints used for the calculations. The purple curve was divided by 3 to fit into the scale of the figure.

In *spherical* NPs, an impact-parameter dependent red-shift of surface excitations, such as that observed in Fig. 3.2(a), is well known to arise from the frequency-dependent multipolar polarizability $\alpha_l(\omega)$ of the NP and can be expressed as the equation below in the non-retarded, electrostatic limit [104].

$$\alpha_l(\omega) = \frac{l[\varepsilon(\omega) - \varepsilon_m(\omega)]}{l\varepsilon(\omega) + (l+1)\varepsilon_m(\omega)} a^3$$

where $\varepsilon(\omega)$ and $\varepsilon_m(\omega)$ are the respective complex dielectric functions of the NP and the bound medium (vacuum here, ε_m =1), a is the radius of the NP, and l is the mode quantum number (l=1, dipole mode; l=2, quadruple mode; etc.). The surface-excitation energy $\hbar\omega$ ($\hbar = h/2\pi$; h, the Planck's constant) taking place at the divergence of $\mathrm{Im}\{\alpha_l(\omega)\}$ evolves with the increase in l [104], while the near-field extension of the given l mode into free space inversely scales with the energy as v/ω (v, the electron velocity; 0.7c at 200 kV; c, the speed of light) [100, 108]. This near-field scaling thus suggests that a large impact parameter would favor a surface excitation with a lower eigenenergy due to its larger v/ω, giving rise to the impact-parameter dependent red-shift of the surface spectral features [100]. In hemispherical [109] or supported spherical objects with non-conducting substrates (such as Si here) [110], the thorough numerical STEM-EELS investigations considering all multipolar components have indicated that probing the objects at their apical locations (i.e., red, green, and blue curves in Fig. 3.2(a)) can lead to surface excitations in resemblance to those of the bare spherical counterpart. We thus performed the non-retarded STEM-EELS calculations for bare Ag nanospheres using the impact-parameter dependent analytical equation on the basis of $\alpha_l(\omega)$ [104], which is computationally efficient, compared to the lengthy numerical

evaluations in Refs. [109] and [110] and faithfully catches the physics for the impact-parameter dependent red-shift and the related SP characteristics observed in Ag NPs (Fig. 3.2(a)).

Fig. 3.2(b) shows the calculated impact-parameter dependent STEM-EELS spectra for an Ag nanosphere (a=15 nm, estimated from Fig. 3.1(a)) and a Si film, and we have considered the contributions of high-order l up to 20 for the Ag-NP calculations. Integrations of even higher order l do not lead to visible changes in the scale of the figure as a result of their negligible contributions to the current small NP [104]. In addition, the criterion for the electrodynamics retardation, $a \cdot \omega / v > 1$ [108], is not fulfilled in the spectral range that we are interested in (< ~10 eV), justifying our exploitations of the non-retarded calculations for Ag NPs [104].

Comparing Fig. 3.2(a) to Fig. 3.2(b), it is obvious that the experimentally observed SP peak at ~3.5 eV eventually consists of a dominant dipolar SP component at 3.5 eV and contributions from all higher order modes (shoulder, 3.6 eV) as shown in the inset of Fig. 3.2(b). With the increase in impact parameters from 1 (red curve) to 6 nm (blue curve, Fig. 3.2(b) and inset), the high-order shoulder rapidly decays as a vanishing spectral feature due to the v/ω scaling, whereas the dipolar contribution remains predominant. The energy resolution of our STEM-EELS instrument is, however, not sufficient to distinguish the two bands, only 0.1 eV apart (inset, Fig. 3.2(b)). From experimental aspects, the summation of both bands then leads to a gently blue-shifted SP feature from 3.5 eV at the impact parameter of 1 nm (red curve, Fig. 3.2(a)). Upon increasing impact parameters, the predominant excitations for the dipolar SP at 3.5 eV (inset, Fig. 3.2(b)) thus account for the experimentally observed red-shift to 3.5 eV in Fig.

3.2(a) (green and blue-shift curves). In the calculations (Fig. 3.2(b)), the spectral red-shift of the ~7-eV excitation to ~5~6 eV arisen from the impact-parameter dependent excitations of the SP multipolar components was also revealed, consistent with Fig. 3.2(a). Indeed, the agreement between experiments (Fig. 3.2(a)) and calculations (Fig. 3.2(b)) for the Ag NPs is satisfactory and firmly establishes the SP multipolar nature for the surface excitations, ~3.5 and ~7.0 eV, in the ultra-violet regime. The calculations on the basis of a spherical NP, though simple, have unraveled the origin for the impact-parameter dependent spectral red-shift in Fig. 3.2(a). Nevertheless, the Ag-NP calculations appear to under-estimate the broad spectral intensities near ~7 eV, possibly due to effects of the Si substrate. For further inspections, we then performed impact-parameter dependent calculations for the Si film (1 nm from the surface; purple curve, Fig. 3.2(b)) [102]. The calculation shows a good agreement with the experiment (purple curve, Figs. 3.2(a) and 3.2(b)), and Si actually displays appreciable surface contributions above ~6 eV. This later characteristic may contribute to the intense surface feature of Ag NPs near ~7 eV (Fig. 3.2(a)), while an unambiguous determination of its origin requires more realistic calculations taking into account the actual sample geometry, which is beyond the scope of this work.

3.3.3 STEM-EELS mapping of surface plasmons of Ag nanoparticle

Figs. 3.3(a)-(c) illustrate the STEM-EELS mapping of the spectral features at 3.5, 7.0, and 9.0 eV (~138 nm), respectively. The spectral mapping was performed by rastering the electron beam on the material in a mesh by mesh manner (2×2 nm per mesh) [89, 100, 103]. After aligning ZLPs acquired at each mesh, the spectral amplitudes of the

given surface excitations were then used to map out their respective spatial distributions [89, 100, 103]. It has been well established that the STEM-EELS mapping nicely mimics the electric near-field distributions of the surface excitations, in particular, the near-field enhancements at local geometrical constraints [89, 100, 111].

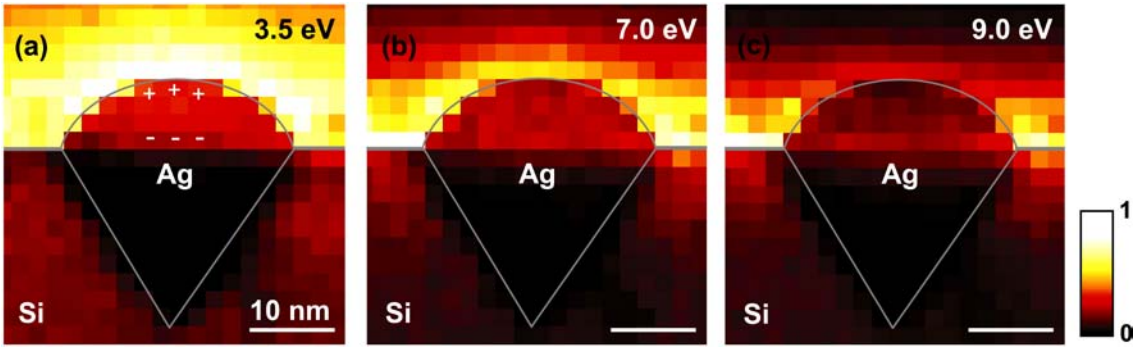

Figure 3.3: STEM-EELS mapping of (a) 3.5-, (b) 7.0-, and (c) 9.0-eV surface resonances in the material with the contrast maxima signifying the most prominent excitation locations for the given spectral features. The positive and negative signs in (a) denote the dominant dipolar character of the near-field features. The mesh dimension is 2×2 nm, and the Ag NP and Si surface are outlined by gray lines. Color scale bar, the linearly normalized image contrast.

In the STEM-EELS map of the 3.5-eV SP (Fig. 3.3(a)), the contrast maximum localized at the top of the Ag NP is characteristic to a dipole-like near-field character (see the schematic positive and negative signs) [87], in perfect consistence with the determination of the dipolar SP nature at 3.5 eV (Fig. 3.2). Moreover, such a contrast-maximum feature (Fig. 3.3(a)) is representative of the local SP near-field enhancements [87,111] and might thus be of practical interests for future plasmonics and SERS applications. At 7.0 eV (Fig. 3.3(b)), the surface of the Ag NP is imaged by sharp

contrasts as expected for surface excitations like Fig. 3.3(a), evidencing again the SP character of this peak. In Fig. 3.3(b), the contrast maxima are, however, localized on the Si surface, signifying the aforementioned appreciable Si contributions above ~6 eV (Fig. 3.2). At 9.0 eV, the surface excitations of Si predominate over those of Ag (Fig. 3.2) and the corresponding spectral mapping indeed faithfully reflect the contrast maxima on the Si surface (Fig. 3.3(c)). The spatial resolving power established in the above STEM-EELS mapping is superb considering that state-of-the-art nanoprobe-based SNOM could not resolve the field distribution around the Ag NP beyond its spatial resolution and, more importantly, the introduced electromagnetic interaction between its nanoprobe and the plasmonic entity may influence the physical interpretation [99]. It should be also pointed out that the contrast delocalization into vacuum in Fig. 3.3 represents the near-field extension into free space for the surface excitations (proportional to v/ω) [100] and decreases with the increasing surface-excitation energy as expected.

Chapter 4 Fabrication of Singlet, doublet, and triplet of Ag nanoparticles in AAO

4.1 Aim

Arrays of closely packed Ag nanoparticles with sub-10 nm interparticle gaps are routinely used in applications like plasmonics [24, 36, 98] and molecular sensing by surface enhanced Raman scattering (SERS) [94, 36, 117]. Ordered arrays of singlet, double, and triple Ag nanoparticles are good candidates for studying surface plasmon hybridization [88], surface plasmon dispersion relations [112], fundamental interactions of surface plasmons [27, 98, 113], light scattering from nanoscatterers [114], near-field studies [115], plasmonic coupling of noble metal nanoparticles [24, 131, 132].

Many methods for the synthesis of Ag nanoparticles have been reported in the literature and can be arbitrarily divided into traditional and non-traditional categories [116]. Traditional methods include reduction of Ag salts with aid of reducing agents like $NaBH_4$ or sodium citrate. Due to the large positive reduction potential of Ag, nanoparticles oxidation is thermodynamically unfavorable resulting in quite stable aqueous and suspensions without the aid of capping ligands. Aggregation can be inhibited by the thick electrical double layers that form around metal nanoparticles in low-ionic-strength suspensions. For high ionic strengths or organic-phase suspensions, capping agents such as self-assembled monolayers [117], surfactants [118], polymers [119], and dendrimers [120] can be employed to protect the particles from aggregation. If the synthesis is carried out in the presence of capping agents, however, anisotropic

particles may result due to the differing affinities of the ligands to the exposed crystal faces [121]. This is sometimes a desired effect and several researchers have shown that various shapes can be produced through judicious use of stabilizing agents. Alternatively, nanoparticles can be capped with desired molecules after the synthesis to facilitate their transfer into nonpolar phases or to tailor their surface chemistry. Non-traditional synthesis methods include Ag particle synthesis through high-temperature reduction in porous solid matrices [122], electrochemical growth into porous anodic alumina [3], vapor-phase condensation of a metal onto a solid support [123], laser ablation of a metal target into a suspending liquid [124], photoreduction of Ag ions [125], electrolysis of an Ag salt solution [126, 127], electron beam lithography (EBL) [128, 129], and constrained self organization [3], and directed self assembly of nanoparticles [130].

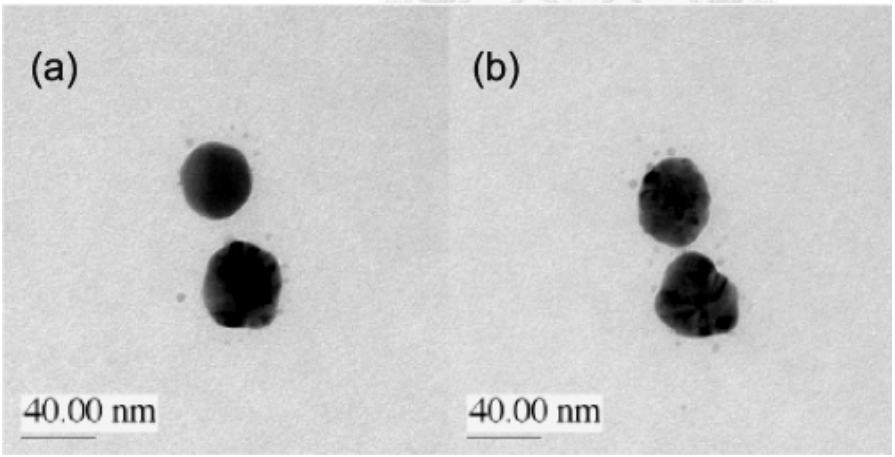

Figure 4.1: TEM images of dimers of Ag nanoparticles fabricated using EBL [128].

Dimers and trimers of Ag nanoparticles can be formed by electron beam lithography [128, 129], interaction of functionalized Ag nanoparticles with a surface which has been functionalized with a chemical group complimentary to that of Ag nanoparticles [133] and by molecular bridging of two (three) nanoparticles [134, 135].

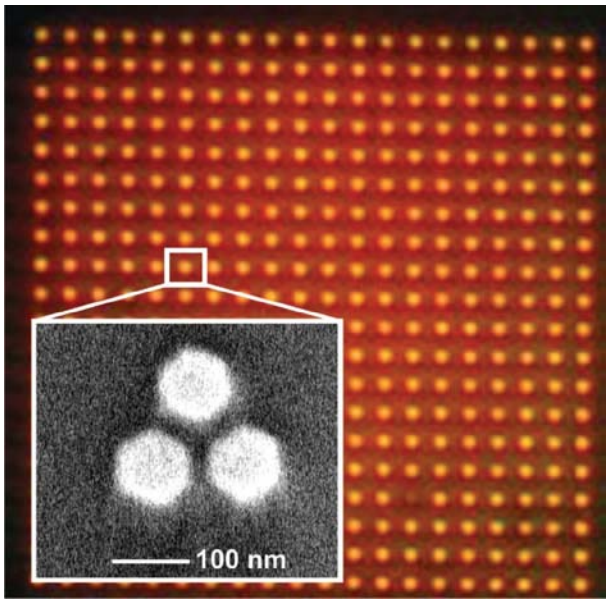

Figure 4.2: Dark field microscopy image of trimers of Ag nanoparticles. Inset shows the SEM image of one representative trimer [129].

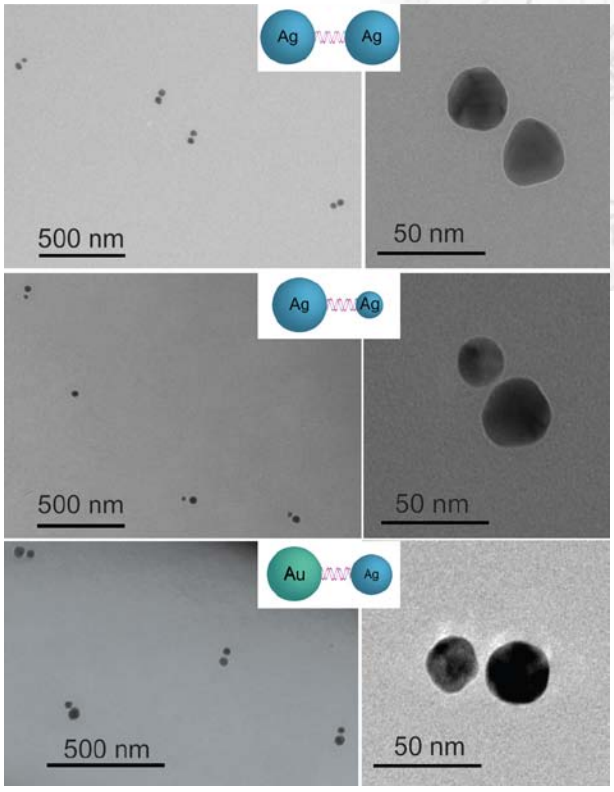

Figure 4.3: TEM images of dimers of noble metal nanoparticles formed by molecular bridging [135].

However, it is not easy to fabricate Ag nanoparticle dimmers (trimer) with sub 10 nm gap using electron beam lithography. And though the molecular bridging method yields nm control over the interparticle gap, it is not easy to fabricate ordered arrays of dimmers (trimers) with known positions.

AAO is a good template for growth of arrays of nanoparticles and nanowires [36-41]. Custom-designed arrays of AAO nanochannels (CDA) [136] have been used for growth of nanowires arrays comprising of multiple elements [137]. CDA can be fabricated by bombardment of AAO nanochannels with high energy Ga^+ focused ion beam (FIB). Ion beam sputtering and material redeposition results in formation of a capping layer on the bombarded region. This capping layer is compact and impervious to water (electrolyte) and its thickness depends on the FIB energy (Fig. 4.4). Capping layer can be opened using low energy (5-10 KeV) ion beam sputtering. This energy dependent closing and opening of AAO nanochannels assists in growth of nanowires arrays comprising of multiple elements as discussed in Ref. 137 and shown in Fig. 4.5.

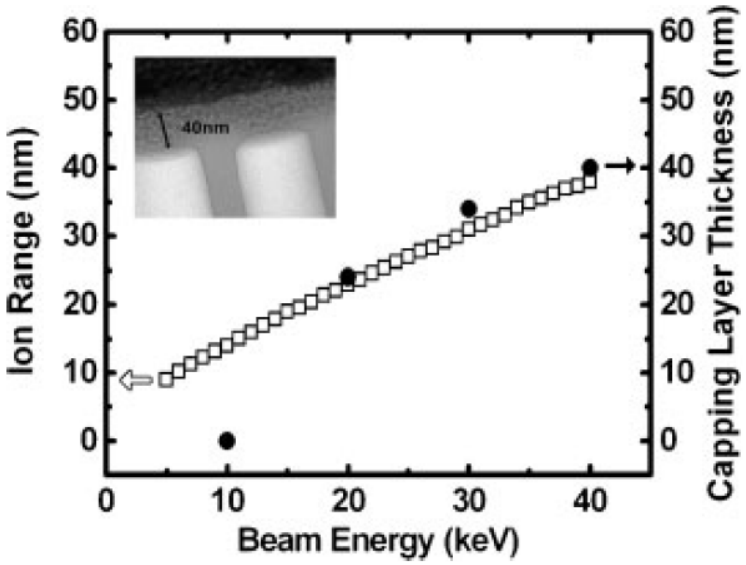

Figure 4.4: Variation of the capping layer thickness (nm) with FIB energy (KeV) [137].

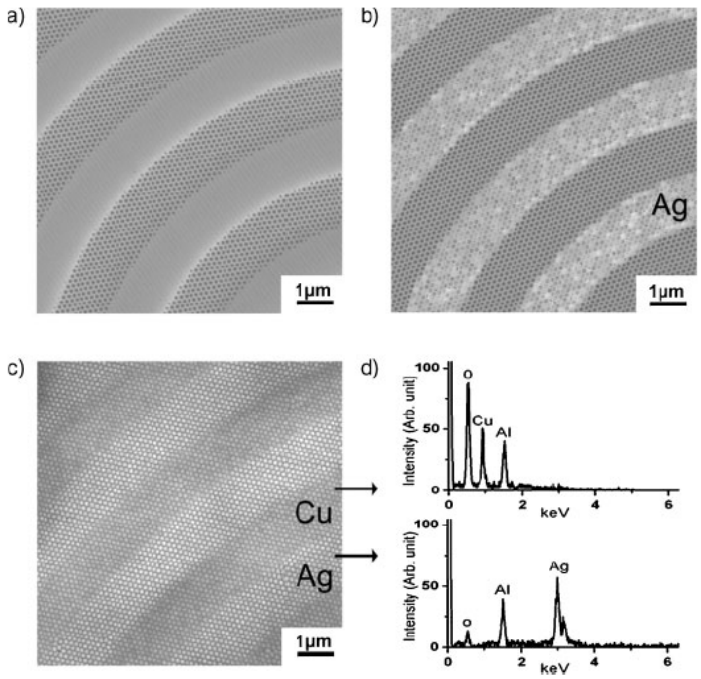

Figure 4.5: Growth of arrays of nanowires comprising of different elements. (a) SEM image of closed nanochannels. (b) Top-view image of arrays after Ag electrodeposition and reopening of closed nanochannels. (c) Back-view images of arrays after Cu electrodeposition into opened nanochannels (d) EDX spectra of Ag and Cu nanowires [137].

It is possible to selectively close AAO nanochannels in such a way that single, or double or triple AAO nanochannels are left open and surrounding nanochannels are closed by FIB bombardment [136, 137]. After that Ag can be electrochemically deposited into these open nanochannels. These custom designed AAO templates allows control over the position of the grown Ag nanoparticles and interparticle gap. FIB patterning will define the exact position of the grown single, double or triple nanoparticles and thickness of wall of AAO can be tuned from several tens of nm to few nm which yields very closely positioned Ag nanoparticles. Therefore, we decided to electrochemically grow singlet, doublet, and triplet of Ag nanoparticles in custom designed AAO templates.

4.2 Experiments

4.2.1 Two-step growth of AAO nanochannels

High-purity (99.99%) annealed aluminum foils were electropolished in a mixed solution of 50 wt% 1:1 (v/v) $HClO_4/C_2H5OH$ at 5 ºC under constant stirring until the root mean square (rms) roughness of a typical 10 µm x 10 µm area was ca. 1 nm, as measured by an atomic force microscope operated in contact mode. Two different AAO templates with different lattice constants of AAO nanochannels were grown by two-step anodization process. Al foils were separately anodized in 0.3 M sulfuric acid solution at 1 ºC at a constant voltage of 12 V and 20 V. After anodizing for 2 hour, the formed AAO were removed using a mixture solution of Chromic acid (CrO_3) and phosphoric acid (H_3PO_4) (CrO_3 = 0.5 gm, H_3PO_4 = 3 ml, H_2O = 50 ml). AAO removal rate is about 7.5 µm in 2 hours at 50 ºC (measured temperature). After removal of AAO the concaves of Al were left behind on the Al foil surface. After that second anodization is conducted under the same anodizing conditions for 3 min to grow about 50-60 nm long AAO nanochannels. Fig 4.6 shows the schematic of the two-step anodization process.

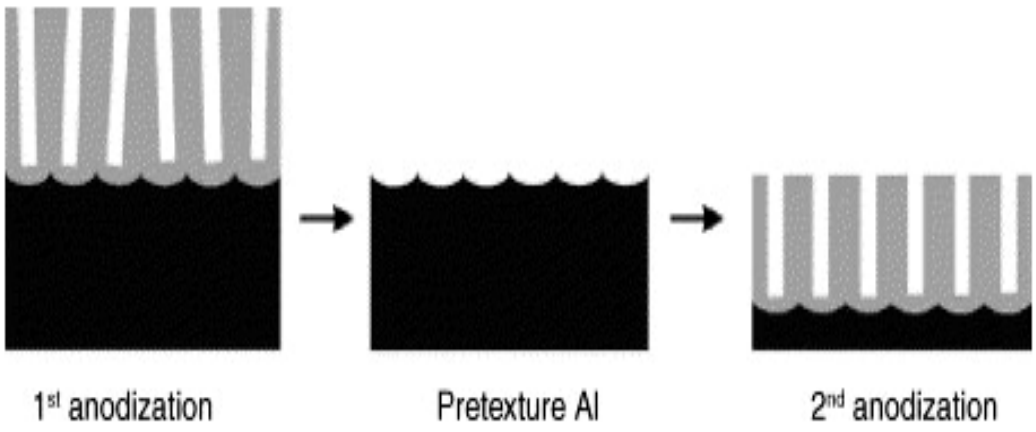

Figure 4.6: Schematic of two-step anodization process [31].

4.2.2 Focused ion beam patterning of AAO

To be able to close the formed AAO nanochannels, the ratio of AAO wall thickness (w) to pore diameter (d) should be 0.7 or more. If w/d is below 0.7 the AAO nanochannels can not be closed and only sputtering of AAO will be observed because closing of nanochannels relies heavily on redeposition of material from side walls. Therefore, the formed AAO nanochannels were opened using a 6 wt% solution of H_3PO_4 at room temperature to obtain AAO substrates with arrays of nanochannels having the specific pore diameter and spacing. AAO pore widening rate is 1.5 to 1.7 nm at 25 ºC.

FIB pattering of AAO was conducted using 30 KeV Ga^+ ion beam with diameter ~5 nm and beam current of 1.1 pA. Patterning was conducted in such a way that a circular pattern is generated after the patterning. Inner red circle, as shown in Fig. 4.7, marks the pristine region whereas outer blue circle marks the bombarded region.

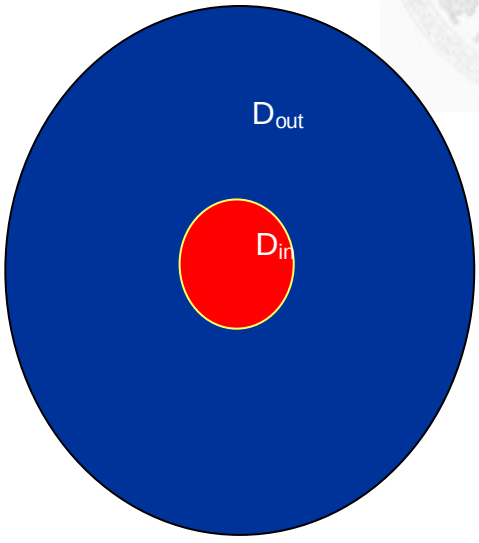

Figure 4.7: Pattern to irradiate the AAO nanochannels with FIB. Blue area is bombarded with Ga^+ ion beam and red area is left untouched. D_{in} = diameter of inner circle and D_{out} = diameter of outer circle.

4.2.3 Electrochemical growth of Ag in AAO

After thinning down the AAO wall to about 10-20 nm thickness, Ag can be electrodeposited in AAO nanochannels. Ag electrodeposition is conducted in a solution of $MgSO_4$ (20.5 gm) + $AgNO_3$ (0.5 gm) + H_2SO_4 (0.9 ml) + H_2O (500 ml) using pulsed - alternating current (60 Hz) at 9 V. This method of electrodeposition yields growth of polycrystalline Ag nanoparticles in AAO nanochannels.

4.3 Results and discussion

4.3.1 AAO nanochannels

Fig. 4.8 shows the top view of the AAO nanochannels after two-step anodization at 12 V (left hand side (LHS) image) and 20 V (right hand side (RHS) image) and pore widening in phosphoric acid to obtain w/d = 0.7. AAO formed at 20 V shows better self-organization and long range ordering of AAO nanochannels because best self-organization condition for anodization in sulfuric acid is at 25 V.

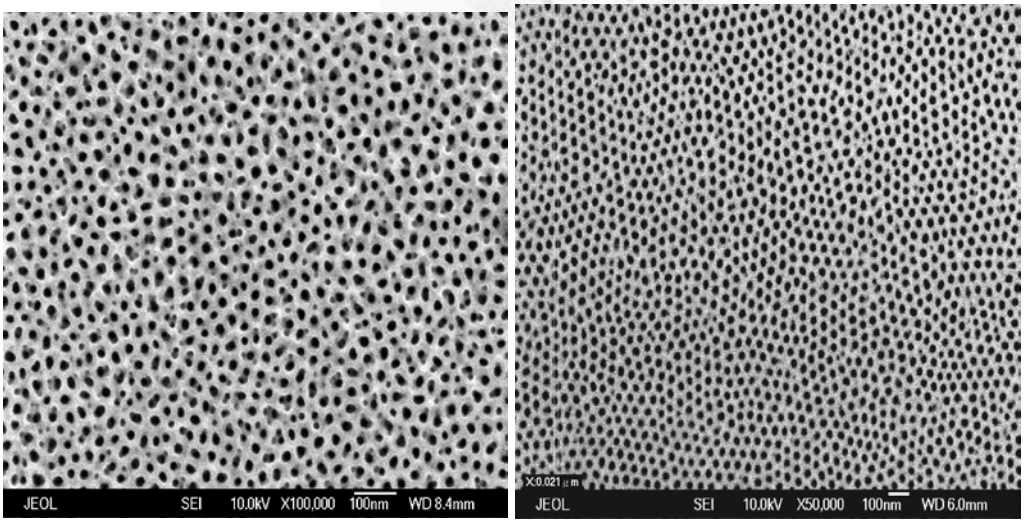

Figure 4.8 SEM images of AAO formed after anodizing in sulfuric acid at 12 V (left) and 20 V (right) and pore widening in phosphoric acid.

4.3.2 Selective closing of AAO nanochannels

Fig. 4.9 shows the formation of open single, double and triple AAO nanochannels surrounded by closed AAO nanochannels. Central hole(s) (black dot) represents open nanochannel(s) whereas surrounding white area marks the closed AAO nanochannels. Pore size of these open nanochannels is about 20-30 nm. Outside the patterned region there are self-organized AAO nanochannels. For AAO templates formed by anodization at 12 V and 20 V, and with w/d = 0.7, this type of open single, double and triple AAO nanochannels can be realized. Although AAO nanochannels can be closed with high beam current, use of small beam current (1 pA) is a must to realize such small open nanochannels pattern. Otherwise FIB beam tail will smear up the inner pristine (red circle in Fig. 4.7) region and all patterned regions will only have closed AAO nanochannels. Here, the thickness of the formed capping layer is about 30-35 nm. Therefore, after patterning the AAO templates further pore widening can be conducted to tune the wall thickness between the doublet and triplet of open AAO nanochannels. In this way the gap between the dimer of Ag nanoparticles can be tuned from 1 to 10 nm.

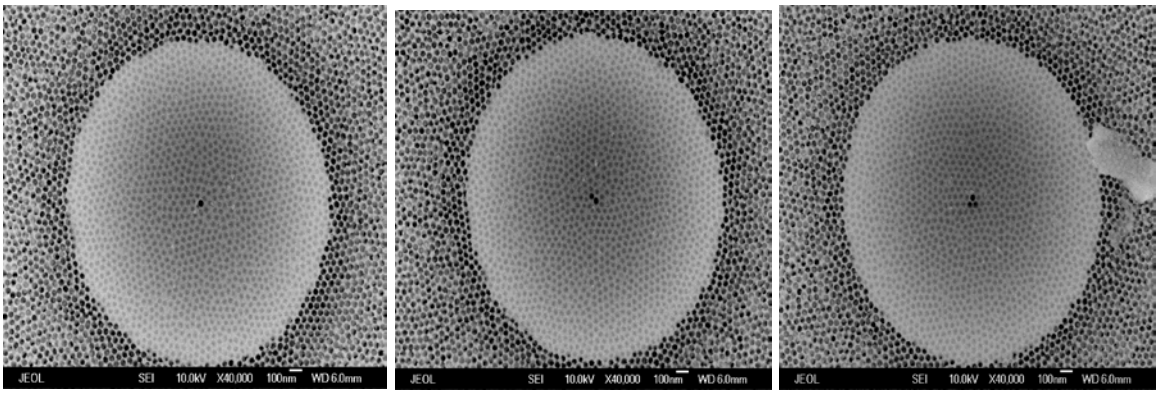

Figure 4.9: SEM images of open single, double and triple AAO nanochannels. FIB patterning was conducted by using a 30 KeV Ga^+ ion beam with 1 pA beam current and by delivering a dose of 10E16 ions/cm^2 to the patterned area. D_{in} = 100 nm.

4.3.3 Singlet, doublet, and triplet of Ag nanoparticles in AAO

Pulsed-alternating current deposition fills up the AAO nanochannels with Ag at a rate of 20-30 nm per second. Fig. 4.10 shows the optical image of the Ag/AAO template after patterning AAO and electrodepositing Ag. White regions mark the presence of capping layer on the FIB patterned area in whose center lies Ag nanoparticles singlet, doublet, and triplet in AAO. Presence of capping layer prohibits the electrodeposition of Ag in FIB patterned regions which results in formation of isolated Ag nanoparticle pairs.

Figure 4.10: Optical micrograph of Ag/AAO template after patterning AAO and electrodepositing Ag.

Fig. 4.11 shows the SEM image of the one of the white patterns shown in Fig. 4.10. Each of the six circles contains isolated Ag nanoparticle(s) in the center.

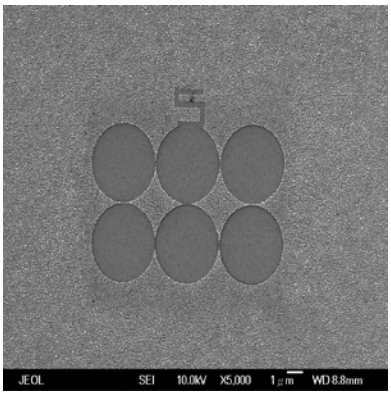

Figure 4.11 Low magnification SEM image of Ag nanoparticle(s) in AAO.

Fig. 4.12 shows the zoom in SEM images of the singlet, doublet, and triplet of Ag nanoparticles in AAO. These images clearly show the formation of the Ag nanoparticle dimmers with sub-10 nm gap. Size of the formed Ag nanoparticles is about 20-30 nm.

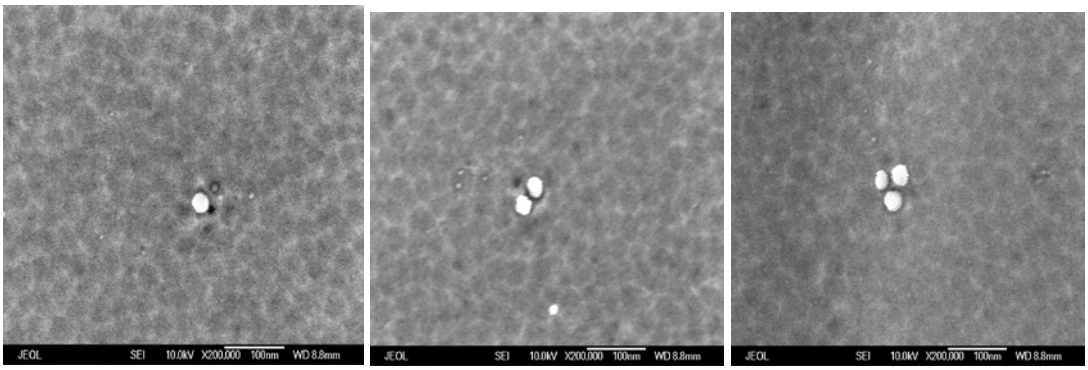

Figure 4.12: SEM images of the singlet, doublet, and triplet of Ag nanoparticles in AAO Magnification is 200 KX and scale bar is 100 nm. Size of Ag nanoparticles is about 20-30 nm.

4.3.4 Effect of ion beam dose on Ag electrodeposition

In order to understand the effect of the ion beam dose on the Ag electrodeposition, we patterned different patterns onto AAO template with varying dose and D_{in} (diameter of the pristine area inside the patterned circle). After patterning with different doses we do pore widening to get AAO wall thickness about 5 nm followed by ac-pulsed electrodeposition of Ag. Fig. 4.13 shows that for ion beam dose = 2E15 ions/cm^2, the capping layer starts to be form but it gets etched in pore widening step leading to Ag deposition everywhere. Increasing the ion beam dose to 1E16 ions/cm^2, the capping layer of thickness ≈ 20-30 nm is formed, which is able to sustain pore widening step and hence prohibits Ag deposition in patterned region. For dose greater than 1E16 ions/cm^2, AAO starts to get depleted which again leading to Ag deposition. It is to be noted that vertical

length of AAO under investigation is only about 50 nm. Therefore, it is necessary to carefully tune the ion beam dose for successful fabrication of isolated Ag nanoparticle(s) in AAO. In addition it is also required to use low beam current (1 pA) for patterning the AAO substrates.

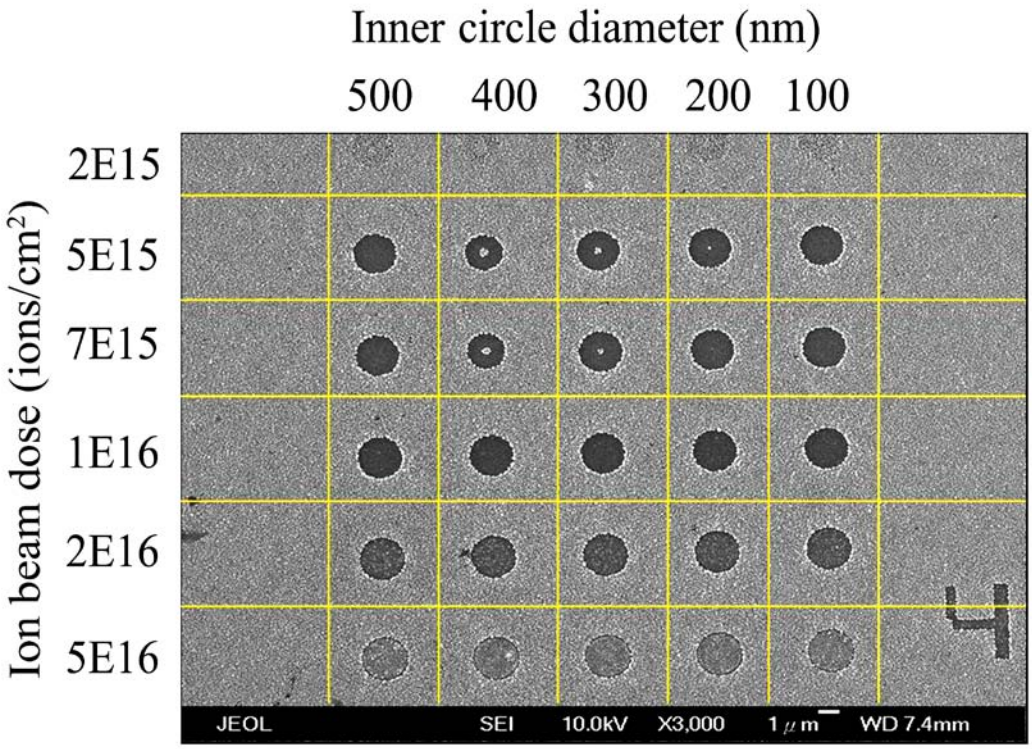

Figure 4.13: Effect of ion beam dose and Ag electrodeposition.

Finally it is to be noted that using the same D_{in} = 100 nm (Fig. 4.7) for AAO patterning, it is possible to fabricate single, double and triplet Ag nanoparticles in AAO. FIB patterning (closing) of AAO nanochannels is a statistical process. Probability of leaving behind a single, double and triple AAO nanochannel(s) open after patterning is about 20%, 40% and 30% respectively. Therefore, before undertaking any optical studies, SEM imaging is necessary to confirm the assembly of Ag nanoparticles in the region of interest (inside the FIB patterned area).

Chapter 5 Directional etching of silicon by silver nanostructures

5.1 Aim

Fundamentals of noble metal (Au, Ag, Pt) assisted electroless etching of Si have been discussed in section 1.5 of chapter 1 of this thesis. Briefly, metal assisted electroless etching (chemical etching, no bias applied) of Si is defined as etching of Si in an aqueous solution of HF and metal salts. It can also be conducted in an aqueous solution of HF and an oxidizing agent, such as H_2O_2, after deposition of noble metal thin films or nanoparticles (NPs) or lithographic patterns onto Si.

Directional etching of Si(100) substrates by Ag nanoparticles and Ag meshes has been reported by different groups [58, 61-64]. However, directional etching of Si by isolated Ag nanorods and nanorings has not been achieved. Further more, it has been observed that etching proceeds by reduction of H_2O_2 on a Ag surface accompanied by oxidation of Si and followed by etching of the oxidized Si by HF [58, 64]. The etching of formed silicon oxide by HF is isotropic, which implies that Ag/Si interface oxide is a key factor which governs the directionality of Si etching. However, the role of interface oxide remains unknown. We performed the directional etching of the Si(100) substrates by Ag nanoparticles, Ag nanorods, and Ag nanorings. After the etching of a Ag/Si sample, the oxide at Ag/Si interface is examined using high resolution transmission electron microscopy (HRTEM). The Effect of Ag/Si interface oxide on the directional etching is studied by etching of $Ag/SiO_x/Si$ samples of known interface oxide thickness. A

mechanism based on Ag-Si interaction has been proposed to explain the directional etching of Si by Ag.

5.2 Experiments

5.2.1 Electron beam lithography of Ag nanopatterns on Si

Ag nanoparticles, nanorods, and nanorings, Ag nanopatterns are fabricated on the Si(100) substrates using scanning electron microscopy (SEM)-based electron beam lithography (EBL). First, poly-methyl-methacrylate (PMMA) A4 is spin coated on a clean and dry H-Si substrate to achieve a PMMA thickness of 200 nm. After baking the coated Si substrate at 180ºC for 3 min, it is loaded into the SEM- based EBL system for writing the desired patterns onto PMMA. Then, an electron beam patterned PMMA/Si sample is developed in the 3:1 (v/v) solution of methyl-isobutyl-ketone (MIBK) and iso-propyl-alcohol (IPA) for 1 min, followed by rinsing in IPA for 30 s, rinsing in de-ionized water for 5 s, and blow drying using dry nitrogen gas. Any residual PMMA and Si native oxide on the sample are removed by 5 s carbon-tetra fluoride (CF_4) reactive ion etching (RIE) at 50 W power and 20 mTorr pressure. It is to be noted that CF_4 RIE etches the surface silicon oxide quickly, but upon prolonged exposure to Si surface, a fluorocarbon layer is formed on the Si surface. Therefore, sometimes, a follow up cleaning by Argon (Ar) RIE at 50 W power and 20 mTorr pressure for 5 sec may be used to ensure that there is no fluorocarbon layer on the Si surface. O_2 RIE should be avoided to prevent the partial oxidation of the Si surface. Then, the cleaned sample is immediately loaded into an oil-free thermal evaporator for deposition of a 50 nm Ag thin film. Afterwards, a lift-off process is conducted in Remover PG (Micro-Chem) to obtain the desired Ag nanopatterns on Si.

5.2.2 Etching of Si by Ag nanopatterns

After patterning the Si substrates with Ag nanopatterns, the samples are etched in an aqueous solution of 4.8 M HF and 0.3 M H_2O_2. After etching the samples are rinsed in deionized water and blow dried using dry N_2 gas. SEM characterization is performed to record the morphologies of all the Ag nanopatterns on Si and the etched Si substrates. 1 pA Ga^+ Focused Ion Beam (FIB) operating at 30 KV FIB is used to prepare cross sections of the etched nanostructures and cross sections are recorded using SEM.

5.2.3 Post etching investigation of Ag/Si interface

To understand the directional etching of Si, the Ag/Si interface is examined by HRTEM after the etching of Ag (5nm thickness)/Si substrates in the aqueous solution of 4.8 M HF and 0.3 M H_2O_2. The Ag (5nm thickness)/Si sample is chosen for ease of characterization. Ag film deposition is conducted by radio frequency magnetron sputtering of a Ag target (99.99% purity) under an Ar gas pressure of 2 mTorr. In order to record the Ag/Si interface with a minimal effect from air oxidation, the etched Si substrates are dried up quickly and covered with commercial G1 glue. Thereafter, the G1 glue is cured at 180ºC for 3 min to cross link the epoxy to terminate the Si oxidation process [138]. It is known that the Si oxidation rate≈(2 -5 Å in about 5 h) is very low [139] at standard temperature and pressure (S.T.P.) and quick coverage with the G1 glue also terminates this process. Cross-sectional HRTEM samples are prepared quickly to limit the oxidation of Si during the sample preparation followed by loading of samples into the microscope. TEM-energy dispersive X-ray (EDX) spectra are used to quantify the amount of SiO_x present at the Ag/Si interface after the etching of Si by Ag.

5.2.4 Etching of Ag/SiO_x/Si substrates with varying oxide thickness

To understand the effect of Ag/Si interface oxide on the directional etching of Si, the Ag thin film deposited Si samples with various Ag/Si interface oxide thicknesses are etched in the aqueous solution of 4.8 M HF and 0.3 M H_2O_2. First, clean hydrogen terminated Si substrates are prepared. Then, on one substrate, the Ag thin film (thickness ≈ 5nm) is sputter deposited. Immediately after deposition, it is etched in the etching solution. Other cleaned Si substrates are oxidized in a humid-pure oxygen environment to achieve 5-7- and 10-12-Å-thick silicon oxides [139]. After depositing Ag films, the samples are immediately etched in the aqueous etching solution (4.8 M HF and 0.3 M H_2O_2). Morphologies of the Ag films deposited on SiO_x(2-3Å)/Si, SiO_x(5-7Å)/Si, and SiO_x(10-12Å)/Si and etched Si were recorded using SEM.

5.3 Results and discussion

5.3.1 Directional etching of nanoholes and nanotrenches into Si

Figures 5.1(a), 5.1(d), and 5.1(g) show the SEM images of the Ag nanoparticles, nanorods, and nanorings on the Si substrate respectively, whereas Figs. 5.1(b), 5.1(e), and 5.1(h) show the plan view SEM images of the corresponding etched nanostructures. Respective cross-sectional SEM images of the etched nanostructures in Figs. 5.1(c), 5.1(f), and 5.1(i) elucidate the etching of straight nanostructures into Si the along [100] direction. Cross-sections of the etched nanostructures are cut using 1 pA Ga^+ focused ion beam (FIB) operating at 30 KeV for minimizing the redeposition of sputtered material. We observe partial closure/covering of the etched nanostructures by the ion beam

sputtered Si. It implies that top most Si surface and vicinity of the etched nanostructures have micro-porous Si structure as suggested by Chourou et. al. [140].

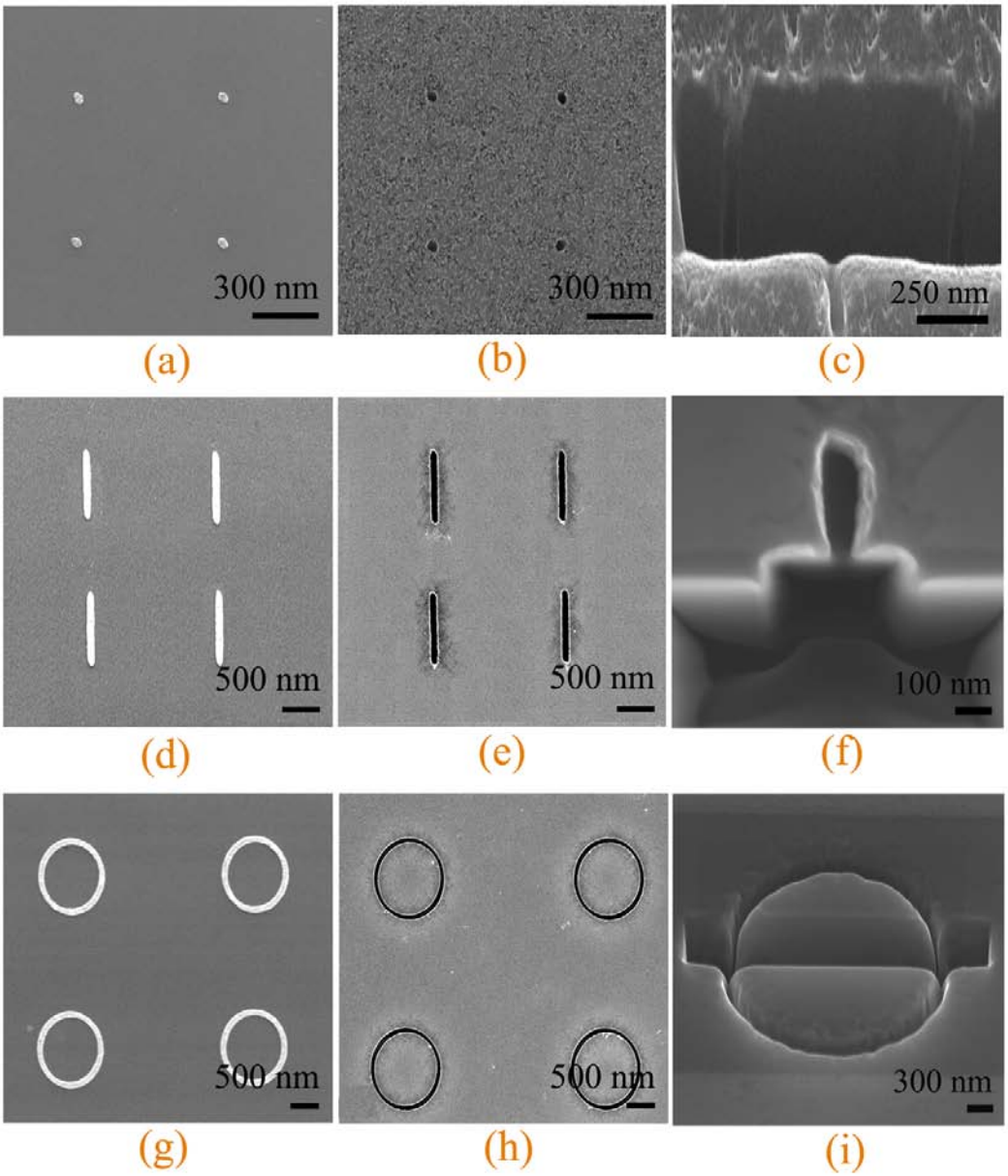

Figure 5.1: SEM images of Ag nanopatterns on Si: (a) Ag nanoparticles, (d) Ag nanorods, and (g) Ag nanorings. SEM images of the corresponding etched Si nanostructures formed after etching Ag nanopattern/Si in aqueous solutions of 4.8 M HF and 0.3 M H_2O_2 for 10 min: (b)-(c), (e)-(f), and (h)-(i).

5.3.2 Quantification of oxide at Ag/Si interface

Etching of the Ag/Si sample results in the formation of straight nanochannels along the Si [100] direction as shown in Fig. 5.2(a). Figure 5.2(b) shows the cross-sectional TEM image of a Ag NP at the bottom of a Si nanochannel. Here, the region marked '1' is the location of a thinner Ag/Si interface oxide and that marked '2' is the location of a thicker Ag/Si interface oxide. Figure 5.2(c) shows the cross- sectional HRTEM image of the very thin SiO_x at the Ag/Si interface (within the regions enclosed by white circles). TEM-EDX spectra from the regions marked '1' and '2' in Fig. 5.2(b) are shown in Fig. 5.2(d) which reveals that the silicon to oxygen ratio is about 3-4 times higher in the region marked "1". We conducted investigation of 10 Ag NPs which are randomly selected from different etched Si samples and all Ag NPs show similar type of etching interfaces. These results imply that at any given time, two types of locations are present during the etching process. At type-a locations [e.g, the region marked '1' in Fig. 5.2(b)], Ag NPs remain in contact with Si, whereas at type-b locations [e.g, the region marked '2' in Fig. 5.2(b)], oxidation of Si and etching of the formed oxide continue. TEM sample preparation may result in formation of additional SiO_x at Ag/Si interface. Therefore, we are considering only relative amount of SiO_x at different types of Ag/Si interfaces. Maintenance of the Ag-Si nano-scale contacts or very thin SiO_x mediated Ag-Si interaction results in the charge neutrality of Ag NPs which in turn ensures that Ag NPs are not etched during the etching process. Otherwise, if Ag NPs are not in contact with Si or Ag-Si interaction is too weak, Ag NPs will be oxidized by H_2O_2 and etched away by HF.

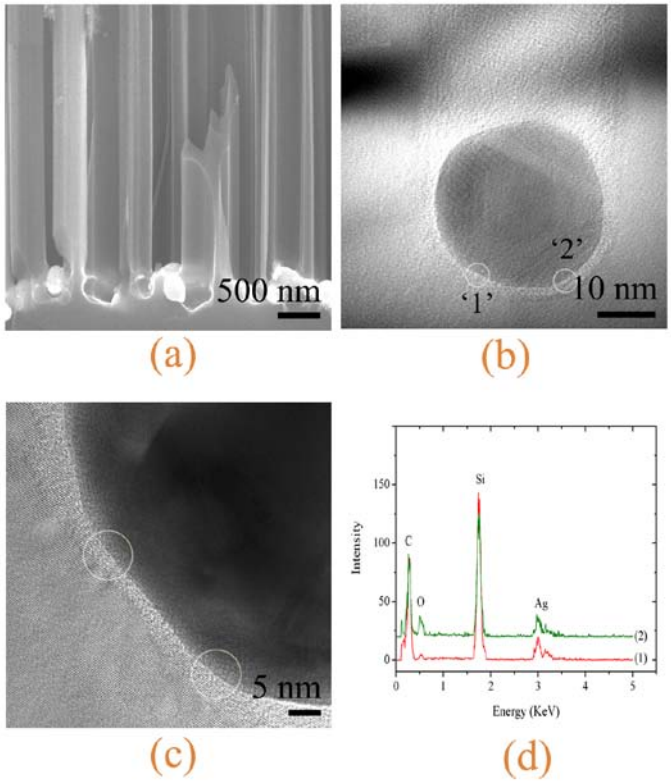

Figure 5.2 Cross-sectional SEM image of Si nanochannels formed after etching of Ag (5 nm film)/Si in aqueous solutions of 4.8 M HF and 0.3 M H_2O_2 for 10 min. (b) HRTEM image of a single Ag nanoparticle at bottom of etched Si nanochannel. (c) Zoom-in HRTEM image showing a thin nano-scale Ag/Si interface within the regions enclosed by white circles. (d) TEM-EDX spectra recorded from locations marked "1" and "2" in image (b).

5.3.3 Effect of Ag/Si interface oxide thickness

Fig. 5.3 shows that sputter deposition of Ag on SiO_x(2-3Å)/Si, SiO_x(5-7 Å)/Si, and SiO_x(10-12 Å)/Si substrates results in deposition of the Ag film with similar type of morphologies (continuity and roughness). Moreover, the Ag particle size and surface density of particles are not altered significantly. It implies that etching behavior of these

Ag deposited SiO_x/Si samples should not be directly associated with Ag film morphologies.

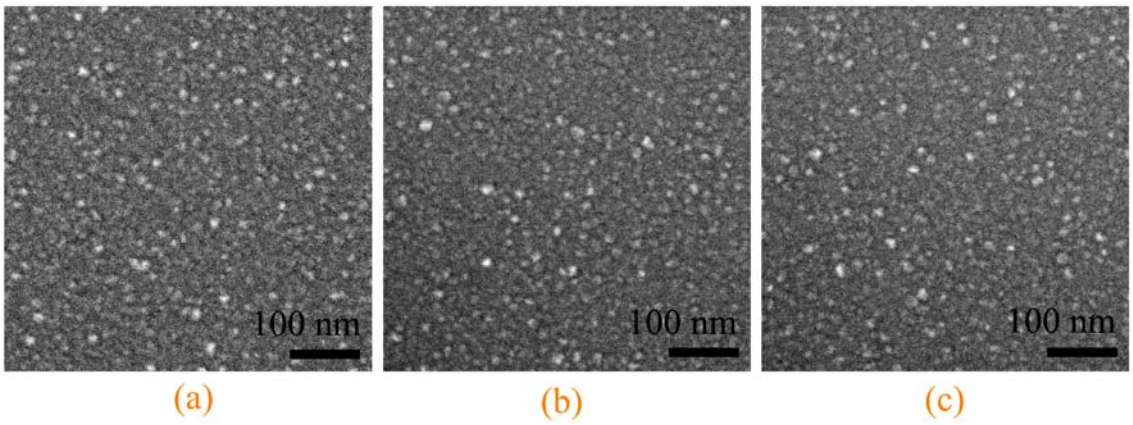

Figure 5.3: SEM images of the Ag thin films (thickness ≈ 5 nm) sputter deposited on (a) SiO_x(2-3Å)/Si, (b) SiO_x(5-7 Å)/Si, and (c) SiO_x(10-12 Å)/Si substrates.

After etching of Ag/SiO_x(2-3Å)/Si and Ag/SiO_x(5-7Å)/Si samples, the formation of directional nanochannels by the Ag nanoparticles into Si is observed [Figs. 5.4(a)-5.4(d)], whereas etching of Ag/SiO_x(10-12 Å)/Si results in the formation of micro-porous Si on top accompanied by reduction in the number density of straight channels as shown in Figs. 5.4(e) and 5.4(f). Therefore, when the interface oxide thickness is about 1 nm, Ag nanoparticles trace random trajectories in the beginning of the etching process. Once the Ag/Si interface acquires equilibrium interface oxide thickness ≈(5Å), they start to perform the directional etching of nanochannels into Si. Results in Fig. 5.4(e) and 5.4(f) may also be explained by etching of many Ag NPs into solution because of negligible Ag-Si interaction and subsequent reduction in number density of nanochannels. We propose that in addition to the type of metal catalyst (Ag, Pt or Pd) [140], crystallinity and doping of the Si substrate [141], the shape of the metal pattern on Si and the

composition of the etching solution [142, 143], the maintenance of the sub-nanometer oxide at the Ag/Si interface is also a key factor in regulating the directional etching of Si.

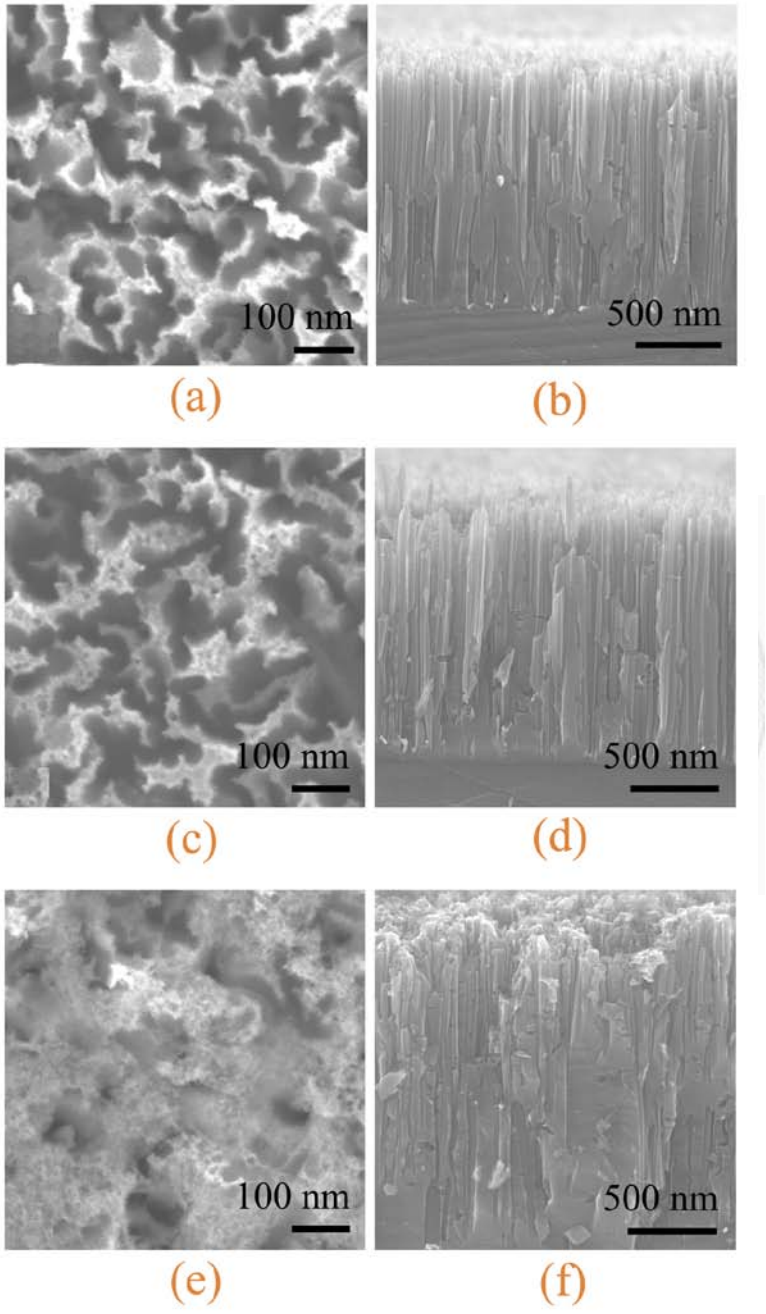

Figure 5.4: SEM images of etched Si after etching of Ag/SiO_x(2-3 Å)/Si [(a)-(b)], Ag/SiO_x(5-7 Å)/Si [(c)-(d)], and Ag/SiO_x(10-12 Å)/Si [(e)-(f)] substrates in aqueous solution of 4.8 M HF and 0.3 M H_2O_2.

5.3.4 Etching mechanism

It has been proposed that Ag assisted etching of Si proceeds by reduction of H_2O_2 (reaction '1') on a Ag NP surface and oxidation of Si (reaction '2') due to injected holes, followed by etching of the oxidized Si (reactions '3' and '4') by HF into H_2SiF_6 accompanied with evolution of SiF_4 and H_2 gases [57]. The following chemical reactions describe the etching process briefly.

(1) $H_2O_2 + 2H^+ + 2e^- \rightarrow 2H_2O$

(2) $Si + 2H_2O + 4h^+ \rightarrow SiO_2 + 4H^+$

(3) $SiO_2 + 6HF \rightarrow H_2SiF_6\,(aq) + 2H_2O$

(4) $SiO_2 + 4HF \rightarrow SiF_4\,(g) + 2H_2O\,(g)$

(5) $2H^+ + 2e^- \rightarrow H_2\,(g)$

Etching of the silicon oxide by HF is isotropic, which implies that reduction of H_2O_2 accompanied by oxidation of Si is the key factor which governs the directionality of Si etching. During the Ag assisted etching of Si in the aqueous HF + H_2O_2 solution, the surface of Si is mainly passivated either by -H bonds or by -OH or by -F bonds. Moreover, it is known that the charge transfer probability across the Si-OH bond is higher than that across the Si-H or Si-F bond [144]. Furthermore, the H-Si(100) or F-Si(100) surface is easy to oxidize in an aqueous or oxygen environment compared with Si(111) surface because it has a 4-5 times higher density of surface states [145]. Therefore, the injection of holes along Si [100] is favored which in turn promotes directional oxidation (refer to reaction '2') and etching of Si. This proposal is consistent with the HRTEM investigation of the Ag/Si interface after the etching. The HRTEM image shows that during etching some part of the Ag NPs is always in contact with Si.

This Ag-Si contact or interaction promotes directional oxidation followed by etching by HF. This Ag-Si interaction may also explain the sticking of Ag to Si during etching. Wei et. al. [146] calculated the adsorption energy of the Ag adatoms at a distance of one monolayer from the Si surface and found it to be about 2.4 eV. This adsorption energy would translate into an interaction force of about 10^{-9} N between the Ag adatom and the Si surface. During etching, if 1000 atoms of Ag are in contact with Si, the Ag-Si interaction force ($\approx 10^{-7}$ N) is sufficient for countering Brownian force ($F_B \approx K_BT$/size of the Ag nanopattern, where K_B is the Boltzman constant; $F_B \approx 10^{-14}$ N for 50 nm Ag nanoparticles), and the force generated by bursting of gas bubbles (pressure inside the nanometer air bubble ≈ 10 M Pa which is equivalent to force of 10^{-8} N). Nonetheless, if the Ag-Si interaction is weakened by excess interface oxide, the loss of directionality of etching will be observed as shown in Fig. 5.4.

Chapter 6 Electroless Ag plating on Silicon

6.1 Aim

As described in section 1.3 of chapter 1 of this thesis, Electroless metal plating is defined as deposition of metal films onto conducting (metal, alloys, and semiconductors) or insulating (polymer, glass, and ceramics etc.) substrates without using any external bias. Plating of noble metals on Si substrates finds application in interconnects and contact pads etc. in integrated circuit (IC) industry [48], metal nanostructures for surface enhanced Raman spectroscopy (SERS) substrates [49,50], plasmonics [51], catalysis [52], electromagnetic shielding [53], and bio-medical technologies [54], growth of Si nanowires [55], and energy storage and production [56]. Ag Plating on Si by galvanic displacement reaction can be conducted by immersing cleaned Si substrates in an aqueous solution of silver nitrate and HF. Owing to its scientific and technological applications; we investigated the mechanism of electroless plating of Ag on Si using high resolution electron microscopy and in-situ Raman and FTIR spectroscopy.

6.2 Experiments

6.2.1 Cleaning of Si substrates

p-type Si(100) substrates (resistivity (ρ) $\approx$ 10 Ωcm) were cleaned by immersing in Piranha solution (H_2SO_4:H_2O_2::4:1) for 5 minutes, rinsing in deionized water ($\rho \approx 18.2$ M Ω cm) for 5 minutes, immersing in 1% HF solution for 5 minutes, rinsing in water for 5 minutes and blow drying using nitrogen gas.

6.2.2 Electroless Ag Plating on Si

For Ag plating, the cleaned Si substrates are immersed in an aqueous solution of 2 M silver nitrate ($AgNO_3$) and 50 mM hydrofluoric acid (HF) for 5 seconds and 5 minutes. After plating samples are rinsed in DI water and alcohol and blow dried using dry N_2 gas.

6.2.3 Characterization

Morphologies of the deposited Ag nanoparticles (NPs) on Si are recorded using SEM. Crystallinity of Ag NPs, growth of Ag nanoparticles on Si and Ag/Si interfaces are investigated using HRTEM. AFM is used to record the time dependent evolution of morphologies of Ag NPs plated Si substrates.

The Raman measurements were performed on a commercial HR800, Jobin-Yvon Raman spectrometer using a 632.8 nm He-Ne laser light as the excitation source. Laser beam is focused with a 50× objective lens (0.5 NA, 10 mm WD) onto the sample resulting in an irradiation power density of 10^5 W/cm^2. The scattered radiation was collected backward with the same objective lens and then was sent through a Raman notch filter to an 80-cm monochromator. The dispersed spectrum was detected by a liquid nitrogen-cooled charge-coupled device camera. The Raman spectrometer has a spectral resolution of < 7 cm^{-1} and a Raman-shift error of < 0.1 cm^{-1} as determined by a calibration procedure. Data accumulation time of each spectrum was 1 min. During the *in-situ* Raman measurements, the Si samples were placed inside a Teflon container and immersed in the Ag plating solution. A low-fluorescence glass plate (150 μm thickness) is used to cover the container and prevent the evaporated gases of the plating solution from corroding the objective lens. Surface of the plating solution was 2 mm above the

sample surface and 3 mm below the protecting glass plate. The Raman spectra of the plated Si substrates after rinsing in H_2O and blown drying with N_2 gas, and the plating solution were also recorded for comparison.

Infrared absorption spectra were acquired in transmission mode using a commercial Nicolet Magna II 550 Fourier-transform infrared (FTIR) spectrometer with a spectral resolution of < 0.1 cm^{-1}. Ag NPs plating occurs on both front and back surfaces of the Si substrates. After plating for 5 min, the Si substrates were removed from the plating solution and immediately mounted on the sample stage of the FTIR spectrometer. We recorded *in-situ* FTIR spectra with data accumulation time of 10 sec for each spectrum. The plating solution was observable to naked eyes on both surfaces of these samples even after recording of the *in-situ* FTIR spectra and there was no observable evolution in the *in-situ* FTIR spectra during measurements. Therefore, it is expected that the Ag plating reaction should continue for several seconds even after removal of the substrates from the plating solution.

The plated samples were subsequently rinsed in H_2O and blown dried with N_2 gas. Another FTIR measurement was taken on such samples afterwards. An FTIR spectrum of a cleaned Si substrate (without 2-3 nm of native oxide) was recorded for reference.

6.3 Results and Discussion

6.3.1 Morphologies of plated Ag NPs

Immersion of Si substrates into Ag plating solution results in the growth of crystalline Ag NPs onto the Si surface as shown in Fig. 6.1. These particles have sizes ranging from 20-50 nm as seen in SEM image of Fig. 6.1(a). Crystallinity of the Ag NPs

has been elucidated by cross sectional TEM image (Fig. 6.1(b)) and high resolution TEM image of a Ag NP/Si interface (Fig. 6.1(c)).

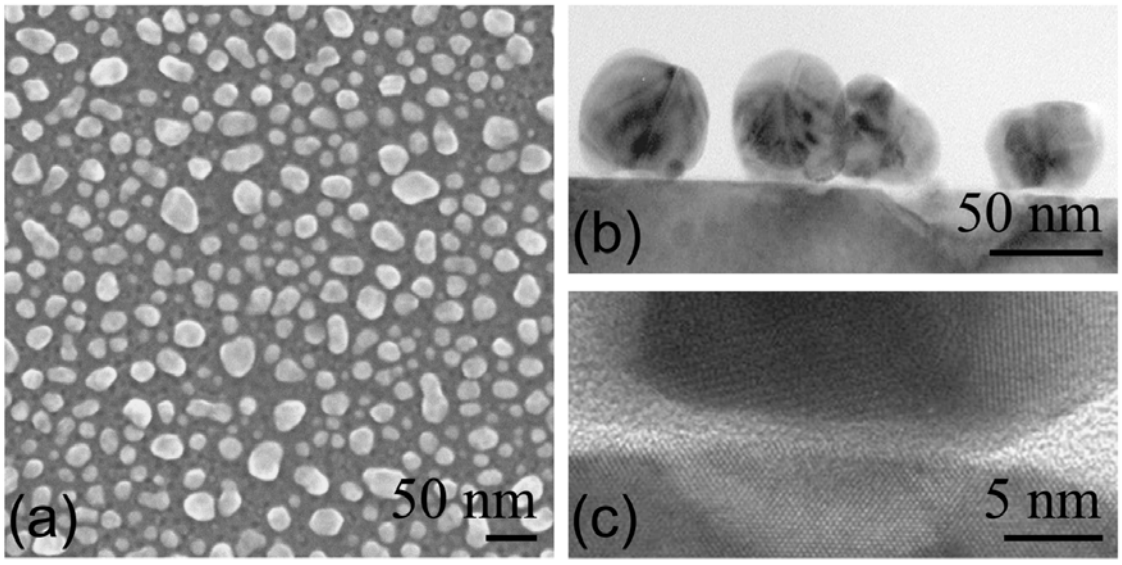

Figure 6.1: (a) Plan view SEM image of Ag nanoparticles (NPs) on Si(100) formed by electroless plating in 2 M $AgNO_3$ + 50 mM HF for 5 minutes. (b) Cross sectional TEM image of Ag NPs on Si (c) HRTEM image of a Ag NP/Si interface.

In order to understand the time evolution dependent morphologies of Ag NPs, we conducted AFM, SEM and TEM investigations. Fig. 6.2 shows the plan view (top) and 3 D (bottom) morphologies of the Si substrates after plating with Ag NPs for 5 s. And Fig. 6.3 shows the plan view (top) and 3 D (bottom) morphologies of the Si substrates after plating with Ag NPs for 5 min. As determined by AFM images, with the increase of time from 5 s to 5 min, root mean square (RMS) roughness of the Ag NPs plated Si substrates increases from 2.15 nm to 8.25 nm. Presence of finer white spots on AFM images imply slow and step by step growth of Ag nano-islands onto Si substrates.

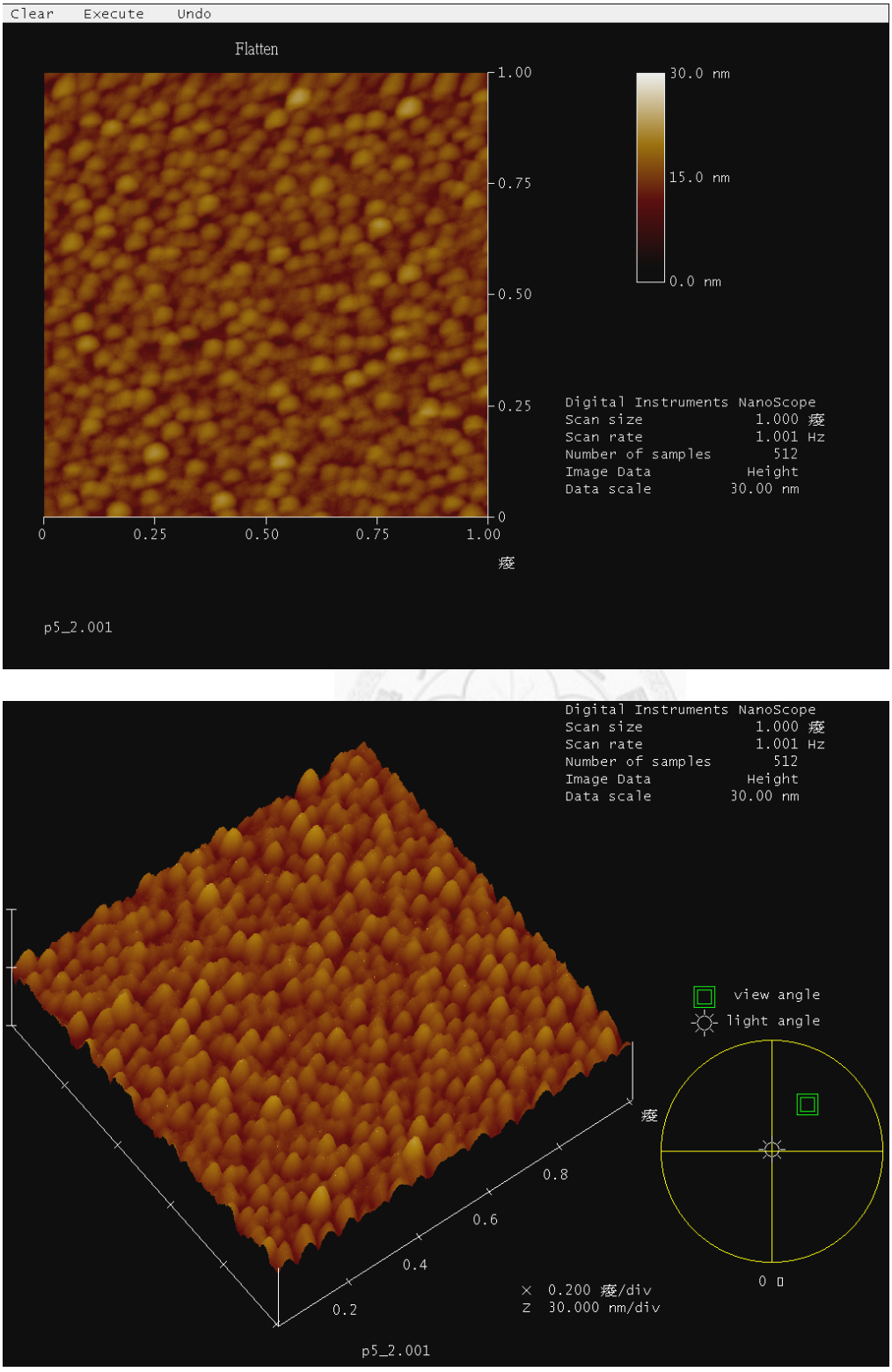

Figure 6.2: Plan view (top) and 3 D (bottom) morphologies of the Si substrates after plating with Ag NPs for 5 s.

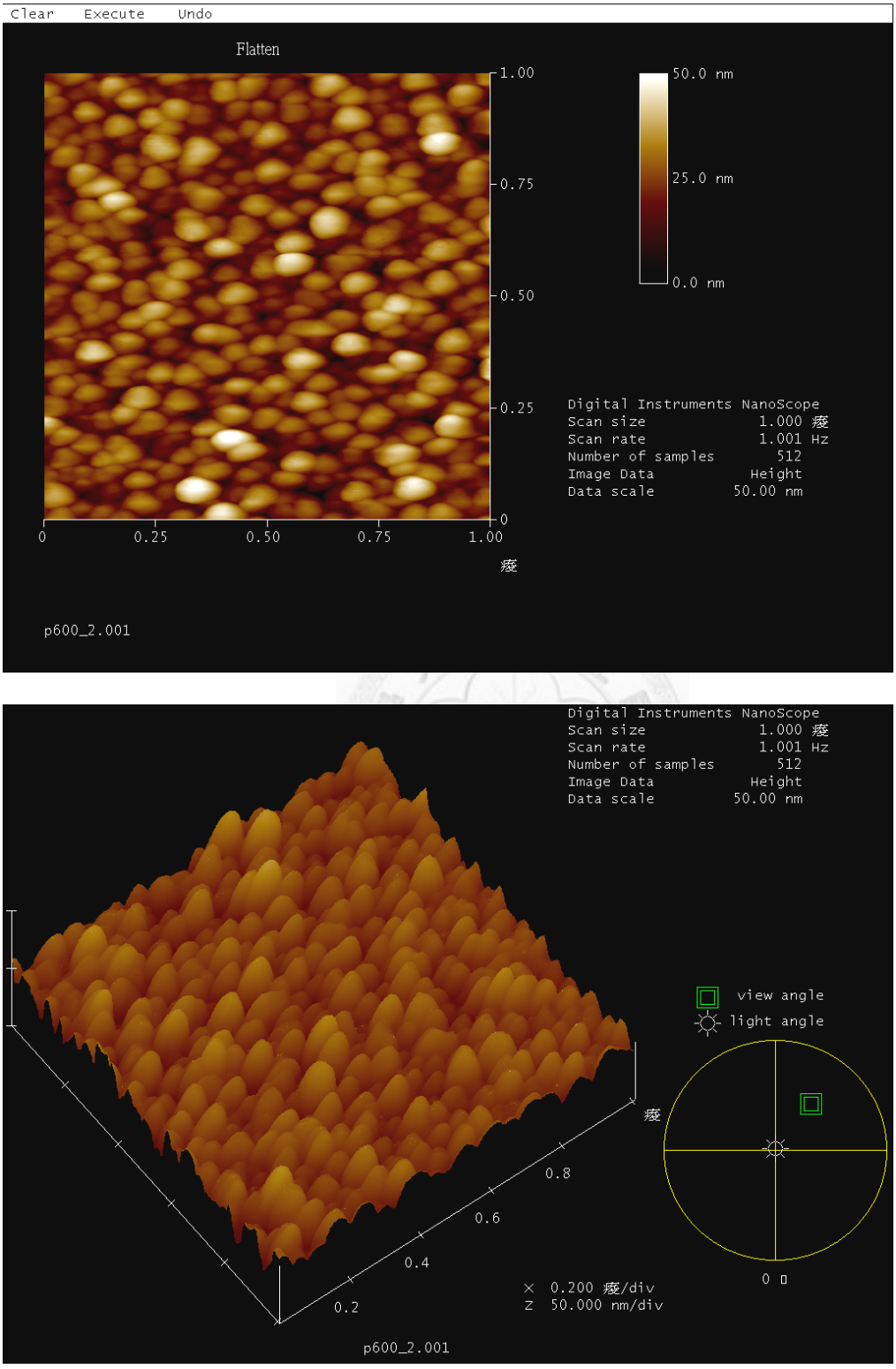

Figure 6.3: Plan view (top) and 3 D (bottom) morphologies of the Si substrates after plating with Ag NPs for 5 min.

Fig. 6.4(a) shows SEM image of the nucleation process of Ag NPs on Si after 5 seconds of plating. Ag NPs with sizes ranging from 5 to 20 nm are observed. Cross sectional TEM and HRTEM images (Fig. 6.4(c), (e)) show Si surface corrugations (～5 nm) which are conformal to geometry of Ag NPs. These corrugations indicate that growth of Ag NPs proceeds by nanoscale displacement or etching of Si from the regions below and near the nucleation centers of Ag NPs. Formation of very small Ag NPs during the nucleation process implies the Volmer-Weber (island formation) type growth of Ag NPs on Si. Upon increasing the plating time to 5 minutes, Ag NPs with sizes ranging from 10 to 35 nm are observed as shown in SEM image of Fig. 6.4(b). Comparing Fig. 6.4(a) and (b), it is observed that the growth rate of smaller particles is smaller compared to bigger particles. This can be understood in terms of change of metal-Si Schottky barrier height (energy difference between valence band maxima of p-type Si and Fermi level of metal or energy difference between conduction band minima of n-type Si and Fermi level of metal). It has been reported that metal (Ni)-semiconductor (Si) barrier height increases when size of Ni-Si contacts is reduced from 1530 nm to 174 nm [149]. And in our case, smaller Ag NPs (5-20 nm) have even smaller nanoscale metal-Si contacts. This will lead to presence of higher Ag-Si Schottky barrier height for smaller Ag NPs. Growth of Ag NPs on Si requires that the Ag^{+} ions from the plating solution must get reduced at Ag/Si interface by taking electrons from Si. Higher Ag-Si Schottky barrier height for smaller Ag NPs reduces the charge transfer probability across Ag/Si interface leading to slower growth rate of smaller Ag NPs. With the increase of plating time the Si surface corrugations also show 2 to 4 times increment as seen in the cross sectional TEM images (c) and (d) of Fig. 6.4.

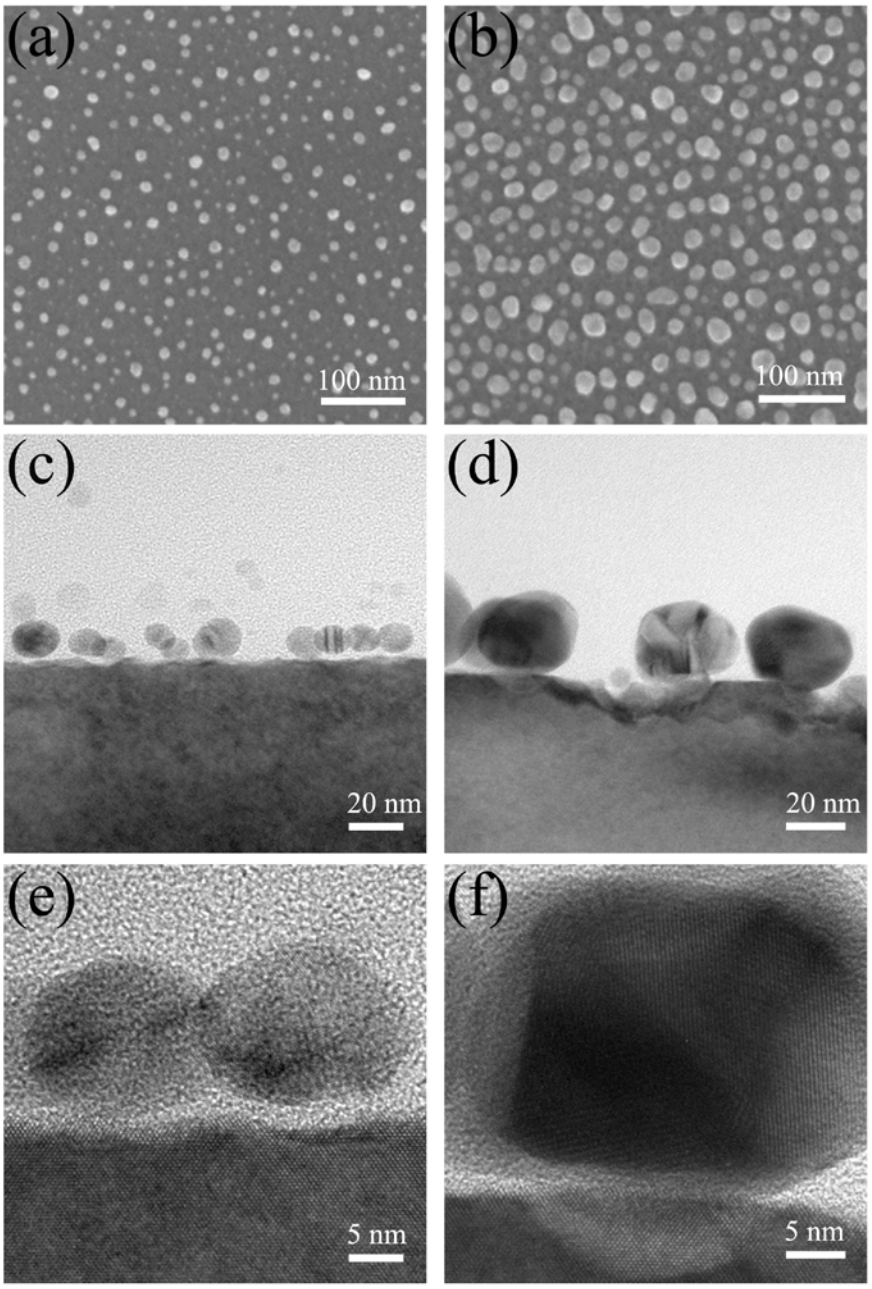

Figure 6.4: Electron microscope images showing growth of Ag nanoparticles on Si after plating in an aqueous solution of 2 M silver nitrate ($AgNO_3$) and 50 mM HF. (a), and (b): Plan view SEM images of Ag NPs on Si after plating for 5 seconds and 5 minutes respectively. (c), and (d): Corresponding cross-sectional TEM images of Ag NPs. (e), and (f): Corresponding cross-sectional HRTEM images of Ag NPs.

This is consistent with the fact that growth of Ag NPs on Si substrate occurs by galvanic displacement of Si. Cross sectional HRTEM image as shown in Fig. 6.4(f) elucidates the nanocrystalline structure of the Ag NPs on Si substrate. Crystallinity of these NPs makes them a better catalyst for vapor-liquid-solid (VLS) growth of highly crystalline Si nanowires as compared to particles grown on Si by physical evaporation of metal [150].

6.3.2 Raman spectra

Fig.6.5 shows the Raman spectra of Si substrates after plating them with Ag NPs for 5 seconds (Fig. 6.5(a)) and 5 minutes (Fig. 6.5(b)) respectively. Fig. 6.5(c) shows the *in-situ* Raman spectra of the Ag plating solution and Fig. 6.5(d) shows the spectra of the used plating solution after continued Ag plating for 2 hours. A weak shoulder around 230 cm^{-1}, peaks at 302 cm^{-1} (2 transverse acoustic mode), 520 cm^{-1} (transverse optical (TO) mode), 620 cm^{-1} (2 longitudinal acoustic mode) and 940 cm^{-1} (2 TO phonon overtone mode at point W in Brillouin zone) are assigned to Si [151]. Interestingly, Fig. 6.5(b) shows an additional broad peak at 965 cm^{-1} (2 TO phonon overtone mode at point L in Brillouin zone), which could be the result of surface enhanced scattering of this particular mode of 2TO bands of Si with light due to presence of Ag. It is to be noted that 2 TO phonon band centered at 960 cm-1 is associated with vibration modes at 920 cm^{-1} (2 TO-phonon overtone scattering from critical point X in Brillouin Zone), 940 cm^{-1} (2 TO-phonon overtone at point W), 965 cm^{-1}(2 TO-phonon overtone scattering from point L) and termination of phonon scattering at 1040 cm^{-1} due to rapid decrease in density of states at this point in Brillouin zone [152]. A medium intensity peak at 654 cm^{-1} is assigned to the peak of silicon-hexafluoride ion (SiF_6^{2-}) in the Raman spectra of H_2SiF_6 in

water [153]. This peak is not observable in the in-situ Raman spectra due to low concentration of SiF_6^{2-} in the solution. A broad peak at 480 cm^{-1} is likely to originate from hydrogenated amorphous silicon or similar disorder due to HF electrochemical etching [154].

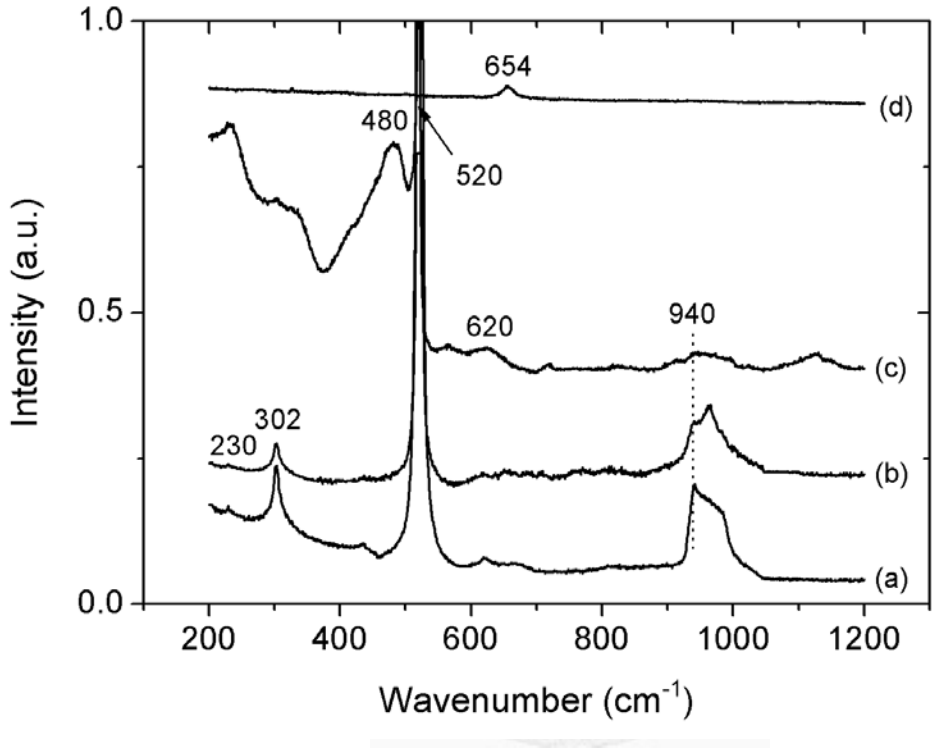

Figure 6.5: Raman spectra of Ag NPs plated Si after: (a) 5 s of Ag plating, and (b) 5 min of Ag plating. (c) *In-situ* Raman spectra of the Ag plating process in solution of 2 M $AgNO_3$ and 50 mM HF. (d) Raman spectra of the used plating solution after 2 hours of Ag plating. Peaks at 230 cm^{-1}, 302 cm^{-1} (2 transverse acoustic mode), 520 cm^{-1} (transverse optical (TO) mode), 620 cm^{-1} (2 longitudinal acoustic modes) and 940 cm^{-1} (2 TO mode) are assigned to Si. Peak at 654 cm^{-1} is assigned to silicon-hexafluoride ion (SiF_6^{2-}). All the spectra are recorded using 632.8 nm He-Ne laser light perating at 10 mW power, and have been normalized to unity, and shifted along y-axis for clear presentation.

6.3.3 FTIR spectra

Fig. 6.6(a) shows *in-situ* FTIR spectra of Ag plating onto Si substrates whereas Fig. 6.6(b) shows FTIR spectra of the Ag NPs plated Si substrate after rinsing in deionized water and drying with dry N_2 gas. Fig. 6.6(c) shows FTIR spectra of a cleaned Si substrate with 2-3 nm of native oxide. For recording the spectra (c), a Si sample was cleaned by sonication in acetone, methanol and deionized water (18.2 MΩ·cm resistivity) for 5 minutes separately.

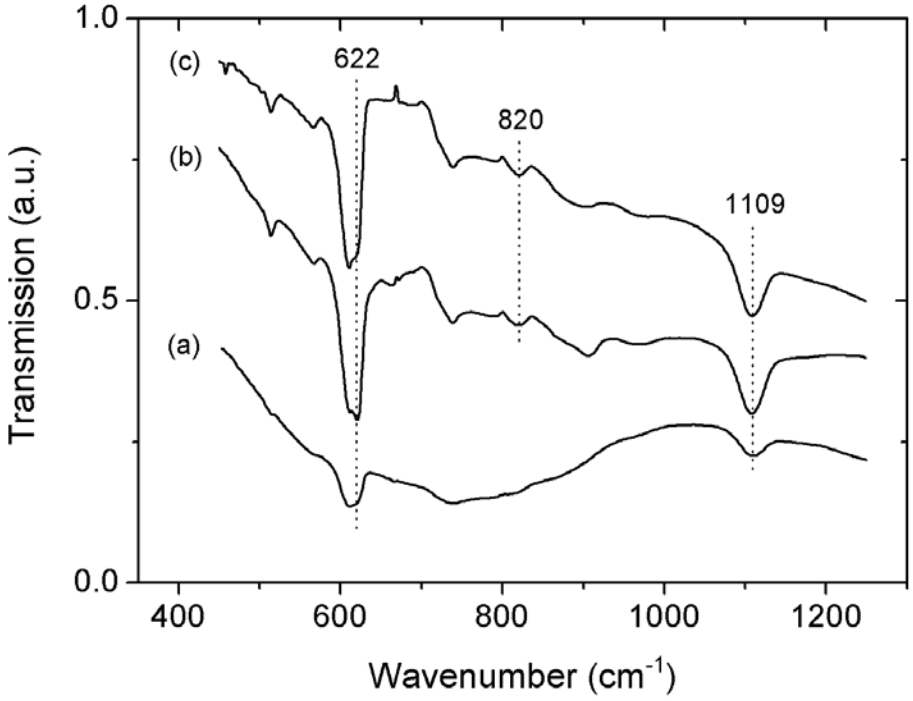

Figure 6.6: (a) shows *in-situ* FTIR spectra of Ag plating onto Si (b) FTIR spectra of the Ag NPs plated Si substrate (c) FTIR spectra of a Si substrate with 2-3 nm of native oxide.

In Fig. 6.6, Si-H wagging mode (622 cm^{-1}), O-Si-O stretching mode (820 cm^{-1}), Si-H bending mode (906 cm^{-1}), and Si-O-Si stretching mode (1110 cm^{-1}) are observed

[155, 156] which indicate the presence of silicon oxide at Ag/Si interface during the Ag plating reaction.

6.3.4 Mechanism of Ag plating

Based on our experimental results, we can conclude that galvanic displacement plating of Ag on Si proceeds via deposition of Ag upon reduction by taking electrons from Si, followed by formation of SiO_x, and dissolution of formed SiO_x into the etching solution as H_2SiF_6. Following chemical reactions describe the Ag plating process as supported by in-situ Raman data. Here 'x' defines the stoichiometry of silicon oxide, 'n' defines the valence of Si and 'ΔG' refers to change in Gibbs free energy in units of Kcal/mol. We calculated ΔG only for the balanced chemical equations by using standard free energy of formation [157] and keeping x =2. In all cases ΔG is found to be negative which implies spontaneity of these reactions.

$Ag^+ + e^- \rightarrow Ag$, $\Delta G \approx$-77 Kcal/mol (Reduction of Ag)

$SiH_4 + x\ H_2O + (n + 4)h^+ \rightarrow SiO_x + (n + 4)H^+$, with x = 0.1 to 2, y = 1 to 4, n ≈ 2 to 4,

$\Delta G \approx$-105 Kcal/mol for oxidation of Si

$SiO_x + 6HF \rightarrow H_2SiF_6$ (aqueous) + xH_2O, $\Delta G \approx$-33 Kcal/mol for etching of Si oxide

$2H^+ + e^- \rightarrow H_2$ (gas), $\Delta G \approx$0 Kcal/mol for hydrogen evolution

The above chemical reactions in conjunction with electron microscopy and in-situ Raman spectroscopy provide the essence of electroless Ag plating on Si by galvanic displacement. Ag ions get reduced on Si surface by taking electrons from Si which results in injection of holes into valence band of Si. Injected holes and water molecules react with Si to form silicon oxide which is eventually dissolved by HF providing a clean

Ag/Si interface where further reduction of Ag ions occurs. Hydrogen gas evolution also occurs spontaneously by recombination of protons with electrons. Our experimental findings are in agreement with the Ag plating model proposed by Kalkan et. al. [155]. Kalkan et. al. proposed the following reduction-oxidation reaction for the electroless plating of Ag on Si:

$SiH_x + 2Ag^+ + 2NO_3^- + H_2O \rightarrow SiO_2 + 2Ag + 2H^+ + 2NO_3^- + (1 + x/2)\ H_2$

Here, hydrogen terminated Si gets oxidized and Ag gets reduced (plated) on the Si substrate. It is to be noted that if the plating solution does not contain HF then the galvanic displacement reaction will be terminated soon. Because SiO_2 layer formed at Ag/Si interface will inhibit the transfer of charge across Ag/Si interface which in turn will inhibit the reduction of Ag ions.

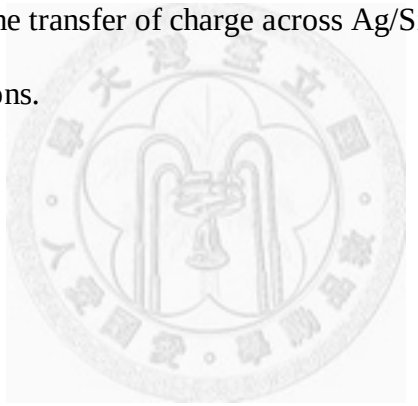

Chapter 7 Ag assisted etching of Si

7.1 Aim

Section 1.5 of chapter 1 of this thesis describes in detail the noble metal (e.g.: Ag, Au) assisted etching of Si substrates. This type of wet chemical etching has been used for fabrication of wide variety of Si nanostructures [57-66]. In particular the Ag-assisted etching of Si in an aqueous solution of HF and H_2O_2 has drawn special attention because of its ability to perform directional etching of nanostructures with high aspect ratio into Si. Many mechanisms have been proposed to explain the Ag-assisted Si etching [57, 58, 64]. However, the etching mechanism remains ambiguous because of lack of direct experimental evidence. Therefore, we conducted the *in-situ* Raman [158] and Fourier transform infrared (FTIR) [156] characterization to elucidate the chemical mechanism of the Ag-assisted Si etching. Further, we applied our results to explain the high speed directional etching of Si assisted by Ag nanoparticles.

7.2 Experiments

7.2.1 Cleaning of Si substrates

p-type Si(100) substrates (10 Ω·cm resistivity) were cleaned by sonication in acetone, methanol and deionized water (18.2 MΩ·cm resistivity) for 5 minutes separately. Immersing such substrates in 1% HF solution for 5 minutes followed by rinsing in deionized water for another 5 minutes results in formation of hydrogen (H) terminated Si surface.

7.2.2 Ag assisted Si etching

For Ag nanoparticles (NPs) plating, the cleaned Si substrates were immersed in an aqueous solution of 2 M silver nitrate ($AgNO_3$) and 50 mM HF for 5 minutes. Ag NPs plated Si substrates are etched for 10 minutes in aqueous solutions of different HF and H_2O_2 compositions. Etching is performed in solutions with fixed H_2O_2 concentrations (0.05 M and 0.5 M) and varying HF concentrations (2.3 M, 4.8 M and 10 M). In another set of experiments, Ag NPs plated Si substrates were also etched in aqueous solutions of different HF and H_2O_2 compositions (1 M HF & 0.5 M H_2O_2, 5 M HF & 0.5 M H_2O_2; and 5 M HF & 2.5 M H_2O_2).

7.2.3 Characterization

Morphologies of Ag NPs on Si and etched Si substrates were recorded using scanning electron microscope (SEM). The Raman measurements were performed on a commercial HR800, Jobin-Yvon Raman spectrometer using a 632.8 nm He-Ne laser light as the excitation source. Laser beam is focused with a 50× objective lens (0.5 NA, 10 mm WD) onto the sample resulting in an irradiation power density of 10^5 W/cm^2. The scattered radiation was collected backward with the same objective lens and then was sent through a Raman notch filter to an 80-cm monochromator. The dispersed spectrum was detected by a liquid nitrogen-cooled charge-coupled device camera. The Raman spectrometer has a spectral resolution of < 7 cm^{-1} and a Raman-shift error of < 0.1 cm^{-1} as determined by a calibration procedure. Data accumulation time of each spectrum was 2 min. During the *in-situ* Raman measurements, the samples were placed inside a Teflon container and immersed in the etching solution. A low-fluorescence glass plate (150 μm

thickness) is used to cover the container and prevent the evaporated gases of HF and H_2O_2 from corroding the objective lens. Surface of the etching solution was 2 mm above the sample surface and 3 mm below the protecting glass plate. The Raman spectra of the resultant porous Si and the etching solution after the reaction were also recorded for comparison.

Infrared absorption spectra were acquired in transmission mode using a commercial Nicolet Magna II 550 Fourier-transform infrared (FTIR) spectrometer with a spectral resolution of < 0.1 cm^{-1}. Ag NPs plating occurs on both front and back surfaces of the Si substrates, therefore the etching reaction proceeds on both surfaces in the etching solution. After etching for 30 min, the Si substrates, which possess several microns long nanochannels, were removed from the etching solution and immediately mounted on the sample stage of the FTIR spectrometer. We recorded *in-situ* FTIR spectra with data accumulation time of 10 sec for each spectrum. Such measurements can be considered as *in-situ* characterization owing to the following five facts. First, the residual etching solution (thickness $\approx$ 30 -50 μm as estimated by optical microscope) was observable to naked eyes on both surfaces of the samples even after the FTIR measurements. Second, after removing the samples from the etching solution and keeping them in vertical position for 15 sec, its surface was observed under optical microscope. Gas bubbles of about 2-5 μm diameters were found to be forming and bursting in the entire residual etching solution layer. Gas evolution is a signature of the ongoing Si etching process. Gas evolution was found to seize within 30 sec after withdrawing the sample from the etching solution. Third, after withdrawing the Si samples from the etching solution and keeping them mounted in vertical position on the stage of FTIR

spectrometer, the FTIR spectra showed the characteristic dips identical to those of the etching solution. These dips were only observed in the high wave number regime for duration of about 30 sec. Fourth, there was no observable evolution of *in-situ* FTIR spectra during first 10-20 sec of the spectral recording. Fifth, Vlassiouk *et al*. [159] studied wetting-dewetting behavior of hydrophobic mesoporus membranes (pore diameter ≈ 20 nm). They reported that large activation energy barrier ($\Delta F > 10^3 K_B T$, K_B = Boltzmann constant, and T = temperature) makes the dewetting very slow process and occurring at non-measurable rate for pore radius > 5nm. Therefore, the capillary action of Si nanochannels is expected to retain the etching solution and the Si etching should continue for several seconds even after removal of the substrates from the etching solution.

The samples were subsequently rinsed in H_2O and blown dried with N_2 gas. Another FTIR measurement was taken on such samples afterwards. Similar to the Raman study, an FTIR spectrum of a cleaned Si substrate (without Ag plating) was recorded after undergoing the etching in aqueous solution of 5 M HF & 0.5 M H_2O_2, and cleaning.

7.3 Results and Discussion

7.3.1 Morphologies of etched Si

Morphologies and characteristics of the Ag NPs plated Si substrates have been described in section 6.3.1 of chapter 6 of this thesis. Etching of Ag NPs plated Si in 0.05 M H_2O_2 and 2.3 M HF solution results in formation of nanochannels with porosity on sidewalls. Many lateral etch holes are also observed as shown in Fig. 7.1(a). Fig. 7.1(b) shows that upon increasing the HF concentration to 4.8 M, the crystallinity of sidewalls

of nanochannels is restored accompanied with reduction in number of lateral etch holes. Increase in the HF concentration to 10 M results in formation of silicon nanowires of about 50 nm diameter as shown in Fig. 7.1(c). In addition, almost no lateral etch holes are observed in nanowires. Average etch depth of silicon is found to be 1.5 µm, 2 µm, and 3.5 µm when HF concentration is 2.3 M, 4.8 M, and 10 M respectively. Increase in the etch depths with the increase in HF concentration is not linear which shows an increased range of lateral etching as supported by formation of nanowires, Fig. 7.1(c).

Etching Ag plated Si substrates in 0.5 M H_2O_2 and 2.3 M HF solution results in formation of nanochannels with microporous topwalls of nanochannels but almost no lateral etch holes are seen as shown in Fig. 7.1(d).

Fig. 7.1(e) shows straight nanochannels and a few lateral holes when etching is performed in 0.5 M H_2O_2 and 4.8 M HF solution. With the increase of HF concentration to 10 M primarily aligned deep nanochannels along with many partially curved nanochannels are observed as shown in Fig. 7.1(f). No nanowire formation is observed when etching is performed in 10 M HF and 0.5 M H_2O_2 aqueous solution because the enhanced sinking speed of Ag NPs into Si limits the lateral etching range, which is in agreement with average etch depth of silicon changing from 1.2 µm, 4 µm, and 10 µm when the HF concentration is 2.3 M, 4.8 M, and 10 M respectively.

Fig. 7.2 shows the SEM images of the Si substrates after etching of Ag NPs plated Si in aqueous solutions of 1 M HF & 0.5 M H_2O_2 (Fig. 7.2(a) and 7.2(b)), 5 M HF & 0.5 M H_2O_2 (Fig. 7.2(c) and 7.2(d)); and 5 M HF & 2.5 M H_2O_2 (Fig. 7.2(e) and 7.2(f)) respectively. Plan view SEM images (Fig 7.2(a), 7.2(c), and 7.2(e)) show circular holes

corresponding to size of plated Ag NPs and cross sectional SEM images (Fig. 7.2(b), 7.2 (d), 7.2(f)) show nanochannels formed into Si.

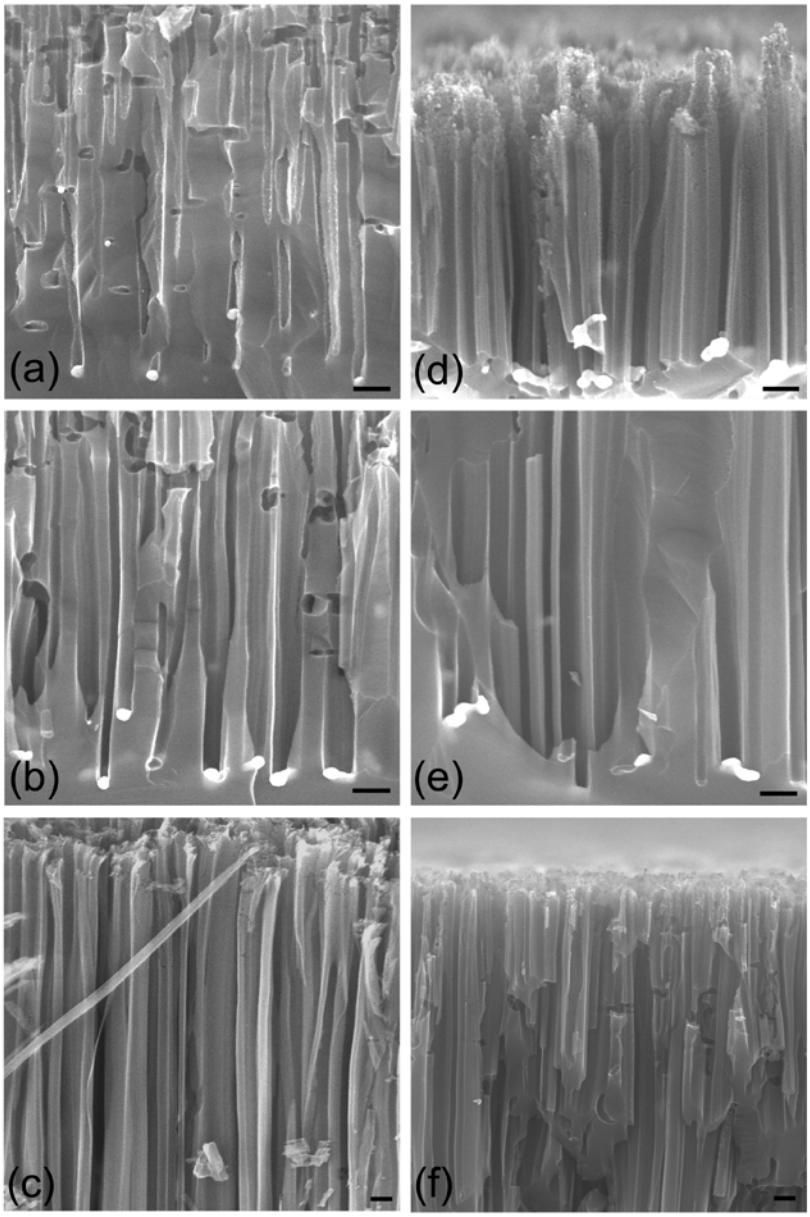

Figure 7.1: Cross sectional SEM images of Si(100) after etching of Ag NPs plated Si in aqueous solution of different compositions. (a), (b), and (c): 0.05 M H_2O_2 and 2.3 M HF, 4.8 M HF and 10 M HF respectively. (d), (e), (f): 0.5 M H_2O_2 and 2.3 M HF, 4.8 M HF and 10 M HF respectively. Scale bar = 100 nm.

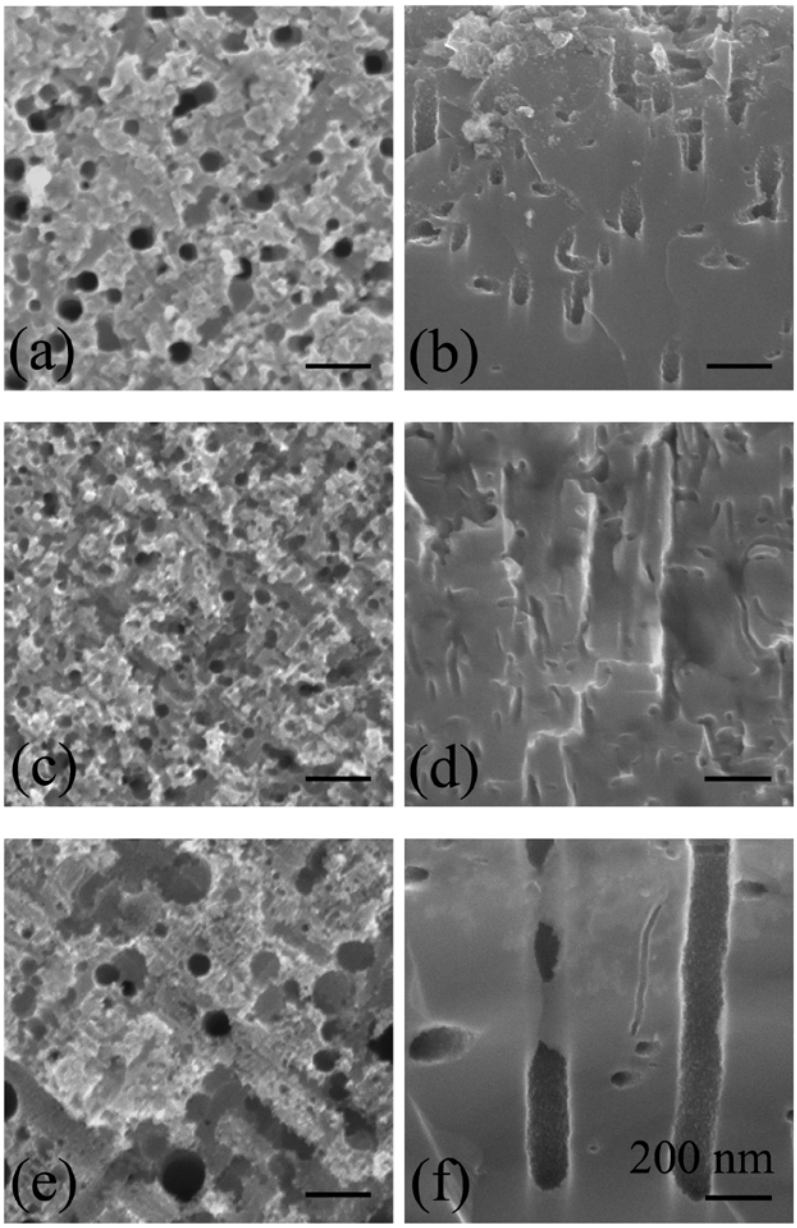

Figure 7.2: Plan view and cross-sectional SEM images of the Si substrates after etching of Ag NPs plated Si in aqueous solutions of 1 M HF and 0.5 M H_2O_2 (2a and 2b), 5 M HF and 0.5 M H_2O_2 (2c and 2d), and 5 M HF and 2.5 M H_2O_2 (2e and 2f) respectively. Scale bar = 200 nm for all images.

In addition to nanochannles, Fig. 7.1 and Fig. 7.2 also show meso-micro-porous Si which is formed in the vicinity of Ag NPs during the etching of Si.

7.3.2 Raman spectra

In Fig. 7.3, Fig. 7.3 (a) and 7.3 (b) show the *in-situ* Raman spectra of the clean Si surface in the etching solution (5 M HF & 0.5 M H_2O_2) and of Ag NPs assisted Si etching respectively. Fig. 7.3 (c) and 7.3 (d) show the Raman spectrum of the formed porous Si and used etching solution. A weak shoulder around 230 cm^{-1}, peaks at 302 cm^{-1} (2 transverse acoustic mode), 520 cm^{-1} (transverse optical (TO) mode), 435 cm^{-1} & 620 cm^{-1} (2 longitudinal acoustic mode) and 940 cm^{-1} (2 TO mode) are assigned to Si [151]. Peak at 876 cm^{-1} is assigned to H_2O_2 [160]. A very weak-broad weak peak at 391 cm^{-1} and a medium intensity peak at 657 cm^{-1} are assigned to the peaks of silicon-hexafluoride ion (SiF_6^{2-}) in the Raman spectra of H_2SiF_6 in water [153].

Ag NPs assisted Si etching produces nanoholes (20 to 100 nm diameter) into Si but significant broadening of the Si peak at 520 cm^{-1} and extension of the peak tail up to 470 cm^{-1} in Fig. 7.3 (b) and 7.3 (c) indicates the formation of the meso-micro-porous Si (pores of 2-5 nm size) also [161]. In addition to formed Si nanoholes and meso-micro-porous Si, the presence of Ag also enhances the Raman scattering of peaks of Si. Therefore, the Raman spectra Fig. 7.3(b) and Fig. 7.3(c) indicate the formation of the meso-micro-porous Si in the vicinity of the Ag nanoparticles. Our speculation is in agreement with SEM images shown in Fig. 7.2.

As a final note on the Raman investigation, both spectrum (b) and (c) show a broadened 520 cm^{-1} peak, compared with that of the pristine silicon sample, indicating a phonon-confinement effect caused by the formed porous Si nanostructures.

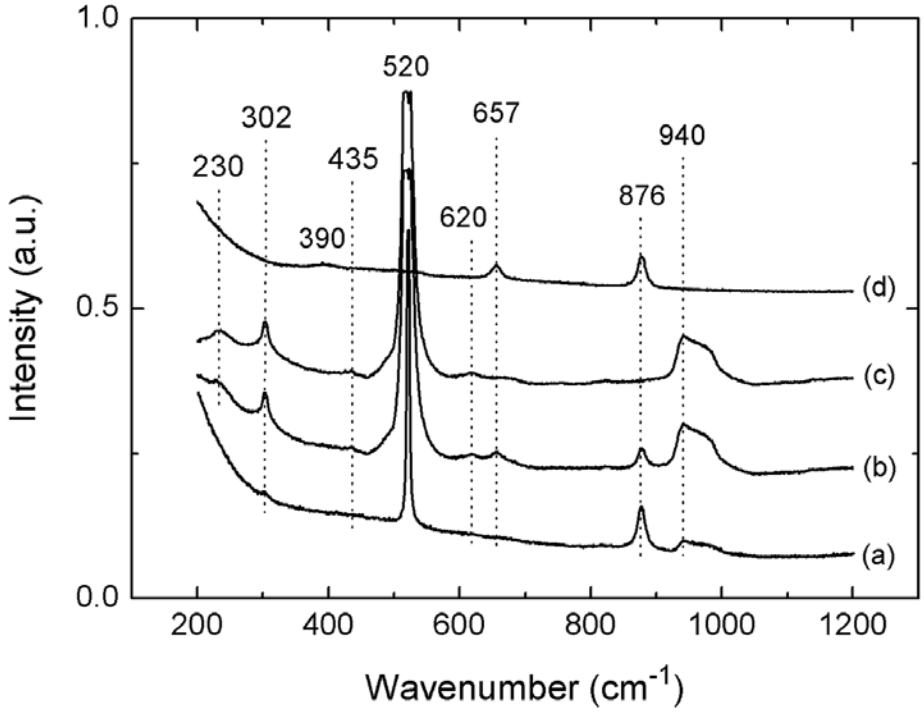

Figure 7.3: *In-situ* Raman spectra of the Si surface in the etching solution (5 M HF and 0.5 M H_2O_2) (a) without Ag nanoparticles, and (b) with Ag nanoparticles. Raman spectra of (c) porous Si and (d) used etching solution. Peaks at 230 cm^{-1}, 302 cm^{-1} (2 transverse acoustic mode), 520 cm^{-1} (transverse optical (TO) mode), 435 cm^{-1} & 620 cm^{-1} (2 longitudinal acoustic modes) and 940 cm^{-1} (2 TO mode) are assigned to Si. Peak at 876 cm^{-1} is assigned to H_2O_2. Peaks at 391 cm^{-1} and 657 cm^{-1} are assigned to silicon-hexafluoride ion (SiF_6^{2-}). All the spectra are recorded using 632.8 nm He-Ne laser light operating at 10 mW power, and have been normalized to unity, and shifted along y-axis for clear presentation.

In-situ Raman spectra in Fig 7.3 revealed only the formation of micro-meso-porous Si as intermediate and H_2SiF_6 as end product of the etching reaction. Therefore, we only investigated the *in-situ* Raman spectra of Ag NPs assisted etching in the aqueous solution of 5 M HF & 0.5 M H_2O_2.

7.3.3 FTIR spectra

In Fig. 7.4, Fig. 7.4(a) shows an FTIR spectrum of a H-Si substrate (without Ag NPs plating) after the etching in aqueous solution of 5 M HF and 0.5 M H_2O_2, rinsing in deionized water, and blow drying using N_2 gas. It shows peaks at 622 cm^{-1} (Si-H wagging mode) and a bump at 1110 cm^{-1} (Si-O-Si stretching mode) [155, 156]. This implies the partial coverage of its surface by silicon oxide. Fig. 7.4(b) shows *in-situ* FTIR spectrum of the Ag NPs assisted Si etching. In addition to water band at 1640 cm^{-1}; peaks at 622 cm^{-1} and 1110 cm^{-1}, and weak bumps at 2100 cm^{-1} (Si-H stretching modes) are observed. Fig. 7.4(c) shows FTIR spectrum of the formed porous Si after rinsing with deionized water and drying. Here additional bands at 820 cm^{-1} (O-Si-O stretching mode), 906 cm^{-1} (Si-H bending mode), and a double bump at 2100 cm^{-1} (Si-H stretching modes) are observed [156]. These additional bands are not observable in the *in-situ* FTIR spectrum because of dominance of IR spectrum of water. Spectra in Fig 7.4 indicate the formation of silicon oxide as intermediate during the Ag assisted Si etching.

Although we observed silicon oxide signal in FTIR spectra (Fig. 7.4), but the role of water in oxidation of the formed porous Si is not evident. Therefore, we conducted another set of *in-situ* FTIR experiments. In Fig 7.5, Fig. 7.5(a), 7.5(b) and 7.5(c) show the *in-situ* FTIR spectra upon etching of Ag NPs plated Si in aqueous solutions of 1 M HF & 0.5 M H_2O_2, 5 M HF & 0.5 M H_2O_2, and 5 M HF & 2.5 M H_2O_2 respectively. Fig. 7.5(d), 7.5(e) and 7.5(f) show the corresponding *in-situ* FTIR spectra after 10x dilution of the etching solutions while keeping the etched Si substrates immersed in their respective etching solution. All spectra show the Si-O-Si stretching mode peak at 1110 cm^{-1} and with comparable intensity of peaks before and after dilution of the etching solution.

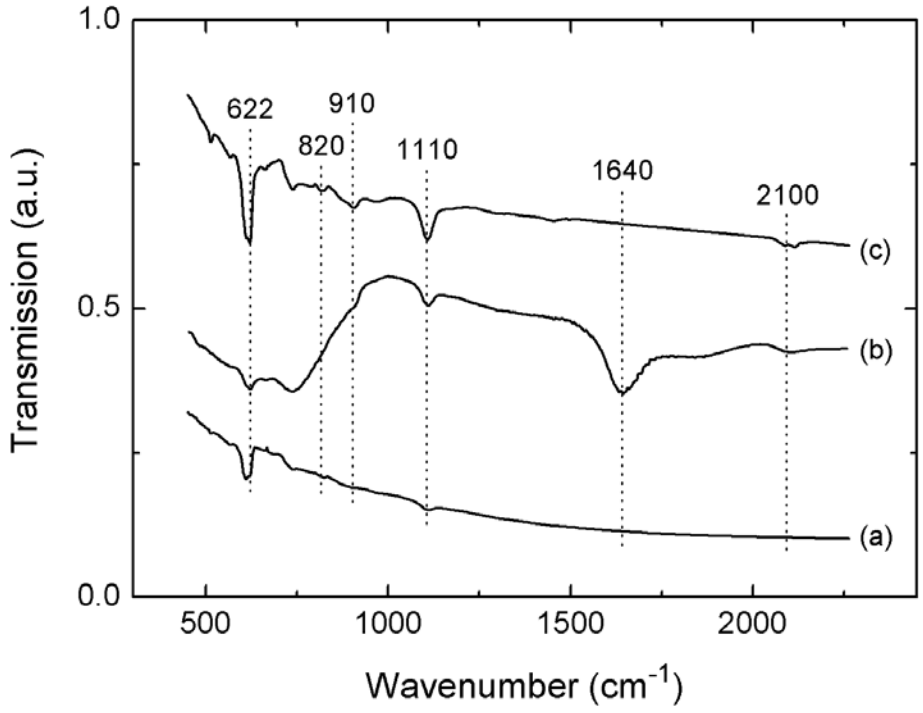

Figure 7.4: (a) FTIR spectrum of a H-Si substrate after immersion in aqueous solution of 5 M HF and 0.5 M H_2O_2 for 10 min and rinsing in H_2O and blow drying using N_2 gas. (b) *In-situ* FTIR spectrum of Ag-assisted Si etching (c) FTIR spectrum of porous Si. Peak at 622 cm^{-1} (Si-H wagging mode), 820 cm^{-1} (O-Si-O stretching mode), 906 cm^{-1} (Si-H bending mode), 1110 cm^{-1} (Si-O-Si stretching mode), 1640 cm^{-1} (vibration mode of water) and 2100 cm^{-1} (Si-H stretching modes) are observed. All spectrums have been normalized to unity and shifted along y-axis for clear presentation.

Further, it is known that reaction of fluorine and hydrogen terminated Si surface with water yields Si-OH which has IR band at 3600 cm^{-1} [162, 163]. Therefore, water does not promote oxidation of the formed porous Si and silicon oxide is formed at Ag/Si interface during the Si etching.

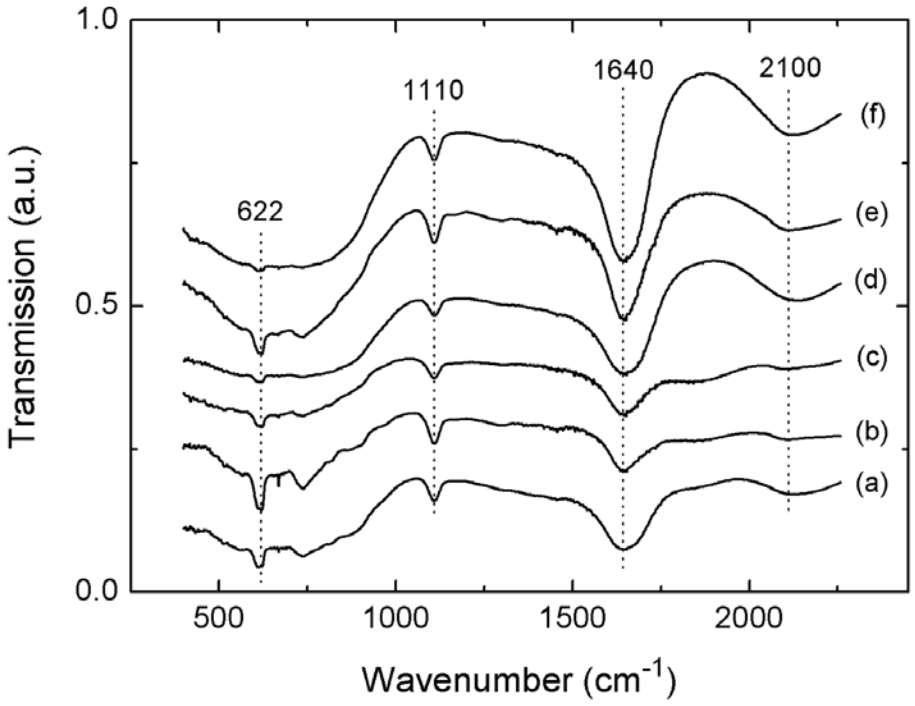

Figure 7.5: (a), (b), and (c) *In-situ* FTIR spectra upon etching of Ag NPs plated Si in aqueous solutions of 1 M HF & 0.5 M H_2O_2, 5 M HF & 0.5 M H_2O_2, and 5 M HF & 2.5 M H_2O_2 respectively. Spectra (d), (e) and (f) show the corresponding *in-situ* FTIR spectra after 10x dilution of the etching solutions while keeping the etched Si substrates immersed in their respective etching solution. Peak at 622 cm^{-1} (Si-H wagging mode), 1110 cm^{-1} (Si-O-Si stretching mode), 1640 cm^{-1} (vibration mode of water) and 2100 cm^{-1} (Si-H stretching modes) are observed. All spectrums have been normalized to unity and shifted along y-axis for clear presentation.

7.3.4 Mechanism of Ag assisted Si etching

In aqueous HF and H_2O_2 solution, silicon oxide is formed due to oxidation of Si by H_2O_2 and formed oxide is etched away by HF. But the etching rate of Si is negligibly small because most of the Si surface is primarily H-terminated and is difficult to be

oxidized and etched. It is known that deposition of Ag on Si enhances the etching rate of Si beneath the Ag NPs. A clean Ag surface is hydrophilic which causes wetting of the Ag surface by the aqueous etching solution followed by the reduction of H_2O_2 on the Ag surface accompanied with injection of holes into Si. Reaction of hole injected Si with water results in formation of silicon oxide which will be etched by HF to yield H_2SiF_6. This leads to the formation of the miroporous Si in vicinity of the Ag NPs followed by oxidation and dissolution of the mircoporous Si. Oxidation and etching of miroporous Si is a faster process. This pathway explains the high-speed etching of Si by the Ag NPs and it is consistent with models proposed by Peng. et. al. [57] and Mohamed et. al. [140]. Peng et.al proposed that etching of Si proceeds with reduction of H_2O_2 on metal surface accompanied with oxidation of Si and dissolution of oxidized Si by HF. Mohamed et. al. proposed the formation of microporous Si beneath the Ag NPs followed by oxidation of Si and dissolution of oxidized Si by HF to explain the high-speed etching of Si.

Following chemical reactions describe the Ag assisted Si etching process as supported by in-situ Raman and FTIR data. Here 'ΔG' refers to change in Gibbs free energy in units of Kcal/mol. We calculated ΔG only for the balanced chemical equations by using standard free energy of formation [157]. It is to be noted that in all cases ΔG is found to be negative which implies spontaneity of these reactions.

(1) $H_2O_2 + 2H^+ + 2e^- \rightarrow 2H_2O$, $\Delta G \approx$-78 Kcal/mol for reduction of hydrogen proxide

(2) Si (microporous) + $2H_2O + 4h^+ \rightarrow SiO_2 + 4H^+$, $\Delta G \approx$-91 Kcal/mol for formation of silicon oxide

(3) $2H^+ + 2e^- \rightarrow H_2$ (gas), ΔG = 0 Kcal/mol for hydrogen gas evolution

(4) $SiO_2 + 6HF \rightarrow H_2SiF_6$ (aqueous) + $2H_2O$, $\Delta G \approx$-33.73 Kcal/mol for etching of silicon oxide

Overall chemical reaction: $Si + H_2O_2 + 6\ HF \rightarrow H_2SiF_6$ (aqueous) + H_2 (gas)

It has been reported by us that maintenance of sub-nanometer oxide between the Ag/Si interface and AgNP-Si interaction are some of the key parameters which regulate the directional etching of Si by Ag NPs [164]. HF etches silicon oxide isotropically, which indicates that reduction of H_2O_2 accompanied by oxidation of Si governs the directional etching of Si. During the Ag NPs assisted Si etching in the aqueous HF and H_2O_2 solution, the surface of Si is primarily passivated either by –H or –OH bonds or by –F bonds. It is known that the probability to charge transfer across the Si-OH bond is higher than that across the Si-H or Si-F bonds [144]. In addition, the H-Si(100) or F-Si(100) surfaces are easy to oxidize in an aqueous or oxygen environment as compared with Si(111) surfaces because they have 4-5 times higher density of surface states [145]. Therefore, the injection of holes along Si [100] is favored which in turn promotes directional oxidation and etching of Si. This model is supported by the observed peak of silicon oxide at 1110 cm^{-1} as shown in Fig. 7.4(b) and 7.4(c), and in spectra of Fig 7.5. Intensity of the silicon oxide peak indicates that the oxide is formed as a reaction intermediate in Ag-assisted Si etching because oxidation rate of HF or HF + H_2O_2 treated Si in air or water [139] is very low and would only yield a small bump at 1110 cm^{-1} as shown in Fig. 7.4(a).

We have investigated the Ag-assisted etching of Si in acidic HF and H_2O_2 solution and elucidated its chemical mechanism. Although, our experimental results are consistent

with the models proposed in literature references on Ag assisted etching of Si [57, 140, 165, 166], but our findings should not be generalized to etching of Si in HF solutions. Jia et. al. conducted stain etching of Si in $NaNO_2$ and HF solution, and found Si-O-Si stretching band at 1100 cm^{-1} in the FTIR spectra of the formed porous Si which indicates formation of silicon oxide as intermediate [167]. On the other hand, Dudley et. al. conducted stain etching of Si in HF + $FeCl_3$ + H_2SO_4 solution and found only Si-H vibration modes in the FTIR spectra of the formed porous Si even after 30 minutes of air exposure which indicates direct etching of Si [168, 169]. Therefore, depending on chemical composition of the etching solution and etching conditions, the Si etching pathway can also differ.

Chapter 8 Conclusions

8.1 Ordered arrays of Ag nanoparticles by constrained self organization

Thermal annealing of thin Ag film, deposited at low temperature onto FIB patterned Si(100) substrate, in inert environment causes the aggregation of Ag on the FIB-irradiated locations. By carefully tuning the deposition and annealing temperature, lattice constant of the aggregation centers, and ion beam dose, ordered array of Ag nanoparticles with uniform size are fabricated. In principle, this method based on FIB irradiation can be exploited for the creation of aggregation lattices on other materials and used for the fabrication of various ordered arrays of nanoparticles via a constrained self-organization process.

8.2 Probing surface plasmon of individual Ag nanoparticles by scanning transmission electron microscopy (STEM)

The spatially resolved investigation of the SP characteristics in individual Ag nanoparticles (~30 nm) in the ultra-violet spectral regime has been achieved using STEM-EELS. The NP shows a prominent SP resonance at ~3.5 eV (~355 nm) and a broad surface excitation at ~7.0 eV (~177 nm), both of which are in good agreement with the associated STEM-EELS calculations. STEM-EELS mapping was further performed to reveal the spatial distributions of these surface excitations, and the dipolar near-field characteristics with remarkable field enhancements imaged for the 3.5-eV SP could be of practical implications for plasmonics and ultra-sensitive sensing by SERS.

8.3 Fabrication of Singlet, doublet, and triplet of Ag nanoparticles in AAO

Single, double, and triple Ag nanoparticles were electrochemically grown into custom designed AAO templates which were prepared by FIB patterning of the AAO substrates. Dimers and trimers of Ag nanoparticles in AAO possess interparticle gap about 5 nm. This fabrication method allows the precise control over the position of the dimers and trimers, and interparticle separation. STEM-EELS and scanning near-field microscopy (SNOM) mapping of the fabricated dimers and trimers is under investigation.

8.4 Directional etching of silicon by silver nanostructures

Directional etching of the nanostructures (nanoholes, nanorings, and nanotrenches) into Si by different Ag nanopatterns has been achieved. We propose that the sticking of Ag to Si during etching and directional etching by Ag depend on Ag/Si interface oxide thickness.

8.5 Electroless Ag plating on Silicon

Electron microscopy and in-situ Raman and FTIR spectroscopy characterization was conducted to investigate the mechanism of the electroless Ag plating. Galvanic displacement plating of Ag on Si results in growth of nano-crystalline Ag nanoparticles on Si substrates which shows Volmer-Weber (island or nano-particle) type growth of Ag on Si substrates.

Raman and FTIR spectroscopy revealed that galvanic displacement plating of Ag on Si proceeds via deposition of Ag upon reduction by taking electrons from Si, followed

by formation of SiO_x, and dissolution of formed SiO_x into the etching solution as H_2SiF_6 providing a clean Ag/Si interface where further reduction of Ag ions occurs.

8.6 Ag assisted etching of Si

Electron microscopy images revealed that depending on the composition of the etching solution the morphologies of the etched Si nanostructures vary. Self organized array of Si nanoholes and nanowires can be grown by Ag-assisted Si etching simply by tuning the composition of the etching solution.

In-situ Raman and FTIR spectroscopy is used to empirically establish the chemical mechanism of the Ag-assisted Si etching. Microporous Si and silicon oxide are revealed as etching reaction intermediates and H_2SiF_6 is detected as an end product of the Si etching. Etching proceeds via formation of microporous silicon oxide followed by dissolution of oxide into solution as H_2SiF_6. We believe that our work will enhance the use of *in-situ* Raman and FTIR spectroscopy to study other reactions like catalysis and toxicology, where interactions between the reactants (or products) and the surfaces of metal catalyst are significant and help shed some lights on the mechanisms of reactions.

Bibliography

1. M. Kaur, S. Bhattacharya, M. Roy, S. K. Deshpande, P. Sharma, S. K. Gupta, J. V. Yakhmi, *Growth of nanostructures of Zn/ZnO by thermal evaporation and their application for room-temperature sensing of H_2S gas*, Applied Physics A, **87**, 91 (2007).

2. G. Yi, C. Wang, and Wong II Park, *ZnO nanorods: synthesis, characterization and applications*, Semiconductor Science and Technology, **20**, S22 (2005).

3. Pradeep Sharma, C. Y. Liu, Chen-Feng Hsu, N. W. Liu, Y. L. Wang, *Ordered arrays of Ag nanoparticles grown by constrained self organization*, Applied Physics Letters, **89**, 163110 (2006).

4. Y. Zhang, L. Sun, Y. Fu, Z. C. Huang, X. J. Bai, Y. Zhai, J. Du, H. R. Zhai, *The shape anisotropy in the magnetic filed-assisted self-assembly chain-like structure of magnetite*, Journal of Physical Chemistry C, **113**, 8152 (2009).

5. J. Wu, Q. Gu, B. S. Guiton, N. P. de Leon, L. Ouyang, H. Park, *Strain-induced self organization of metal-insulator domains in single -crystalline VO_2 nanobeams*, Nano Letters, **6**, 2313 (2006).

6. C. Papaseit, N. Pochon, J. Tabony, *Micro-tubule self organization is gravity dependent*, Proceedings of National Academy of Sciences, **97**, 8364 (2000).

7. Y. Yin, Y. Lu, B. Gates, Y. Xia, *Template-assisted self-assembly: a practical route to complex aggregates of monodispersed colloids with well-defined sizes, shapes and structures*, Journal of American Chemical Society, **123**, 8718 (2001).

8. H. Duan, K.K. Berggren, *Directed self assembly at the 10 nm scale by using capillary force-induced nanocohesion*, Nano Letters, **10**, 3710 (2010).

9. D. Qin, Y. Xia, B. Xu, H. Yang, C. Zhu, G. M. Whitesides, *Fabrication of ordered two dimensional arrays of micro- and nanoparticles arrays by using patterned self-assembled monolayers as templates*, Advanced Material, **11**, 1433 (1999).

10. P. L. Stiles, J. A. Dieringer, N. C. Shah, R. P. Van Duyne, *Surface-Enhanced Raman Spectroscopy*, Annual Review Analytical Chemistry, **1**, 601 (2008).

11. W. A. Murray, J. R. Suckling, W. L. Barnes, *Overlayers on Silver Nanotriangles: Field Confinement and Spectral Position of Localized Surface Plasmon Resonances*, Nano Letters, **6**, 1772 (2006).

12. C.L. Nehl, H. W. Liao, J. H. Hafner, *Optical Properties of Star-Shaped Gold Nanoparticles*, Nano Letters, **6**, 683 (2006).

13. M. J. Bloemer, M. C. Buncick, R. J. Warmack, *Surface electromagnetic modes in prolate spheroids of gold, aluminum, and copper*, Journal of Optical Society of America B, **5**, 2552 (1988).

14. J. A. Creighton, D.G. Eadon, *Ultraviolet-visible absorption spectra of the colloidal metallic elements*, Journal of Chemical Society Faraday Transactions, **87**, 3881 (1991).

15. E. J. Zeman, G. C Schatz, *An accurate electromagnetic theory study of surface enhancement factors for silver, gold, copper, lithium, sodium, aluminum, gallium, indium, zinc, and cadmium*, Journal of Physical Chemistry, **91**, 634 (1987).

16. G. H. Chan, J. Zhao, *Plasmonic Properties of Copper Nanoparticles Fabricated by Nanosphere Lithography*, Nano Letters, **7**, 1947 (2007).

17. C. Langhammer, Z. Yuan, I. Zoric, B. Kasemo, *Plasmonic Properties of Supported Pt and Pd Nanostructures,* Nano Letters, **6**, 833 (2006).

18. K. L. Kelly, E. Coronado, L. L. Zhao, G. C. Schatz, *The optical properties of metal nanoparticles: The influence of size, shape and dielectric environment*, Journal of Physical Chemistry B, **107**, 668 (2003).

19. C. P. Collier, R. J. Saykally, J. J. Shiang, S. E. Henrichs, J. R. Heath, *Reversible Tuning of Silver Quantum Dot Monolayers Through the Metal-Insulator Transition*, Science, **277**, 1978 (1997).

20. F. Hubenthal, T. Ziegler, C. Hendrich, M. Alschinger, F. Träger, *Tuning the surface plasmon resonance by preparation of gold-core/silver-shell and alloy nanoparticles*, European Physics Journal D, **34**, 165 (2005).

21. H. Makoto, K. Ashok, *Wavelength tuning of surface plasmon resonance by annealing silver-copper nanoparticles*, Journal of Applied Physics, **100**, 014309 (2006).

22. F. J. Beck, K. Catchpole, *Red-shifting the surface plasmon resonance of silver nanoparticles for light trapping in solar cells*, Material Research Society Symposium Proceedings, **1101,** KK03-04 (2008).

23. B. M. Ross, L. P. Lee, *Plasmon tuning and local field enhancement maximization of the nanocrescent*, Nanotechnology, **19**, 275201 (2008).

24. S. Biring, H.-H. Wang, J.-K. Wang, and Y.-L. Wang, *Light scattering from 2D arrays of monodispersed Ag-nanoparticles separated by tunable nano-gaps: spectral evolution and analytical analysis of plasmonic coupling*, Optics Express, **16**, 15312 (2008).

25. P. K. Jain, W. Huang, M. A. El-Sayed, *On the Universal Scaling Behavior of the Distance Decay of Plasmon Coupling in Metal Nanoparticle Pairs: A Plasmon Ruler Equation*, Nano Letters, **7**, 2080 (2007).

26. S. Malynch, G. Chumanov, *Light-Induced Coherent Interactions between Silver Nanoparticles in Two-Dimensional Arrays*, Journal of American Chemical Society, **125**, 2896 (2003).

27. S. A. Maier, *Plasmonics: Fundamentals and Applications*, (Springer, 2006).

28. H. Raether, *Excitation of Plasmons and Interband Transitions by Electrons*, (Springer, 1979).

29. M. Bosman, V. J. Keast, M. Watanabe, A. I. Maaroof, M. B. Cortie, *Mapping surface plasmons at the nanometre scale with an electron beam*, Nanotechnology, **18**, 165505 (2007).

30. F. Li, L.Zhang, R. M. Metzer, *On the growth of highly ordered pores in anodized aluminum oxide*, Chemistry of Materials, **10**, 2470 (1998).

31. H. Masuda, K. Fakuda, *Ordered metal nanoholes arrays made by a two step replication of honeycomb structures of anodic alumina*, Science, **268**, 1466 (1998).

32. H. Masuda, H. Yamada, M. Satoh, H. Asoh, M. Nakao, T. Tamamura, *Highly ordered nanochannel-array architecture in anodic alumina*, Applied Physics Letters, **71**, 2770 (1997).

33. C. Y. Liu, A. Datta, N. W. Liu, C. Y. Peng, Y. L. Wang, *Order-disorder transition of anodic alumina nanochannel arrays grown under the guidance of focused-ion-beam-patterning*, Applied Physics Letters, **84**, 2509, (2004).

34. Z. Sun, H. K. Kim, Growth of ordered, *single-domain, alumina nanopore arrays with holographically patterned aluminum films*, Applied Physics Letters, **81**, 3458, (2002).

35. W. Lee, R. Ji, C. A. Ross, U. Gosele, K. Nielsch, *Wafer-scale nickel imprint stamps for porous alumina membranes based on interference lithography*, Small **2**, 978 (2006).

36. H.-H. Wang, C.-Y. Liu, S.-B. Wu, N.-W. Liu, C.-Y. Peng, T.-H. Chan, C.-F. Hsu, J.-K. Wang, Y.-L. Wang, *Highly Raman-Enhancing Substrates Based on Silver Nanoparticle Arrays with Tunable Sub-10 nm Gaps*, Advanced Materials, **18**, 491 (2006).

37. D. Xu, D. Chen, Y. Xu, X. Shi, G. Guo, L. Gui, Y. Tang, *Preparation of II-VI group semiconductor nanowire arrays by dc electrochemical deposition in porous aluminum oxide templates*, Pure and Applied Chemistry, **72**, 127 (2000).

38. J. E. Weber, W. G. Yelton, A. Kumar; *Electrodeposition of $Bi_{1-x}Sb_x$ Nanowires as an Advanced Material for Thermoelectric Applications*, Functionalized Nanoscale Materials, Devices and Systems, page 425 (2008).

39. G. J. Strijkers, J. H. J. Dalderop, M. A. A. Broeksteeg, H. J. M. Swagten, W. J. M. de Jonghe, *Structure and magnetization of arrays of elctrodeposited Co wires in anodic alumina*, Journal of Applied Physics, **86**, 5141 (1999).

40. S. Grimm, R. Giesa, K. Sklarek, A. Langner, U. Gosele, H. W. Schmidt, M. Steinhart, *Nondestructive Replication of Self-Ordered Nanoporous Alumina Membranes via Cross-Linked Polyacrylate Nanofiber Arrays*, Nano Letters, **8**, 1954 (2008).

41. M. Zhang, Y. Bando, K. Wada, K. Kurashima, *Synthesis of nanotubes and nanowires of silicon oxide*, Journal of Materials Science Letters, **18**, 1911 (1999).

42. S. Biring, H. H. Wang, J. K. Wang, Y. L. Wang, *Light scattering from 2D arrays of monodispersed Ag-nanoparticles separated by tunable nano-gaps: spectral evolution and analytical analysis of plasmonic coupling*, Optics Express, **16**, 15312 (2008).

43. C. Carraro, R. Maboudian, L. Magagnin, *Metallization nanostructuring of semiconductor surfaces by galvanic displacement processes,* Surface Science Reports, **62**, 499 (2007).

44. K. P. Pernstich, M. Schenker, F. Weibel, A. Rossi, W. R. Caseri, *Electroless Plating of Ultrathin Films and Mirrors of Platinum Nanoparticles onto Polymers, Metals, and Ceramics,* ACS Applied Materials Interfaces, **2**, 639 (2010).

45. H. W. Kim, N. E. Lee, *Conformal electroless filling of Cu into patterned amorphous carbon layer modified by oxygen plasma and aminosilane treatments,* Journal of Vacuum Science and Technology B, **28**, 715 (2010).

46. Y. W. Song, D. Y. Shan, E. H. Han, *Corrosion behaviors of electroless plating Ni–P coatings deposited on magnesium alloys in artificial sweat solution*, Electrochimica Acta, **53**, 2009 (2007).

47. J. Skelly, *Decorative plating processes for common plastic resins: Resin selection as well as plastic part design is critical to matching the right finishing method with the intended application*, Metal Finishing, **106**, 61 (2008).

48. M. Hasegawa, N. Yamachika, S. D. Yosi, Y. Okinaka, T. Osaka, *Evidence for "superfilling" of submicrometer trenches with electroless copper deposit*, Applied Physics Letters, **90**, 101916 (2007).

49. A. Gutes, C. Carraro, R. Maboudian, *Silver Dendrites from Galvanic Displacement on Commercial Aluminum Foil as an Effective SERS Substrate,* Journal of Americal Chemical Society, **132**, 1476 (2010).

50. F. M. Liu, M. Green, *Efficient SERS substrates made by electroless silver deposition into patterned silicon structures,* Journal of Material Chemistry, **14**, 1526 (2004).

51. S. H. Lee, K. C. Bantz, N. C. Lindquist, S. H. Oh, L. H. Christy, *Self-Assembled Plasmonic Nanohole Arrays*, Langmuir, **25**, 13685 (2009).

52. M. Mohl, A. Kumar, A. L. M. Reddy, A. Kukovecz, Z. Konya, I. Kiricsi, R. Vajtai, P. M. Ajayan, *Synthesis of Catalytic Porous Metallic Nanorods by Galvanic Exchange Reaction*, Journal of Physical Chemistry C, **114**, 389 (2010).

53. V. Bogush, *Application of Electroless Metal Deposition for Advanced Composite Shielding Material,* Journal of Optoelectronics and Advanced Material, **7**, 1635 (2005).

54. N. A. Malvadkar, G. Demirel, M. Poss, A. Javed, W. J. Dressick, M. C. Demirel, *Fabrication and Use of Electroless Plated Polymer Surface-Enhanced Raman Spectroscopy Substrates for Viral Gene Detection*, Journal of Physical Chemistry C, **114**, 10730 (2010).

55. A. S. Paulo, N. Arellano, J. A. Plaza, R. He, C. Carraro, M. Maboudian, R. T. Howe, J. Bokor, P. Yang, *Suspended Mechanical Structures Based on Elastic Silicon Nanowire Arrays*, Nano Letters, **7**, 1100 (2007).

56. G. Che, B. B. Lakshmi, C. R. Martin, E. R. Fisher, *Metal-Nanocluster-Filled Carbon Nanotubes: Catalytic Properties and Possible Applications in Electrochemical Energy Storage and Production,* Langmuir, **15**, 750 (1999).

57. K. Peng, A. Lu, R. Zhang, S.-T. Lee, *Motility of Metal Nanoparticles in Silicon and Induced Anisotropic Etching*, Advanced Functional Materials, **18**, 3026 (2008).

58. X. Li, P. W. Bohn, *Metal-assisted Chemical Etching in HF/H_2O_2 Produces Porous Silicon*, Applied Physics Letters, **77,** 2572 (2000).

59. D. H. Wan, H. L. Chen, S. Y. Chuang, C. C. Yu, Y. C. Lee, *Using Self-Assembled Nanoparticles to Fabricate and Optimize Subwavelength Textured Structures in Solar Cells*, Journal of Physical Chemistry C, **112**, 20567 (2008).

60. S. Bauer, J. G. Brunner, H. Jha, Y. Yasukawa, H. Asoh, H.; S. Ono, H. Böhm, J. P. Spatz, P. Schmuki, *Ordered Nanopore Boring in Silicon: Metal Assisted Etching using a Self-aligned Block Copolymer Au Nanoparticle Template and Gravity Accelerated Etching*, Electrochemistry Communication, **12**, 565 (2010).

61. H. Zhipeng, Z. Xuanxiong, R. Manfred, L. Lifeng, L. Woo, S. Tomohiro, S. Stephan, G. Ulrich, *Extended Arrays of Vertically Aligned Sub-10 nm Diameter Si Nanowires by Metal-Assisted Chemical Etching*, Nano Letters, **8**, 3046 (2008).

62. Y. Qu, L. Liao, Y. Li, H. Zhang, Y. Huang, X. Duan, *Electrically Conductive and Optically Active Porous Silicon Nanowires*, Nano Letters, **9**, 4539 (2009).

63. K. Tsujino, M. Matsumura, *Boring Deep Cylindrical Nanoholes in Silicon Using Silver Nanoparticles as a Catalyst,* Advanced Materials, **17**, 1045 (2005).

64. C. Chartier, S. Bastide, C. Levy-Clement, *Metal-Assisted Chemical Etching of Silicon in HF-H_2O_2*, Electrochimica Acta, **53**, 5509 (2008).

65. Y. Xiu, L. Zhu, D. W. Hess, C. P. Wong, *Hierarchical Silicon Etched Structures for Controlled Hydrophobicity/Super Hydrophobicity*, Nano Letters, **7**, 3388 (2007).

66. O. J. Hildreth, W. Lin, C. P. Wong, *Effect of Catalyst Shape and Etchant Composition on Etching Direction in Metal-Assisted Chemical Etching of Silicon to Fabricate 3D Nanostructures*, ACS Nano, **3**, 4033 (2009).

67. E. H. Anderson, D. Ha, J. A. Liddle, *Sub-pixel alignment for direct-write electron beam lithography*, Microelectronic Engineering, **73-74**, 74-79 (2004).

68. A. A. Tseng, *Recent development in micromilling using focused ion beam technology*, Journal of Micromechanical Microengineering, **14**, R15-R34 (2004).

69. Ernst Meyer, Hans J. Hug , Roland Bennewitz, *Scanning Probe Microscopy: The Lab on a Tip* (Springer, 2003).

70. Ray F. Egerton, *Physical Principles of Electron Microscopy: An Introduction to TEM, SEM, and AEM* (Springer 2005).

71. Robert Keyse, *Introduction to Scanning Transmission Electron Microscopy* (Royal Microscopical Society Microscopy Handbooks, 1997).

72. R.F. Egerton, *Electron Energy-Loss Spectroscopy in the Electron Microscope*, (Springer, 1996).

73. John R. Ferraro, *Introductory Raman Spectroscopy* (Academic Press, 2002).

74. V. Saptari, *Fourier Transform Spectroscopy Instrumentation Engineering* (SPIE, 2004).

75. http://www.eaglabs.com/ Evans Analytical Group.

76. N.W. Liu, A. Datta, C. Y. Liu, C. Y. Peng, H. H. Wang, Y. L. Wang, *Fabrication of anodic-alumina films with custom designed arrays of nanochannels*, Advanced Materials, **17**, 222 (2005).

77. Yi Cui, Mikael T. Bjork, J. Alexander Liddle, Carsten Sonnichsen, Benjamin

Boussert, A. Paul Alivisatos, *Integration of colloidal nanocrystals into lithographically patterned devices*, Nano Letters, **4**, 1093 (2004).

78. Takashi Yatsui, Wataru Nomura, Motoichi Ohtsu, *Self-assembly of size- and position-controlled ultralong nanodot chains using near-field optical desorption*, Nano Letters, **5**, 2548, (2005).

79. Y. L. Wang, Z. Shao, *Advances in Electronics and Electron Physics* (Academic Press, 1991).

80. J. B. Wang, A. Datta, Y. L. Wang, *Morphological changes of Si(100) induced by focused ion beam irradiation*, **135**, 129 (1998).

81. J. F. Zeigler, J. P. Biersack, *SRIM (TRIM 90) Simulation Package* (IBM Research, 1995), IBM.

82. H. Raether, *Springer Tracts in Modern Physics (volume 88): Excitation of Plasmons and Interband Transitions by Electrons* (Springer-Verlag, 1980).

83. R. H. Ritchie, *Plasma loses by fast electrons in thin films*, Physics Review, **106**, 874 (1957).

84. E. A. Stern, R. A. Ferrell, *Surface plasmon oscillations of a degenerate electron gas*, Physics Review, **120**, 130 (1960).

85. P. Schwerdtfeger, *Gold goes nano-from small clusters to low-dimensional assemblies*, Angewandte Chemie International Edition, **42**, 1892 (2003).

86. J. Aizpurua, G. W. Bryant, L. J. Richter, F. J. García de Abajo, *Optical properties of coupled metallice nanorods for field-enhanced spectroscopy*, Physics Review B, **71**, 235420 (2005).

87. I. Romero, J. Aizpurua, G. W. Bryant, F. J. García de Abajo, *Plasmons in nearly touching metallic nanoparticles: singular response in the limit of touching dimers,* Optics Express, **14**, 9988 (2006).

88. P. Nordlander, C. Oubre, E. Prodan, K. Li, M. I. Stockman, *Plasmon hybridization in nanoparticle dimers*, Nano Letters, **4**, 899 (2004).

89. J. Nelayah, M. Kociak, O. Stéphan, F. J. García de Abajo, M. Tencé, L. Henrard, D. Taverna, I. Pastoriza-Santos, L. M. Liz-Marzán, C. Colliex, *Mapping surface plasmons on a single metallic nanoparticle*, Nature Physics, **3**, 348 (2007).

90. J. Aizpurua, P. Hanarp, D. S. Sutherland, M. Käll, G. W. Bryant, F. J. García de Abajo, *Optical properties of gold nanorings*, Physics Review Letters, **90**, 057401 (2003).

91. F. Hao, C. L. Nehl, J. H. Hafner, P. Nordlander, *Plasmon resonances of a gold nanostar*, Nano Letters, **7**, 729 (2007).

92. B. K. Canfield, H. Husu, J. Laukkanen, B. Bai, M. Kuittinen, J. Turunen, M. Kauranen, *Local field assymetry drives second harmonic generation in noncentrosymmetric nanodimers,* Nano Letters, **7**, 1251 (2007).

93. T. Klar, M. Perner, S. Grosse, G. von Plessen, W. Spirkl, J. Feldmann, *Surface-plasmon resonances in single metallic nanoparticles*, Physics Review Letters, **80**, 4249 (1998).

94. K. Kneip, M. Moskovits, H. Kneipp, *Surface-Enhanced Raman Scattering: Physics and Applications* (Springer, 2006).

95. T. Atay, J.-H. Song, A. V. Nurmikko, *Strongly interacting plasmon nanoparticle pairs: from dipole-dipole interaction to conductively coupled regime,* Nano Letters, **4**, 1627 (2004).

96. I. Khan, D. Cunningham, S. Lazar, D. Graham, W. E. Smith, D. W. McComb, *A TEM and electron energy loss spectroscopy (EELS) investigation of active and inactive silver particles for surface enhanced resonance Raman spectroscopy (SERRS)*, Faraday Discussions, **132**, 171 (2006).

97. M. Danckwerts, L. Novotny, *Optical frequency mixing at couples gold nanoparticles*, Physics Review Letters, **98**, 026104 (2007).

98. E. Ozbay, *Plasmonics: merging photonics and electronics at nanoscale dimensions*, Science, **311**, 189 (2006).

99. J.-Y. Chu, T.-J. Wang, Y.-C. Chang, Y.-J. Lu, M.-W. Lin, J.-T. Yeh, J.-K. Wang, *Multi-wavelength heterodyne-detected scattering-type scanning near-field optical microscopy*, Ultramicroscopy, **108**, 314 (2008).

100. M.-W. Chu, C. H. Chen, F. Javier García de Abajo, J.-P. Deng, C.-Y. Mou, *Surface exciton polaritons in individual Au nanoparticles in the far-ultraviolet spectral regime*, Physics Review B, **77**, 245402 (2008)

101. M.-W. Chu, V. Myroshnychenko, C. H. Chen, J.-P. Deng, C.-Y. Mou, and F. Javier García de Abajo, *Probing bright and dark surface-plasmon modes in individual and coupled noble metal nanoparticles using an electron beam*, Nano Letters, **9**, 399 (299).

102. P. Moreau, N. Brun, C. A. Walsh, C. Colliex, A. Howie, *Relativistic effects in electron-energy-loss-spectroscopy observations of the Si/SiO_2 interface plasmon peak*, Physics Review B, **56**, 6774 (1997).

103. M. Bosman, V. J. Keast, M. Watanabe, A. I. Maaroof, M. B. Cortie, *Mapping surface plasmons at the nanometer scale with electron beam*, Nanotechnology, **18**, 165505 (2007).

104. T. L. Ferrell, P. M. Echenique, *Generation of surface excitations on dielectric spheres by an external electron beam*, Physics Review Letters, **55**, 1526 (1985).

105. Edward D. Palik, *Handbook of Optical Dielectric Constants of Solids*, (Academic Press, 1985).

106. F. Ouyang, P. E. Batson, M. Isaacson, *Quantum size effects in the surface-plasmon excitation of small metallic particles by electron-energy-loss-spectroscopy*, Physics Review B, **46**, 15421 (1992).

107. M. Schlüter, Die Optischen, *Eigenschaften von gold, silber, and gold-silber-legierungen zwischen 2 and 40 eV aus energieverlustmessungen*, Zeitschrift fur Physik, **250**, 87 (1972).

108. F. J. García de Abajo, A. Howie, *Retarded field calculation of electrón energy loss in inhomogeneous dielectrics*, Physics Review. B, **65**, 115418 (2002).

109. J. Aizpurua, A. Rivacoba, S. P. Apell, *Electron energy losses in hemispherical particles*, Physics Review B, **54**, 2091 (1996).

110. N. Zabala, A. Rivacoba, *Electron energy loss near supported particles*, Physics Review B, **48**, 14534 (1993).

111. V. Myroshnychenko, J. Rodríquez-Fernández, I. Pastoriza-Santos, A. M. Funston, C. Novo, P. Mulvaney, L. M. Liz-Marzán, and F. J. García de Abajo, *Modelling the optical response of gold nanoparticles* , Chemical Society Review, **37**, 1792 (2008).

112. K. S. Lee, M. A. El-Sayed, *Gold and silver nanoparticles in sensing and imaging: sensitivity of plasmon response to size, shape and metal composition*, Journal of Physical Chemistry B, **110**, 19220 (2006).

113. N. Yamamoto, S. Ohtani, F. J. García de Abajo, *Gap and Mie plasmons in individual silver nanospheres near a silver surface*, Nano Letters, **11**, 91 (2011).

114. J. W. Liaw, *New surface integral equations for the light scattering of multi-metallic nanoscatterers*, Engineering Analysis with Boundary Elements, **31**, 299 (2007).

115. S. Foteinopoulou, J. P. Vigneron, C. Vandenbem, *Optical near-field excitations on plasmonic nanoparticle-based structures*, Optics Express, **15**, 4253 (2007).

116. D. D. Evanoff Jr., G. Chumanov, *Synthesis and optical properties of silver nanoparticles and arrays*, Chemical Physics and Physical Chemistry, 6, 1221 (2005).

117. X. Li, J. Zhang, W. Xu, H. Jia, X. Wang, B. Yang, B. Zhao, B. Li, Y. Ozaki, *Mercaptoacetic acid-capped silver nanoparticles colloid: formation, morphology, and SERS activity*, Langmuir, **19**, 4285 (2003).

118. M. Maillard, S. Giorgio, M. P. Pileni, *Tuning the size of silver nanodisks with similar aspect ratios: synthesis, and optical properties*, Journal of Physical Chemistry B, **107**, 2466 (2003).

119. K. P. Velikov, G. E. Zegers, A. V. Blaaderen, *Synthesis and characterization of large colloidal silver particles*, Langmuir, **19**, 1384 (2003).

120. K. Esumi, A. Suzuki, A. Yamahira, K. Torigoe, *Role of poly(amidoamine) dendrimers for preparing nanoparticles of gold, platinum and silver*, Langmuir, **16**, 2604 (2000).

121. Y. Sun, Y. Xia, *Shape controlled synthesis of gold and silver nanoparticles*, Science, **298**, 2176 (2002).

122. Y. Plyuto, J. M. Berquier, C. Jackquiod, C. Ricolleau, *Ag nanoparticles synthesized in template structured mesoporous silica films on a glass substrate*, Chemical Communications, **17**, 1653 (1999).

123. Y. P. Zhao, D. X. Ye, G. C. Wang, T. M Lu, *Novel nano-column and nanoflower arrays by glancing angle deposition*, Nano Letters, **2**, 351 (2002).

124. F. Mafune, J. Kohno, Y. Takeda, T. Kondow, *Structure and stability of silver nanoparticles in aqueous solution produced by laser ablation*, Journal of Physical Chemistry B, **104**, 8333 (2000).

125. H. H. Huang, X. P. Ni, G. L. Loy, C. H. Chew, K. L. Tan, F. C. Loh, J. F. Deng, G. Q. Xu, *Photochemical formation of silver nanoparticles in poly(N-vinyl pyrrolidone)*, Langmuir, **12**, 909 (1996).

126. N. A. Kotov, M. E. D. Zaniquelli, F. C. Meldrum, J. H. Fendler, *Two-dimensional silver electrocrystallization under monolayers spread on aqueous silver nitrate*, Langmuir, **9**, 3710 (1993).

127. J. Zhu, S. Liu, O. Palchik, Y. Koltypin, A. Gadenken, *Shape-controlled synthesis of silver nanoparticles by pulse sonoelectrochemical methods*, Langmuir, **16**, 6396 (2000).

128. L. Gunnarsson, T. Rindzevicius, J. Prikulis, B. Kasemo, M. Kall, S. Zou, G. C. Schatz, *Confined plasmons in nanofabricated single silver particle pairs: experimental observations of strong interparticle interactions*, Journal of Physical Chemistry B, **109**, 1079 (2005).

129. J. Alegret, T. Rindzevicius, T. Pakizeh, Y. Alaverdyan, L. Gunnarsson, M. Kall, *Plasmonic properties of silver trimers with trigonal symmetry fabricated by electron-beam lithography*, Journal of Physical Chemistry C, **112**, 14313 (2008).

130. M. Grzelczak, J. Vermant, E. M. Frust, L. M. Liz-Marzan, *Directed self assembly of nanoparticles*, ACS Nano, **4**, 3591 (2010).

131. M. K. Kinnan, G. Chumanov, *Plasmonic coupling in two dimensional arrays of silver nanoparticles: II. Effect of particle size and interparticle distance*, Journal of Physical Chemistry C, **114**, 7496 (2010).

132. C. Sonnichsen, B. M. Reinhard, J. Liphardt, A. P. Alivisatos, *A molecular ruler based on plasmon coupling of single gold and silver nanoparticles*, Nature Biotechnology, **23**, 741 (2005).

133. L. V. Brown, H. Sobhani, J. B. Lassiter, P. Norlander, N. J. Hallas, *Heterodimers: Plasmonic properties of mismatched nanoparticles pairs*, ACS Nano, **4**, 819 (2010).

134. J. P. Novak, D. L. Feldheim, *Assembly of phenylacetylene-bridged silver and gold nanoparticles arrays*, Journal of American Chemical Society, **122**, 3979 (2000).

135. S. Sheikholeslami, Y. Jun, P. K. Jain, A. P. Alivisatos, *Coupling of optical resonances in a compositionally asymmetric plasmonic nanoparticles dimer*, Nano Letters, **10**, 2655 (2010).

136. N. W. Liu, A. Datta, C. Y. Liu, C. Y. Peng, H. H. Wang, Y. L. Wang, *Fabrication of anodic alumina films with custom-designed arrays of nanochannels*, Advanced Materials, **17**, 222 (2005).

137. N. W. Liu, C. Y. Liu, H. H. Wang, C. F. Hsu, M. Y. Lai, T. H. Chuang, Y. L. Wang, *Focused-ion-beam-based selective closing and opening of anodic alumina nanochannels for the growth of nanowire arrays comprising multiple elements*, Advanced Material, **20**, 2547 (2008).

138. A. Gerlach, W. Keller, J. Schulz, K. Schumacher, *Gas permeability of adhesives and their applications for hermetic packaging of microcomponents,* Microsystems Technology, **7**, 17 (2001).

139. M. Morita, T. Ohmi, E. Hasegawa, M. Kawakami, K. Suma, *Control factor of native oxide growth on silicon in air or in ultrapure water,* Applied Physics Letters, **55**, 562 (1989).

140. M. L. Chourou, K. Fukami, T. Sakka, S. Virtanen, Y. H. Ogata, *Metal assisted etching of p-type Si under anodic polarization in HF solution with and without H_2O_2,* Electrochimica Acta, **55**, 903 (2010).

141. M. L. Zhang , K. Q. Peng , X. Fan , J. S. Jie , R. Q. Zhang , S. T. Lee , N. B. Wong, *Preparation of large area uniform silicon nanowires arrays through metal-assisted chemical etching,* Journal of Physical Chemistry C, **112**, 4444 (2008).

142. O. J. Hildreth, W. Lin, C. P. Wong, *Effect of catalyst shape and etchant composition on etching direction in metal-assisted chemical etching of silicon to fabricate 3D nanostructures,* ACS Nano, **3**, 4033 (2009).

143. K. Tsujino, M. Matsumura, *Morphologies of nanoholes formed in silicon by wet etching in solutions containing HF and H_2O_2 at different concentrations using silver nanoparticles as catalyst,* Electrochimica Acta, **53**, 28 (2007).

144. Xiaoge Gregory Zhang: *Electrochemistry of Silicon and Its Oxide* (Springer, New York, 2001).

145. H. Angermann, W. Henrion, A. Roseler, M. Rebien, *Wet chemical passivation of Si(111)- and Si(100)- substrates,* Material Science B, **73**, 178 (2000).

146. S. Wei, W. Li, F. Zhang, X. Zhao, *Adsorption of Ag on Si(100) surface*, Physica B, **390**, 191 (2007).

147. T. Tsuboi, T. Sakka, Y. H. Ogata, *Metal deposition into porous silicon layer by immersion plating: influence of halogen ions*, Journal of Applied Physics, **83**, 4501 (1998).

148. Y. Y. Song, Z. H. Gao, J. H. Kelly, X. H. Xia, *Galvanic deposition of nanostructured noble-metal films on silicon*, Electrochemical and Solid State Letters, **8**, C148 (2005).

149. R.C. Rossi, M. X. Tan, N. S. Lewis, *Size dependent electrical behavior of spatially inhomogeneous barrier height regions on silicon*, Appied Physics Letters, **77**, 2698 (2000).

150. T. Shimizu, T. Xie, J. Nishikawa, S. Shingubara, S. Senz, U. Gosele, *Synthesis of vertical high-density epitaxial Si(100) nanowire arrays on a Si(100) substrate using an anodic aluminum oxide template*, Advanced Materials, **19**, 917, (2007).

151. B. Li, D. Yu, S. L. Zhang, *Raman spectral study of silicon nanowires*, Physical Review B, **59**, 1645 (1999).

152. P. A. Temple, C. E. Hathaway, *Multiphonon Raman spectrum of silicon*, Physical Review B, **7**, 3685 (1973).

153. M. Steinert, J. Acker, M. Krause, S. Oswald, K. Wetzig, *Reactive species generated during wet chemical etching of silicon in HF/HNO_3 mixtures*, Journal of Physical Chemistry B, **110**, 11377 (2006).

154. Z. Peng, H. Hu, M. I. B. Utama, L. M. Wong, K. Ghosh, R. Chen, S. Wang, Z. Shen, Q. Xiong, *Heteroepitaxial decoration of Ag nanoparticles on Si nanowires: A case study of Raman scattering and mapping*, Nano Letters, **10**, 3940 (2010).

155. A.K. Kalkan, S. J. Fonash, *Electroless synthesis of Ag nanoparticles on deposited nanostructured Si films*, Journal of Physical Chemistry B, **109**, 20779 (2005).

156. K. T Queeney, H. Fukidome, E. E. Chaban, Y. J. Chabal, *In-situ FTIR studies of reactions at silicon/liquid interface: wet chemical etching of ultrathin SiO_2 on Si(100)*, Journal of Physical Chemistry B, **105**, 3903 (2001).

157. B. E. Poling, G. H. Thompson, D.G. Friend, R. L. Rowley, W. V. Wilding: *Perry's Chemical Engineers' Handbook*, (MacGraw-Hill Publication, 2008).

158. J. Wang, H. Tu, W. Zhu, Q. Zhou, A. Liu, C. Zhang, *A comparative Raman spectroscopy study on silicon surface in HF, HF/H_2O_2, and HF/NH_4F aqueous solutions*, Materials Science Engineering B, **72**, 193 (2000).

159. I. Vlassiouk, C. D. Park, S. A. Vail, D. Gust, S. Smirnov, *Control of nanopore wetting by a photochromic spiropyran: a light controlled valve and electrical switch*, Nano Letters, **6**, 1013 (2006).

160. S. Venkateswaran, *Raman spectrum of hydrogen peroxide*, Nature, **127**, 406 (1931).

161. S. V. Gaisler, O. I. Semenova, R. G. Sharafutdinov, B. A. Kolesov, *Analysis of Raman spectra of amorphous-nanocrystalline silicon films*, *Physics of the Solid State*, **46**, 1528 (2004).

162. N. Hosoda, Y. Kyogoku, T. Suga, *Effect of the surface treatment on the room temperature bonding of Al to Si and SiO_2*, Journal of Materials Science, **33**, 253 (1998).

163. Y. Nagasawa, H. Ishida, F. Soeda, A. Ishitani, I. Yoshii, K. Yamamoto, *FT-IR-ATR observation of SiOH and SiH in the oxide layer on a Si wafer*, Mikrochimica Acta, **I**, 431, (1988).

164. P. Sharma, Y. L. Wang, *Directional Etching of Silicon by Silver Nanostructures*, Applied Physics Express, **4**, 25001 (2011).

165. X. Sun, R. Tao, L. Lin, Z. Li, Z. Zhang, J. Feng, *Fabrication and characterization of polycrystalline silicon nanowires with silver-assistance by electroless depositions*, Applied Surface Science, **257**, 3861 (2011).

166. Z. Huang, T. Shimizu, S. Senz, Z. Zhang. N. Geyer, U. Gosele, *Oxidation rate effect on the direction of metal-assisted chemical and electrochemical etching of silicon*, Journal of Physical Chemistry C, **114**, 10683 (2010).

167. Y. Q. Jia, L. Z. Zhang, J. S. Fu, B. R. Zhang, J. C. Mao, G. G. Qin, *Characterization of stain etched porous silicon with photoluminescence, electron paramagnetic resonance, and infrared absorption spectroscopy*, Journal of Applied Physics, **74**, 7615 (1993).

168. M. E. Dudley, K. W. Kolasinski, *Etching of silicon in fluoride solutions*, Surface Science, **603**, 1904 (2009).

169. K. W. Kolasinski, *Charge transfer and nanostructure formation during electroless etching of silicon*, Journal of Physical Chemistry C, **114**, 22098 (2010).

Appendix

A.1 List of Publications

1. Pradeep Sharma, C. Y. Liu, Chen-Feng Hsu, N. W. Liu, Y. L. Wang, *Ordered arrays of Ag nanoparticles grown by constrained self organization*, Applied Physics Letters, **89**, 163110 (2006).

2. Ming-Wen Chu, Pradeep Sharma, Ching-Pin Chang, Sz Chian Liou, Kun-Tong Tsai, Juen-Kai Wang, Yuh-Lin Wang, Cheng Hsuan Chen, *Probing surface plasmons in individual Ag nanoparticles in the ultra-violet spectral regime*, Nanotechnology, **20**, 235705 (2009).

3. P. Sharma, Y. L. Wang, *Directional Etching of Silicon by Silver Nanostructures*, Applied Physics Express, **4**, 25001 (2011).

4. Pradeep Sharma, Juen-Kai Wang, Yuh-Lin Wang, *Revealing intermediates of Ag-assisted Si etching by in-situ Raman and FTIR spectroscopy*, Submitted to Journal of Physical Chemistry C in year 2011.

A.2 List of Acronyms

1. Scanning electron microscopy (SEM)
2. Transmission electron microscopy (TEM)
3. Atomic force microscopy (AFM)
4. Scanning transmission electron microscopy (STEM)
5. Electron energy loss spectroscopy (EELS)
6. Fourier transform infrared spectroscopy (FTIR)
7. Electron beam lithography (EBL)
8. Focused ion beam lithography (FIB)
9. Porous anodic alumina (AAO or Anodic Aluminum Oxide)
10. TEM- energy dispersive X-ray spectrometry (TEM-EDX)
11. High resolution transmission electron microscopy (HRTEM)
12. Surface enhanced Raman scattering (SERS)
13. Half angle annular dark field {HAADF or Z (atomic number)-contrast imaging}
14. Hexagonal-close-packed (HCP)
15. Left hand side (LHS)
16. Right hand side (RHS)
17. Transport of Ions in Materials (TRIM) Code
18. Surface plasmons (SPs)
19. Nanoparticles (NPs)
20. Custom-designed arrays of AAO nanochannels (CDA)
21. Figure (Fig.)